Constrained Sequential Lamination: Nonconvex Optimization and Material Microstructure

Thesis by

Matt Fago

In Partial Fulfillment of the Requirements

for the Degree of

Doctor of Philosophy

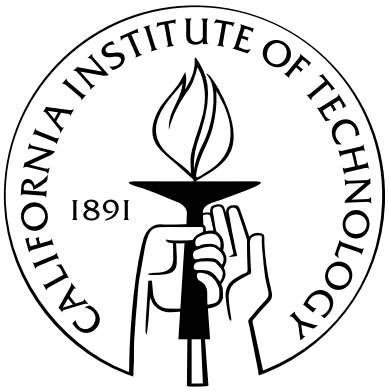

California Institute of Technology

Pasadena, California

2004

(Defended February 26, 2004)

For Katherin

Acknowledgements

During my studies I have had the opportunity to be mentored by a few truly exceptional teachers. I would like to begin by acknowledging Mr. Steve Young of Madison East High for showing me the beauty of calculus, while still insisting on mathematical rigor. Mr. Ellenbecker, Mr. Kelly, Mr. Murphy, and Mr. Paulson also all challenged me in their own way.

From the University of Michigan I would like to thank Prof. John Taylor for his peerless introduction to shear centers and finite element analysis, Prof. Pete Washabaugh for his structural dynamics course that was eerily similar in intensity to my first year at GALCIT, and Prof. Anthony Waas for his mentoring during my Edward A. Stalker Undergraduate Research Fellowship project.

My long road at GALCIT began under the care of Prof. Guruswami Ravichandran, whom I thank both for the research opportunities, and for his thorough re-introduction to modern solid mechanics after my industry hiatus. Of course, I also thank my advisor Prof. Michael Ortiz, in particular for his patient explanations and indelible computational mechanics course.

I doubt that the first year at GALCIT can be survived without the help of one's classmates, and I am grateful for their comradeship. In particular, I would like to thank the 'Baja Gang' Mike Rubel, Tait Pottebaum, Ian Spielman, and Chris Dionne, for their friendship

and unique lunchtime discussions.

I would like to thank Dr. Robert Rudd for the opportunity to work with him during my summer at Lawrence Livermore National Laboratory.

Nicolet Instruments provided me with invaluable early engineering industry experience and undergraduate tuition support provided by the Nicolet Hi-Step scholarship and internship.

I am also grateful for the resources and support afforded by the U.S. Department of Energy through Caltech's ASCI/ASAP Center for the Simulation of the Dynamic Behavior of Solids, and through the DOE's Computational Science Graduate Fellowship. Further, I would like to acknowledge the support provided by the AFOSR through Brown's MURI for the Design of Materials by Computation.

This thesis was completed in collaboration with numerous people. In particular, I would like to acknowledge the work of Dr. Sylvie Aubry, Dr. Alessandro Fortunelli, and Prof. Michael Ortiz, with special thanks to Prof. Kaushik Bhattacharya for his pertinent and helpful comments.

Finally, I would like to thank my wife, Katherin, to whom this thesis is dedicated, for accepting all that graduate school entailed. This could not have happened without you.

Abstract

A practical algorithm has been developed to construct, through sequential lamination, the partial relaxation of multiwell energy densities such as those characteristic of shape memory alloys. The resulting microstructures are in static and configurational equilibrium, and admit arbitrary deformations. The laminate topology evolves during deformation through branching and pruning operations, while a continuity constraint provides a simple model of metastability and hysteresis. In cases with strict separation of length scales, the method may be integrated into a finite element calculation at the *subgrid* level. This capability is demonstrated with a calculation of the indentation of a Cu-Al-Ni shape memory alloy by a spherical indenter.

In verification tests the algorithm attained the analytic solution in the computation of three benchmark problems. In the fourth case, the four-well problem (of, e.g., Tartar), results indicate that the method for microstructural evolution imposes an energy barrier for branching, hindering microstructural development in some cases. Although this effect is undesirable for purely mathematical problems, it is reflective of the activation energies and metastabilities present in applications involving natural processes.

The method was further used to model Shield's tension test experiment, with initial calculations generating reasonable transformation strains and microstructures that compared well with the sequential laminates obtained experimentally.

Contents

List of Figures

List of Tables

Chapter 1

Introduction

A central problem in mechanics concerns the prediction of material processes on multiple length scales and their cumulative effect on material behavior. Constitutive models that incorporate effects from several length scales are important tools, both in circumstances in which the model is directly applicable, and in the development of high fidelity models at larger scales.

The research detailed herein is concerned with the computation of microstructures resulting from the optimization of nonconvex energy functionals. This problem has mathematical interest in its own right, but the present work will focus on applications to solid mechanics. In particular, the algorithm developed will primarily be used in conjunction with constitutive models of martensitic materials.

1.1 Martensitic materials

To begin, we review the theory of martensitic materials and compute some relevant examples. For more background refer to, e.g., [1, 11, 12, 17, 37, 58, 60] and references therein. This overview shall largely follow the progression of Bhattacharya [17].

Martensitic materials, such as shape-memory alloys, are characterized by the occurrence of a rapid diffusionless solid-solid phase transformation from a high symmetry austenite

phase to one or more martensite phases upon a change in temperature or the application of load. The resulting microstructures typically consist of complex arrangements of several symmetry related variants. The composition, arrangement, and behavior of these microstructures is the topic of this work.

In this class of materials, under proper conditions, the energy landscape imposed by quantum mechanics renders the austenite phase unstable, instead favoring a different atomic configuration. The prediction of this instability, while beyond the present scope, is accessible to current methods in quantum chemistry such as Density Functional Theory [68].

Positing the existence of such phases, we require a formal description. Due to the diffusionless nature of the transformation, there exists a linear mapping, corresponding to a homogeneous deformation, that produces the lattice vectors of one variant from another

$$\boldsymbol{e}_i^{martensite} = \boldsymbol{U}\boldsymbol{e}_i^{austenite} \tag{1.1}$$

where $\boldsymbol{U}$ is the transformation matrix, and the $\boldsymbol{e}_i$ are lattice vectors. There will in general be several symmetry related martensite variants, each with a corresponding transformation strain $\boldsymbol{U}_i$. As an example, InTl undergoes a cubic to tetragonal transformation with the cubic austenite described by the transformation matrix

$$\boldsymbol{U}_A = \boldsymbol{I} \tag{1.2}$$

where $\boldsymbol{I}$ is the identity matrix, and with three martensite phases

$$\boldsymbol{U}_1 = \mathrm{diag}(\beta, \alpha, \alpha), \quad \boldsymbol{U}_2 = \mathrm{diag}(\alpha, \beta, \alpha), \quad \boldsymbol{U}_3 = \mathrm{diag}(\alpha, \alpha, \beta), \tag{1.3}$$

where diag() is a diagonal matrix and $\{\alpha, \beta\}$ describe the relative lengths of the lattice vectors. The three martensites thus correspond to stretching the cubic lattice by β in each of the three coordinate directions in turn, with the remaining two lattice vectors both deformed an amount α.

Frame indifference and material symmetry require the energy functional to satisfy

$$W(\boldsymbol{R}_P^T \boldsymbol{F} \boldsymbol{R}_P) = W(\boldsymbol{F}) \tag{1.4}$$

where $\boldsymbol{F}$ is the deformation gradient and $\boldsymbol{R}_P$ are the rotations that map the lattice onto itself (the point group of the lattice). Accordingly, the energy functional must reflect the same symmetries embodied by the variants. This further implies that the related variants must have the same energy. Frame indifference alone implies

$$W(\boldsymbol{R}\boldsymbol{F}) = W(\boldsymbol{F}),\ \boldsymbol{R} \in SO(3), \tag{1.5}$$

indicating that the energy of each variant is a well. Consequently, an energy model for these materials is to assign similar energy wells to each martensite variant and another to the austenite phase. The relative stability of each phase is accounted for by the value of the energy at each well. Therefore, at the transformation temperature T_c all of the wells possess the same value of the energy at their minima, above T_c the austenite well is at a lower energy, while below the martensites are favored. This multiwell structure, imposed by lattice symmetry, is nonconvex. As we shall see in the next section, these nonconvex energies are responsible for the formation of microstructures.

Postulating the existence of microstructures, or recalling the experimental evidence [28, 74], we shall investigate the governing relations. For an interface between two material

phases to exist (without dislocations) the lattice vectors must satisfy continuity. Expressed in terms of transformation matrices, we require that they share a common plane

$$\boldsymbol{R}_i\boldsymbol{U}_i - \boldsymbol{R}_j\boldsymbol{U}_j = \boldsymbol{a} \otimes \boldsymbol{N} \tag{1.6}$$

where $\{\boldsymbol{U}_i, \boldsymbol{U}_j\}$ are the transformation strains of the two variants, $\boldsymbol{N}$ is the normal to the invariant plane, $\boldsymbol{a}$ is the shearing direction, and the variants are allowed to reorient via $\{\boldsymbol{R}_i, \boldsymbol{R}_j\} \in SO(3)$. Fixing the rotation of one variant and redefining $\boldsymbol{a}$ allows (1.6) to be re-written as

$$\boldsymbol{R}\boldsymbol{U}_i - \boldsymbol{U}_j = \boldsymbol{a} \otimes \boldsymbol{N} \tag{1.7}$$

which is known as the twinning equation. This equation states that the deformations $\boldsymbol{R}\boldsymbol{U}_i$ and $\boldsymbol{U}_j$ on either side of an interface are *rank-one connected*, i.e., they differ by the rank-one matrix $\boldsymbol{a} \otimes \boldsymbol{N}$. Note that equation (1.7) assumes that each variant is at its respective minimum energy deformation $\boldsymbol{U}$—the 'constrained' theory of Ball and James [11, 12]—which corresponds to the assumption that the material moduli are significantly larger than the transformation stresses, and thus elastic deformations can be neglected. While the deformations in general need not equal the transformation strain, compatability still insists they be rank-one connected. Equation (1.7) does not indicate which microstructure will form. However, with either sufficient creativity or with recourse to experimental results, it can be used to explore possible compatible microstructures.

In anticipation of the work to follow, we shall derive several important microstructures present in Cu-Al-Ni. This material undergoes a cubic to orthorhombic martensitic transformation and has, therefore, six variants in the martensitic phase. The deformation undergone by the material in transforming from austenite to an unstressed variant of martensite may

be described by a stretch tensor $\boldsymbol{U}_m$, $m = 1, \ldots, 6$. For Cu-Al-Ni, these are [28, 29]:

$$\boldsymbol{U}_1 = \begin{pmatrix} \zeta & 0 & 0 \\ 0 & \xi & \eta \\ 0 & \eta & \xi \end{pmatrix}, \quad \boldsymbol{U}_2 = \begin{pmatrix} \zeta & 0 & 0 \\ 0 & \xi & -\eta \\ 0 & -\eta & \xi \end{pmatrix}, \quad \boldsymbol{U}_3 = \begin{pmatrix} \xi & 0 & \eta \\ 0 & \zeta & 0 \\ \eta & 0 & \xi \end{pmatrix}, \tag{1.8}$$

$$\boldsymbol{U}_4 = \begin{pmatrix} \xi & 0 & -\eta \\ 0 & \zeta & 0 \\ -\eta & 0 & \xi \end{pmatrix}, \quad \boldsymbol{U}_5 = \begin{pmatrix} \xi & \eta & 0 \\ \eta & \xi & 0 \\ 0 & 0 & \zeta \end{pmatrix}, \quad \boldsymbol{U}_6 = \begin{pmatrix} \xi & -\eta & 0 \\ -\eta & \xi & 0 \\ 0 & 0 & \zeta \end{pmatrix}, \tag{1.9}$$

where $\xi = 1.0425$, $\eta = 0.0194$ and $\zeta = 0.9178$, and all components are referred to the cubic axes of the austenitic phase.

1.1.1 Martensite–martensite laminate

An important microstructure observed experimentally [28, 29] is the laminar mixing of two martensite variants, shown schematically in Fig. 1.1. Thus, given variants $\boldsymbol{U}_i$ and $\boldsymbol{U}_j$, we

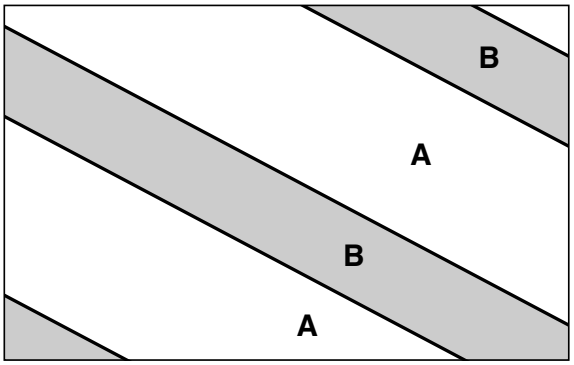

Figure 1.1: Schematic of a martensite–martensite microstructure with variants A and B.

wish to determine values of $\boldsymbol{R}$, $\boldsymbol{a}$, and $\boldsymbol{N}$ that satisfy (1.7). Using Proposition 4 of Ball and James [11], this can be reduced to the following algorithm as given by Bhattacharya [17].

Equation (1.7) has a solution if and only if

$$\lambda_1 \leq 1 \quad \lambda_2 = 1 \quad \lambda_3 \geq 1 \tag{1.10}$$

where the λ_i, not all 1, are the ordered eigenvalues of

$$\boldsymbol{C} = \boldsymbol{U}_j^{-T}\boldsymbol{U}_i^T\boldsymbol{U}_i\boldsymbol{U}_j^{-1}. \tag{1.11}$$

There are then two solutions, given by

$$\boldsymbol{a} = \rho\left(\sqrt{\frac{\lambda_3(1-\lambda_1)}{\lambda_3-\lambda_1}}\boldsymbol{e}_1 + \kappa\sqrt{\frac{\lambda_1(\lambda_3-1)}{\lambda_3-\lambda_1}}\boldsymbol{e}_3\right) \tag{1.12}$$

$$\boldsymbol{N} = \frac{\sqrt{\lambda_3}-\sqrt{\lambda_1}}{\rho\sqrt{\lambda_3-\lambda_1}}\left(-\sqrt{1-\lambda_1}\boldsymbol{U}_2^T\boldsymbol{e}_1 + \kappa\sqrt{\lambda_3-1}\boldsymbol{U}_2^T\boldsymbol{e}_3\right) \tag{1.13}$$

where $\kappa = \pm 1$, $\rho \neq 0$ such that $|\boldsymbol{N}| = 1$, and $\boldsymbol{e}_i$ are the eigenvectors corresponding to λ_i. $\boldsymbol{R}$ can then be found via (1.7).

The above procedure can be used to determine the required $\{\boldsymbol{R}, \boldsymbol{a}, \boldsymbol{N}\}$ to satisfy (1.7) for two general deformations. Since we are following the constrained theory, as noted, the above has been written with respect to the transformation strains $\boldsymbol{U}$.

When the martensite variants are related via

$$\boldsymbol{U}_i = \boldsymbol{R}^T\boldsymbol{U}_j\boldsymbol{R} \tag{1.14}$$

where $\boldsymbol{R}$ is a plane of symmetry of the austenite and therefore is a 180° rotation about an axis $\hat{\boldsymbol{e}}$, as is the case for Cu-Al-Ni, there is a simplification to the solution of (1.7). The

twinning equation again has two solutions, with the first solution given by [17]

$$\boldsymbol{a} = 2\left(\frac{\boldsymbol{U}_i^{-T}\hat{\boldsymbol{e}}}{|\boldsymbol{U}_i^{-T}\hat{\boldsymbol{e}}|^2} - \boldsymbol{U}_i\hat{\boldsymbol{e}}\right), \quad \boldsymbol{N} = \hat{\boldsymbol{e}}, \tag{1.15}$$

and a second solution

$$\boldsymbol{a} = \rho\boldsymbol{U}_i\hat{\boldsymbol{e}}, \quad \boldsymbol{N} = \frac{2}{\rho}\left(\widetilde{\boldsymbol{e}} - \frac{\boldsymbol{U}_i^T\boldsymbol{U}_i\hat{\boldsymbol{e}}}{|\boldsymbol{U}_i\hat{\boldsymbol{e}}|^2}\right), \quad \rho = 2\left|\hat{\boldsymbol{e}} - \frac{\boldsymbol{U}_i^T\boldsymbol{U}_i\hat{\boldsymbol{e}}}{|\boldsymbol{U}_i\hat{\boldsymbol{e}}|^2}\right|, \tag{1.16}$$

where ρ has been calculated so that $|\boldsymbol{N}| = 1$. For Cu-Al-Ni this calculation has been carried out by Bhattacharya, Li and Luskin [21]. The required rotation axes are given by $\hat{\boldsymbol{e}} = \boldsymbol{e}/|\boldsymbol{e}|$, with the vector $\boldsymbol{e}$ as in Table 1.1.

wells	1	2	3	4	5	6
1		$\boldsymbol{e}_3$	$\boldsymbol{e}_1 - \boldsymbol{e}_2$	$\boldsymbol{e}_1 + \boldsymbol{e}_2$	$\boldsymbol{e}_1 - \boldsymbol{e}_3$	$\boldsymbol{e}_1 + \boldsymbol{e}_3$
2	$\boldsymbol{e}_2$		$\boldsymbol{e}_1 + \boldsymbol{e}_2$	$\boldsymbol{e}_1 - \boldsymbol{e}_2$	$\boldsymbol{e}_1 + \boldsymbol{e}_3$	$\boldsymbol{e}_1 - \boldsymbol{e}_3$
3	$\boldsymbol{e}_1 - \boldsymbol{e}_2$	$\boldsymbol{e}_1 + \boldsymbol{e}_2$		$\boldsymbol{e}_3$	$\boldsymbol{e}_2 - \boldsymbol{e}_3$	$\boldsymbol{e}_2 + \boldsymbol{e}_3$
4	$\boldsymbol{e}_1 + \boldsymbol{e}_2$	$\boldsymbol{e}_1 - \boldsymbol{e}_2$	$\boldsymbol{e}_3$		$\boldsymbol{e}_2 + \boldsymbol{e}_3$	$\boldsymbol{e}_2 - \boldsymbol{e}_3$
5	$\boldsymbol{e}_1 - \boldsymbol{e}_3$	$\boldsymbol{e}_1 + \boldsymbol{e}_3$	$\boldsymbol{e}_2 - \boldsymbol{e}_3$	$\boldsymbol{e}_2 + \boldsymbol{e}_3$		$\boldsymbol{e}_2$
6	$\boldsymbol{e}_1 + \boldsymbol{e}_3$	$\boldsymbol{e}_1 - \boldsymbol{e}_3$	$\boldsymbol{e}_2 + \boldsymbol{e}_3$	$\boldsymbol{e}_2 - \boldsymbol{e}_3$	$\boldsymbol{e}_1$	

Table 1.1: Vector $\boldsymbol{e}$ arising in the twinning relations for Cu-Al-Ni [21]. The vectors $\{\boldsymbol{e}_1, \boldsymbol{e}_2, \boldsymbol{e}_3\}$ correspond to the cubic directions in the austenite phase.

These solutions can be classified as follows. When the solution for $\boldsymbol{N}$ is rational, as in (1.15), the solution is referred to as a *Type I twin*. Conversely, solutions (1.16) where $\boldsymbol{a}$ is rational are *Type II twins*. In some instances both $\boldsymbol{a}$ and $\boldsymbol{N}$ are rational—corresponding to two solutions for $\boldsymbol{R}$ in (1.14)—referred to as a *compound twin*. For Cu-Al-Ni, the pairs $\{1, 2\}$, $\{3, 4\}$ and $\{5, 6\}$ produce compound twins.

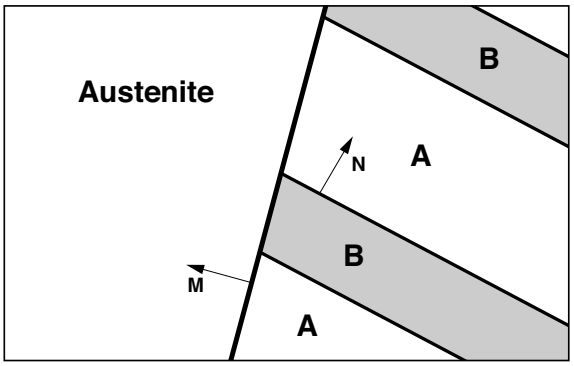

Figure 1.2: Schematic of an austenite–twinned martensite microstructure with martensite variants A and B.

1.1.2 Austenite–twinned martensite

Note that the solutions in Table 1.1 are between martensite variants only, and do not include the austenite phase. Equation (1.7) has a solution involving austenite and martensite only in very specific circumstances that do not occur for the vast majority of materials. Yet, experimental evidence [74] clearly indicates the formation of an interface between austenite and martensite. One such observed microstructure is illustrated in Fig. 1.2.

The interface between the martensites in the figure obeys (1.7) as above, but the interface between this laminate and the austenite satisfies continuity only in an average sense. In physical microstructures a transition region attains exact compatability at the interface [29, 50]. This average deformation gradient is

$$\boldsymbol{F}_M = \lambda \boldsymbol{R}\boldsymbol{U}_i + (1-\lambda)\boldsymbol{U}_j \tag{1.17}$$

where λ is the proportion of variant $\boldsymbol{U}_i$. We thus wish to find possible interfaces between

$\boldsymbol{F}_M$ and austenite. Writing (1.7) for each of the interfaces shown in Fig. 1.2

$$\boldsymbol{R}\boldsymbol{U}_i - \boldsymbol{U}_j = \boldsymbol{a} \otimes \boldsymbol{N} \tag{1.18}$$

$$\boldsymbol{Q}\boldsymbol{F}_M - \boldsymbol{I} = \boldsymbol{b} \otimes \boldsymbol{M} \tag{1.19}$$

where $\boldsymbol{I}$ is the transformation strain of the austenite, $\{\boldsymbol{Q}, \boldsymbol{R}\} \in SO(3)$, and $\{\boldsymbol{N}, \boldsymbol{M}\}$ (with corresponding $\{\boldsymbol{a}, \boldsymbol{b}\}$) are defined in Fig. 1.2. The solution to (1.18) must correspond to one of the solutions obtained above. Theorem 7 of Ball and James [11] provides a solution to (1.19), which can be stated as follows [17].

Let

$$\delta = \boldsymbol{a} \cdot \boldsymbol{U}_j(\boldsymbol{U}_j^2 - \boldsymbol{I})^{-1}\boldsymbol{N} \tag{1.20}$$

$$\eta = \text{trace}(\boldsymbol{U}_j^2) - \det(\boldsymbol{U}_j^2) - 2 + \frac{|\boldsymbol{a}|^2}{2\delta}. \tag{1.21}$$

A solution exists if and only if $\delta \leq -2$ and $\eta \geq 0$. If $\delta = -2$ there is only one solution

$$\lambda = \frac{1}{2}\left(1 - \sqrt{1 + \frac{2}{\delta}}\right) \tag{1.22}$$

$$\boldsymbol{b} = \rho\left(\sqrt{\frac{\lambda_3(1-\lambda_1)}{\lambda_3 - \lambda_1}}\boldsymbol{e}_1 + \kappa\sqrt{\frac{\lambda_1(\lambda_3 - 1)}{\lambda_3 - \lambda_1}}\boldsymbol{e}_3\right) \tag{1.23}$$

$$\boldsymbol{M} = \frac{\sqrt{\lambda_3} - \sqrt{\lambda_1}}{\rho\sqrt{\lambda_3 - \lambda_1}}\left(-\sqrt{1-\lambda_1}\boldsymbol{e}_1 + \kappa\sqrt{\lambda_3 - 1}\boldsymbol{e}_3\right) \tag{1.24}$$

where $\lambda_1 \leq \lambda_2 \leq \lambda_3$ are eigenvalues with corresponding eigenvectors $\{\boldsymbol{e}_1, \boldsymbol{e}_2, \boldsymbol{e}_3\}$ of the

matrix

$$\boldsymbol{C} = (\boldsymbol{U}_j + \lambda \boldsymbol{N} \otimes \boldsymbol{a})(\boldsymbol{U}_j + \lambda \boldsymbol{a} \otimes \boldsymbol{N}) \tag{1.25}$$

and where ρ is chosen so $|\boldsymbol{M}| = 1$, $\kappa = \pm 1$, and $\boldsymbol{Q}$ is obtained from (1.19), while if $\delta < -2$ there is a second solution corresponding to $\lambda \to (1 - \lambda)$.

Note that for each pair of variants i and j there are two solutions to (1.18) corresponding to the two choices for κ in (1.12) and (1.13), each with up to four solutions to (1.18) and (1.19). There are, therefore, eight possible austenite–twinned martensite solutions for each pair of martensite wells. For the case of Cu-Al-Ni, all eight solutions exist for the 12 Type I and Type II twins, with no solution for the three compound twins, resulting in a total of 96 solutions. A tabulation of these solutions is available in [74].

The two examples discussed above, while important, are by no means comprehensive. For example, Bhattacharya has studied martensite wedges [14], while Chu and James have observed a doubly laminated microstructure [29]. To determine which microstructure is preferred, and to understand why they occur at all, one needs to look at energetics and the issues involved with minimizing the nonconvex multiwell energies of such materials.

1.2 Nonconvex optimization

This section will give a brief overview of some of the issues involved in the minimization of nonconvex energies such as the multiwell energy discussed above. The field is a large and difficult one; for more background refer to [9, 11, 12, 17, 33, 37, 48, 54, 59, 60, 71].

Formally, we are interested in problems of the form

$$\inf_{y \in V} I, \quad I = \int_\Omega W(D\boldsymbol{y}(\boldsymbol{x}))d\boldsymbol{x} \tag{1.26}$$

where $\Omega \in \mathbb{R}^3$ is a deformable body, $\boldsymbol{y}(\boldsymbol{x}) : \Omega \to \mathbb{R}^3$ is a deformation with gradient $\boldsymbol{F}(\boldsymbol{x}) = D\boldsymbol{y}(\boldsymbol{x})$, $W(\boldsymbol{F}) : \mathbb{R}^{3\times 3} \to \mathbb{R}, W \geq 0$ is an energy density, and V is a suitable solution space. While seemingly innocent, it is well known that such problems may be ill-posed if W is nonconvex. Recall that a function $f(\boldsymbol{x})$ is *convex* if

$$f(\lambda \boldsymbol{a} + (1-\lambda)\boldsymbol{b}) \leq \lambda f(\boldsymbol{a}) + (1-\lambda) f(\boldsymbol{b}) \tag{1.27}$$

$\forall \boldsymbol{a}, \boldsymbol{b}$ in the domain of f, $\forall \lambda \in [0,1]$.

We begin by reviewing the simple scalar case (see, e.g., [44, 59]) using the classical approach. We are interested in obtaining the function $y(x)$ that infimizes

$$I = \int f(x, y(x), y'(x)) dx. \tag{1.28}$$

In this case we can write the first variation

$$\frac{\partial}{\partial \lambda} I(y + \lambda \eta)\bigg|_{\lambda=0} = 0 \tag{1.29}$$

where $\eta(x)$ is any admissible function. This results in

$$\delta I = \int \left[\eta'(x) f_{y'} + \eta(x) f_y\right] dx = 0 \tag{1.30}$$

where, e.g., $f_y = \partial f / \partial y$. When integrated by parts this yields

$$\delta I = \int \eta \left[f_y - \frac{d}{dx} f_{y'}\right] dx = 0 \tag{1.31}$$

which must hold for all η. This finally leads us to the Euler equation for this case

$$f_y = \frac{d}{dx} f_{y'} = f_{y'y'} y'' + f_{y'y} y' + f_{y'x}. \tag{1.32}$$

Note that if $f_{y'y'} \geq 0$ this equation is elliptic, a necessary condition for a solution of (1.28) to exist, indicating the importance of the convexity of f with respect to y'.

The vectoral case is more complex. Following the direct method of the calculus of variations [33], we demand that the integral I in (1.26) be finite and bounded from below. We then seek minimizing sequences $\{y_\nu\}$ such that for some subsequence $y_\nu \to y_m$ and $I(y_\nu) \searrow I_m$ so that $I(y_m) = I_m$ and I has a minimizer y_m. This requires the *(sequential) weak lower semicontinuity* of I

$$\boldsymbol{y}_\nu \rightharpoonup \boldsymbol{y} \Rightarrow \liminf_{\nu \to \infty} I(\boldsymbol{y}_\nu) \geq I(\boldsymbol{y}) \tag{1.33}$$

and reveals the crux of the problem: we need to determine if I is weakly lower semicontinuous (l.s.c.) for the energy functional of interest.

Morrey [59] showed that an equivalent condition for the existence of minimizers is for W to be *quasiconvex*, that is,

$$\int_\Omega W(\boldsymbol{F}) d\boldsymbol{x} \leq \int_\Omega W(\boldsymbol{F} + D\varphi(\boldsymbol{x})) d\boldsymbol{x} \tag{1.34}$$

for all $\boldsymbol{F}$ and $\varphi(\boldsymbol{x})$. Hence, for a quasiconvex energy W, I is minimized by linear mappings $\boldsymbol{F}$ [59].

A similar existence condition is based on polyconvexity [9], where a function W is

polyconvex if

$$W(\boldsymbol{F}) = g(M(\boldsymbol{F})) \tag{1.35}$$

where g is a convex function of $M(\boldsymbol{F})$, the vector of all minors of $\boldsymbol{F}$. For $\boldsymbol{F} \in \mathbb{R}^{3\times 3}$, $M(\boldsymbol{F}) = (\boldsymbol{F}, \mathrm{cof}(\boldsymbol{F}), \det(\boldsymbol{F}))$.

Another important concept of convexity is *rank-one convexity*, defined as

$$W(\lambda \boldsymbol{a} + (1-\lambda)\boldsymbol{b}) \leq \lambda W(\boldsymbol{a}) + (1-\lambda) W(\boldsymbol{b}) \tag{1.36}$$

$\forall \boldsymbol{a}, \boldsymbol{b}$ in the domain of W, $\forall \lambda \in [0,1]$, where $\mathrm{rank}(\boldsymbol{a} - \boldsymbol{b}) \leq 1$. Thus W is rank-one convex if it is convex along all line segments with endpoints that differ by a rank-one matrix. Note that this definition (1.36) implies that the total energy described by the rank-one compatible energy wells discussed in §1.1 is not rank-one convex (see, e.g., [33, 71]).

An important result is the relationship between the various notions of convexity, given here as in Dacorogna [33]

$$\begin{array}{ccccccc} W \text{ convex} & \not\Leftarrow\!\Rightarrow & W \text{ polyconvex} & \not\Leftarrow\!\Rightarrow & W \text{ quasiconvex} & \not\Leftarrow\!\Rightarrow & W \text{ rank-one convex} \\ & & & & \Updownarrow & & \Updownarrow \\ & & & & \begin{array}{c} I \text{ weakly lower} \\ \text{semicontinu-} \\ \text{ous} \end{array} & & \begin{array}{c} \text{Euler} \\ \text{equations are} \\ \text{elliptic} \end{array} \end{array} \tag{1.37}$$

where the last negative result is due to Šverák [80]. In one dimension all of these forms are equivalent. In the present context, the most important implication of (1.37) is that the multiwell energy density under discussion is not quasiconvex (and I is not l.s.c.), and thus in general the infimum of (1.26) is not attained.

The concepts above are best illustrated with a simple example as discussed by Bhattacharya and others [17, 60, 86]. Consider the one dimensional problem involving the deformation $y(x), x \in (0,1)$ with gradient $f = dy/dx$ and an energy

$$E(f) = (f(x)^2 - 1)^2 \tag{1.38}$$

which has two wells at $f = \pm 1$. We will consider the total energy functional

$$I = \int_0^1 \left[\Big((f(x))^2 - 1 \Big)^2 + (y(x))^2 \right] dx \tag{1.39}$$

as in this simple example it is necessary to augment $E(f)$ to obtain the behavior of interest. We wish to find a deformation y with zero energy. This requires

$$\frac{dy(x)}{dx} = f = \pm 1 \quad \text{and} \quad y(x) = 0 \tag{1.40}$$

which is obviously impossible. Yet, we can construct a minimizing sequence $\{y_\nu\} = \{y^1, y^2, \ldots, y^n\}$ composed of the 'sawtooth' functions

$$y^n(x) = \begin{cases} x, & \text{if } 0 < x < \frac{1}{2n}, \\ \\ \frac{1}{n} - x, & \text{if } \frac{1}{2n} \le x < \frac{2}{2n}, \end{cases} \tag{1.41}$$

where y^n is extended periodically for $x \in (\frac{2}{2n}, 1)$, and is continuous. Obviously $f = \pm 1 \implies E(f) = 0$, while $y \to 0$ in an *average* sense: $\{y_\nu\}$ is a *weakly convergent sequence*. It is thus clear that $\lim_{n\to\infty} I(y^n) = 0$. Yet notice that I is not weakly l.s.c., i.e., $\{y_\nu\} \rightharpoonup 0$ but $I(0) > 0$. Similar, less contrived, but more lengthy, examples can be found in the references above, all of which reinforce the key point: lack of lower semicontinuity (or similarly quasiconvexity)

leads to the formation of microstructures which represent *approximate solutions* to the problem (1.26).

One approach to the solution of such problems is via direct minimization of (1.26) using, e.g., the finite element method. While straightforward, the preceeding discussion indicates that this effort is in general essentially hopeless; the mesh would need to resolve the microstructural details, and, further, would bias the solution. Nevertheless, as shown by the indentation calculations of Tadmor et al. [81], and the small-scale finite element model of the austenite–martensite interface of James et al. [50], this method can yield useful results. Similarly, Collins et al. [30, 31, 58] solve the unrelaxed problem directly on a finite element mesh, imposing affine boundary conditions consistent with the average deformation gradient of a given laminate microstructure. This technique allows for the examination and visualization of possible microstructures, but does suffer from mesh effects.

Alternatively, one can search for an *effective* or *relaxed* form of the energy that accounts for the development of microstructure, and consequently would be quasiconvex. The solution of this relaxed problem would be devoid of microstructure and would attain the infimum.

Associated with each concept of convexity in (1.37) is an associated convex envelope and convexification. The convex, polyconvex, quasiconvex, and rank-one convex envelopes of the function f are defined as [33]

$$\begin{aligned} Cf &= \sup\{g \leq f : g \text{ convex}\} \\ Pf &= \sup\{g \leq f : g \text{ polyconvex}\} \\ Qf &= \sup\{g \leq f : g \text{ quasiconvex}\} \\ Rf &= \sup\{g \leq f : g \text{ rank-one convex}\} \end{aligned} \tag{1.42}$$

which with (1.37) implies

$$Cf \leq Pf \leq Qf \leq Rf \leq f. \tag{1.43}$$

Again following Dacorogna [33], given a function $f : \mathbb{R}^{n\times m} \to \mathbb{R}\cup\{+\infty\}$ the convexification is

$$Cf(A) = \inf_{\lambda_i, A_i} \left\{ \sum_{i=1}^{nm+1} \lambda_i f(A_i) : \sum_{i=1}^{nm+1} \lambda_i A_i = A \right\}, \forall A \in \mathbb{R}^{n\times m}, \tag{1.44}$$

with an analogous expression for the polyconvexification. The quasiconvexification is similarly computed via

$$Qf(A) = \inf_{\varphi} \left\{ \frac{1}{|\Psi|} \int_{\Psi} f(A + D\varphi(\boldsymbol{x}))d\boldsymbol{x} \right\}, \forall A \in \mathbb{R}^{n\times m}, \tag{1.45}$$

and is independent of the domain Ψ. Finally, following the construction of Kohn and Strang [53, 54], the rank-one convexification can be written as

$$Rf_0 = f \tag{1.46}$$

$$R_{k+1}f(A) = \inf_{\lambda, A_1, A_2} \{\lambda R_k f(A_1) + (1-\lambda) R_k f(A_2)\} \tag{1.47}$$

$$Rf = \lim_{k\to\infty} R_k f \tag{1.48}$$

where $A = \lambda A_1 + (1-\lambda)A_2$ and $\operatorname{rank}(A_1 - A_2) \leq 1$. This definition is equivalent to the H_N conditions discussed, e.g., by Dacorogna [33]. In the present setting, the rank-one convexification is the minimum energy attainable via recursive laminations of rank-one connected deformations. Such a construction is referred to as a *sequential laminate*, with a microstructure corresponding to R_k denoted as a rank-k laminate. The martensite–martensite microstructure studied in §1.1.1 thus corresponds to a rank-one sequential laminate, while

the austenite–twinned martensite of §1.1.2 is rank-two.

Returning to the solution of (1.26), it can be shown [33] that not only does the relaxed problem attain the infimum, but the solution is also a minimizer to the original problem, i.e.,

$$\min \int_\Omega QW(D\boldsymbol{y}(\boldsymbol{x}))d\boldsymbol{x} = \inf \int_\Omega W(D\boldsymbol{y}(\boldsymbol{x}))d\boldsymbol{x}. \tag{1.49}$$

More precisely, as the unrelaxed problem need not attain its infimum, the minimizers of the relaxed problem are weak limits of minimizing sequences of the original problem. A general approach to obtain QW is thus highly desirable.

Unfortunately, the quasiconvexification is known only for a few problems (see, e.g., [37, 52, 54]), with no general algorithm available. Equation (1.46) does suggest a method for obtaining RW, at least in the limit. However, $RW \not\Rightarrow QW$ in general, implying that this may only obtain a partial relaxation. We could therefore restrict ourselves to the study of sequential laminates, which is the basis for the algorithm developed in the sequel.

Using this approach, Dolzmann introduced an algorithm [36, 39] that computes the rank-one convexification of a function $f \in \mathbb{R}^{m\times n}$ on a uniform grid, shown to converge to Rf as the mesh size decreases. The method operates via iterating over all matrices on the grid and performing a convexification using tabulated rank-one directions at each point. However, because of this tabulation the algorithm is only practical for $f \in \mathbb{R}^{2\times 2}$, and is somewhat expensive: the presented numerical examples used, e.g., a mesh on $[-4, 4]^4$ of 33^4 mesh points with 64 rank-one directions, requiring 75 million individual convexifications per iteration over the grid.

More generally, Govindjee et al. [45–47] have implemented an algorithm based on a lower-bound of the quasiconvexification of the energy. The implementation, reminiscent

of plasticity calculations, has been used to predict the experimental results of Shield [74], and, further, offers insight into the relaxation of a general N-variant energy. However, this method is formulated using small strains, requires isotropic moduli, and cannot provide microstructural details if desired.

Bhattacharya and Dolzmann [18, 19] have constructed approximate relaxed energy functionals for the tetragonal-to-orthorhombic (two-well) and tetragonal-to-monoclinic (four-well) cases. Their approach involved the determination of the quasiconvex hull of the transformation strains—the (average) deformation gradients with zero energy. Given this set, a quasiconvex energy functional was constructed that satisfied material symmetry, was zero only on the quasiconvex hull with quadratic growth elsewhere, and reproduced the material moduli.

An alternative approach to convexification is to solve the unrelaxed problem (1.26), but consider a solution space consisting of 'acceptable' microstructures as described by *parameterized measures* or *Young measures*. This method, first introduced by Young in 1937 [86], describes the solution in terms of the local proportions (or probability distribution) of each phase in an infinitesimally fine mixture. By their definition, Young measures characterize *all* minimizing sequences without requiring unnecessary details, and need not represent laminates. For more detail, see [51, 60, 70, 71] and references within.

Ball and James have used parameterized measures to obtain an important result for the two-well and three-well problems [11, 12]. Given boundary conditions corresponding to a simple laminate

$$\boldsymbol{F} = \lambda \boldsymbol{U}_1 + (1-\lambda)\, \boldsymbol{R}\boldsymbol{U}_2 \tag{1.50}$$

with $\boldsymbol{R} \in SO(3)$, $\lambda \in [0,1]$ and $\operatorname{rank}(\boldsymbol{U}_1 - \boldsymbol{R}\boldsymbol{U}_2) = 1$, where the $\boldsymbol{U}_i$ are transformation

stretches, they showed that the resulting microstructure is unique with Young measures that correspond to a simple laminate if $\lambda \in (0, 1)$. Bhattacharya, Li and Luskin [21] have obtained a similar result for cubic-to-orthorhombic transformations for nearly all values of the transformation strains. Bhattacharya et al. also provide stability and error estimate results useful in finite element calculations similar to those given by Li and Luskin [56, 57] in the cubic-to-tetragonal case.

An example of a numerical application utilizing this method, Aranda and Pedregal [4] have proposed an algorithm based on a finite element approximation of Young measures resulting from the partial rank-one convexification of the energy [5]. They present results for the two well problem which indicate some influence on mesh orientation.

For a survey of other numerical approaches consult the review article by Luskin [58]. Further background particularly relevant to the specific topic at hand will be provided in later chapters.

Given the limitations of the current relaxation methods, there remains a need for an efficient numerical algorithm for the relaxation of general multiwell energy densities. The work presented here represents significant progress towards this end.

1.3 Outline

The next chapter, which first appeared as [7] (reproduced with permission), will present and demonstrate an algorithm for computing the partial relaxation of a general multiwell energy density via the explicit construction of a sequential laminate. The resulting microstructure is at a local energy minimum, and is in static and configurational equilibrium. The present author's contribution included the finite element example calculations and requisite adaptation and refinement of the lamination algorithm.

The algorithm will be verified in Chapter 3 through comparison with several benchmark problems. This provides the opportunity to both verify the correctness and understand the limitations of the algorithm without the complications of an experiment.

In Chapter 4 the lamination algorithm will be used to model Shield's Cu-Al-Ni tension test experiment [74]. Shield obtained both the stress-strain response and microstructural details for specimens at several orientations, enabling experimental verification of both the response and microstructures obtained numerically.

The final chapter will offer conclusions and areas for further research.

Chapter 2

A constrained sequential lamination algorithm

2.1 Introduction

Materials often are capable of adopting a multiplicity of crystal structures, or phases, the relative stability of which depends on temperature, the state of stress, and other factors. Under conditions such that several phases are energetically favorable, e.g., at the transition temperature in martensitic materials, materials are often found to develop microstructure in nature or in the laboratory. A central problem in mechanics concerns the prediction of these microstructures and their effect on the effective or macroscopic behavior of materials, including such scaling properties and size effects as may result from their formation and evolution. When martensitic materials are modelled within the confines of nonlinear elasticity, the coexistence of phases confers their strain-energy density function a multiwell structure [16, 29, 40, 57]. The corresponding boundary value problems are characterized by energy functions which lack weak sequential lower-semicontinuity, and the energy-minimizing deformation fields tend to develop fine microstructure [11, 12, 33, 60].

There remains a need at present for efficient numerical methods for solving macroscopic boundary-value problems while simultaneously accounting for microstructure development

at the microscale. One numerical strategy consists of attempting a direct minimization of a suitably discretized energy function. For instance, Tadmor et al. [81] have applied this approach to the simulation of nanoindentation in silicon. The energy density is derived from the Stillinger-Weber potential by recourse to the Cauchy-Born approximation, and accounts for five phases of silicon. The energy functional is discretized by an application of the finite-element method. Tadmor et al. [82] pioneering calculations predict the formation of complex phase arrangements under the indenter, and such experimentally observed features as an insulator-to-conductor transition at a certain critical depth of indentation.

Despite these successes, direct energy minimization is not without shortcomings. Thus, analysis has shown (see, e.g., [60] for a review) that the microstructures which most effectively relax the energy may be exceedingly intricate and, consequently, unlikely to be adequately resolved by a fixed numerical grid. As a result, the computed microstructure is often coarse and biased by the computational mesh, which inhibits—or entirely suppresses—the development of many of the competing microstructures. By virtue of these constraints, the numerical solution is often caught up in a metastable local minimum which may not accurately reflect the actual energetics and deformation characteristics of the material.

In applications where there is a clear separation of micro and macrostructural length scales, an alternative numerical strategy is to use a suitably relaxed energy density in calculations [13, 27, 34, 45, 58]. In this approach, the original multiwell energy density is replaced by its *quasiconvex* envelop, i.e., by the lowest energy density achievable by the material through the development of microstructure. Thus, the determination of the relaxed energy density requires the evaluation of *all* possible microstructures compatible with a prescribed macroscopic deformation. The resulting relaxed energy density is quasiconvex [60], and its minimizers, which represent the macroscopic deformation fields, are devoid

of microstructure and, thus, more readily accessible to numerical methods. In essence, the use of relaxed energy densities in macroscopic boundary value problems constitutes a multiscale approach in which the development of microstructure occurs—and is dealt with—at the *subgrid* level. The central problem in this approach is to devise an effective means of determining the relaxed energy density and of integrating it into macroscopic calculations.

Unfortunately, no general algorithm for the determination of the quasiconvex envelop of an arbitrary energy density is known at present. A fallback strategy consists of the consideration of *special* microstructures only, inevitably resulting in a partial relaxation of the energy density. For instance, attention may be restricted to microstructures in the form of *sequential laminates* [34, 36, 52, 58, 63, 64]. The lowest energy density achievable by the material through sequential lamination is known as the *rank-one* convexification of the energy density. Many of the microstructures observed in shape-memory alloys [29] and in ductile single crystals [63] may be interpreted as instances of sequential lamination, which suggests that the rank-one convexification of the energy coincides—or closely approximates—the relaxed energy for these materials. Ductile single crystals furnish a notable example in which the rank-one and the quasiconvex envelops are known to coincide exactly [6].

In this paper we present a practical algorithm for partially relaxing multiwell energy densities. The algorithm is based on sequential lamination and, hence, at best it returns the rank-one convexification of the energy density. Sequential lamination constructions have been extensively used in both analysis and computation [4, 5, 11, 16, 49, 52, 55, 58, 63]. All microstructures generated by the algorithm are in static and configurational equilibrium. Thus, we optimize all the interface orientations and variant volume fractions, with the result that all configurational forces and torques are in equilibrium. We additionally allow the variants to be arbitrarily stressed and enforce traction equilibrium across all interfaces.

The proposed lamination construction is *constrained* in an important respect: during a deformation process, we require that every new microstructure be reachable from the preceding microstructure along an admissible transition path. The mechanisms by which microstructures are allowed to effect topological transitions are: *branching*, i.e., the splitting of a variant into a rank-one laminate; and *pruning*, consisting of the elimination of variants whose volume fraction reduces to zero. Branching transitions are accepted provided that they reduce the total energy, without consideration of energy barriers. By repeated branching and pruning, microstructures are allowed to evolve along a deformation process. The *continuation* character of the algorithm furnishes a simple model of metastability and hysteresis. Thus, successive microstructures are required to be 'close' to each other, which restricts the range of microstructures accessible to the material at any given time. In general, this restriction causes the microstructures to be path-dependent and metastable, and the computed macroscopic response may exhibit hysteresis.

The proposed relaxation algorithm may effectively be integrated into macroscopic finite-element calculations at the subgrid level. We demonstrate the performance and versatility of the algorithm by means of a numerical example concerned with the indentation of a Cu-Al-Ni shape memory alloy [29] by a spherical indenter. The calculations illustrate the ability of the algorithm to generate complex microstructures while simultaneously delivering the macroscopic response of the material. In particular, the algorithm results in force-depth of indentation curves considerably softer than otherwise obtained by direct energy minimization.

2.2 Problem formulation

Let $\Omega \in \mathbb{R}^3$ be a bounded domain representing the reference configuration of the material. Let $\boldsymbol{y}(x) : \Omega \to \mathbb{R}^3$ be the deformation and $\boldsymbol{F}(x) = D\boldsymbol{y}(x)$ be the corresponding deformation gradient. We denote the elastic energy density at deformation gradient $\boldsymbol{F} \in \mathbb{R}^{3\times 3}$ by $W(\boldsymbol{F})$. We require $W(\boldsymbol{F})$ to be material frame indifferent, i.e., to be such that $W(\boldsymbol{RF}) = W(\boldsymbol{F})$, $\forall \boldsymbol{R} \in SO(3)$ and $\boldsymbol{F} \in \mathbb{R}^{3\times 3}$. In addition, the case of primary interest here concerns materials such that $W(\boldsymbol{F})$ is not quasiconvex. As a simple example, we may suppose that $W(\boldsymbol{F})$ has the following special structure: Let $W_i(\boldsymbol{F})$, $i = 1, \ldots, M$ be quasiconvex energy densities (see, e.g., [33] for a definition and discussion of quasiconvexity), representing the energy wells of the material. Then

$$W(\boldsymbol{F}) = \min_{m=0,\ldots,M} W_m(\boldsymbol{F}) \tag{2.1}$$

i.e., $W(\boldsymbol{F})$ is the lower envelop of the functions $W_m(\boldsymbol{F})$.

A common model of microstructure development in this class of materials presumes that the microstructures of interest correspond to low-energy configurations of the material, and that, consequently, their essential structure may be ascertained by investigating the absolute minimizers of the energy. However, the energy functionals resulting from multiwell energy densities such as (2.1) lack weak-sequential lower semicontinuity and their infimum is not attained in general [33]. The standard remedy is to introduce the quasiconvex envelop

$$QW(\boldsymbol{F}) = \frac{1}{|Q|} \inf_{\boldsymbol{u}\in W_0^{1,\infty}(\Omega)} \int_Q W(\boldsymbol{F} + D\boldsymbol{u})dx \tag{2.2}$$

of $W(\boldsymbol{F})$, or relaxed energy density. In this expression, $W_0^{1,\infty}(\Omega)$ denotes the space of functions whose distributional derivatives are essentially bounded and which vanish on

the boundary, and Q is an arbitrary domain. Physically, $QW(\boldsymbol{F})$ represents the lowest energy density achievable by the material through the development of microstructure. The macroscopic deformations of the solid are then identified with the solutions of the relaxed problem

$$\inf_{\boldsymbol{y}\in X}\left\{\int_{\Omega}[QW(D\boldsymbol{y})-\boldsymbol{f}\cdot\boldsymbol{y}]dx-\int_{\partial\Omega_2}\bar{\boldsymbol{t}}\cdot\boldsymbol{y}\right\} \tag{2.3}$$

where X denotes some suitable solution space, $\boldsymbol{f}$ is a body force field, $\boldsymbol{t}$ represents a distribution of tractions over the traction boundary $\partial\Omega_2$, and the deformation of the body is constrained by displacement boundary conditions of the form

$$\boldsymbol{y}=\bar{\boldsymbol{y}} \text{ on } \partial\Omega_1=\partial\Omega-\partial\Omega_2. \tag{2.4}$$

Thus, in this approach the effect of microstructure is built into the relaxed energy $QW(\boldsymbol{F})$. The relaxed problem defined by $QW(\boldsymbol{F})$ then determines the macroscopic deformation.

In executing this program the essential difficulty resides in the determination of the relaxed energy $QW(\boldsymbol{F})$. As mentioned in the introduction, no general algorithm for the determination of the quasiconvex envelop of an arbitrary energy density is known at present. A fallback strategy is to effect a partial relaxation of the energy density by recourse to *sequential lamination* [52, 58] and the use of the resulting rank-one convexification $RW(\boldsymbol{F})$ of $W(\boldsymbol{F})$ in lieu of $QW(\boldsymbol{F})$ in the macroscopic variational problem (2.3). We recall that the rank-one convexification $RW(\boldsymbol{F})$ of $W(\boldsymbol{F})$ follows as the limit [53, 54]

$$RW(\boldsymbol{F})=\lim_{k\to\infty}R_kW(\boldsymbol{F}) \tag{2.5}$$

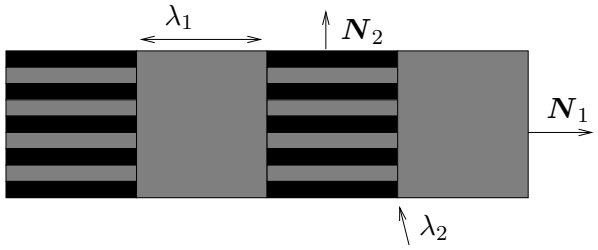

Figure 2.1: Example of a rank-two laminate. λ_1 and λ_2 are the volume fractions corresponding to levels 1 and 2, respectively, and $\boldsymbol{N}_1$ and $\boldsymbol{N}_2$ are the corresponding unit normals.

where $R_0W(\boldsymbol{F}) = W(\boldsymbol{F})$ and $R_kW(\boldsymbol{F})$ is defined recursively as

$$R_kW(\boldsymbol{F}) = \inf_{\lambda,\boldsymbol{a},\boldsymbol{N}} \{(1-\lambda)R_{k-1}W(\boldsymbol{F} - \lambda\boldsymbol{a}\otimes\boldsymbol{N}) + \lambda R_{k-1}W(\boldsymbol{F} + (1-\lambda)\boldsymbol{a}\otimes\boldsymbol{N}), \\ \lambda \in [0,1], \boldsymbol{a}, \boldsymbol{N} \in \mathbb{R}^3, |\boldsymbol{N}| = 1\} \quad k \geq 1. \tag{2.6}$$

In these expressions, λ and $1-\lambda$ represent the volume fractions of the k-level variants, $\boldsymbol{N}$ is the unit normal to the planar interface between the variants, and $\boldsymbol{a}$ is a vector (see Fig. 2.1).

Unfortunately, a practical algorithm for the evaluation of the rank-one convexification of general energy densities 'on the fly' does not appear to be available at present. Dolzmann [36] has advanced a method for the computation of the exact rank-one convexification of an arbitrary energy density in two dimensions. However, extensions of the method to three dimensions are not yet available. In addition, the method requires the *a priori* tabulation of $RW(\boldsymbol{F})$ over all of $\mathbb{R}^{2\times 2}$, which limits its applicability to large-scale computing.

An additional complication arises from the fact that the cyclic behavior of martensitic materials often exhibits hysteresis. Under these conditions, the response of the material is path-dependent and dissipative, and, therefore, absolute energy minimization does not furnish a complete model of material behavior. The modeling of hysteresis requires con-

sideration of entire deformation processes, rather than isolated states of deformation of the material. A framework for the understanding of hysteresis may be constructed by assuming that the evolution of microstructure is subject to a *continuity* requirement, namely, the requirement that successive microstructures be close to each other in some appropriate sense. This constraint restricts the range of microstructures which the material may adopt at any given time and thus results in metastable configurations. The particular sequence of metastable configurations adopted by the material may be path dependent, resulting in hysteresis. The connection between metastability and hysteresis has been discussed by Ball, Chu and James [10].

2.3 A sequential lamination algorithm

The problem which we address in the remainder of this chapter concerns the formulation of efficient algorithms for the evaluation of $RW(\boldsymbol{F})$, and extensions thereof accounting for kinetics and nonlocal effects, with specific focus on algorithms which can be effectively integrated into large-scale macroscopic simulations. We begin by reviewing basic properties of sequential laminates for subsequent reference. More general treatments of sequential lamination may be found in [14, 15, 52, 54, 58, 69].

Uniform deformations may conventionally be categorized as rank-zero laminates. A rank-one laminate is a layered mixture of two deformation gradients, $\boldsymbol{F}^-$, $\boldsymbol{F}^+ \in \mathbb{R}^{3\times 3}$. Compatibility of deformations then requires $\boldsymbol{F}^\pm$ to be rank-one connected, i.e.,

$$\boldsymbol{F}^+ - \boldsymbol{F}^- = \boldsymbol{a} \otimes \boldsymbol{N} \tag{2.7}$$

where $\boldsymbol{a} \in \mathbb{R}^3$, and $\boldsymbol{N} \in \mathbb{R}^3$, $|\boldsymbol{N}| = 1$, is the normal to the interface between the two variants

of deformation. Let $\lambda^{\pm}$,

$$\lambda^- + \lambda^+ = 1, \quad \lambda^{\pm} \in [0,1], \tag{2.8}$$

denote the volume fractions of the variants. Then, the average or macroscopic deformation follows as

$$\boldsymbol{F} = \lambda^- \boldsymbol{F}^- + \lambda^+ \boldsymbol{F}^+. \tag{2.9}$$

If $\boldsymbol{F}$ and $\{\boldsymbol{a}, \lambda^{\pm}, \boldsymbol{N}\}$ are known, then the deformation in the variants is given by

$$\begin{aligned} \boldsymbol{F}^+ &= \boldsymbol{F} + \lambda^- \boldsymbol{a} \otimes \boldsymbol{N} \\ \boldsymbol{F}^- &= \boldsymbol{F} - \lambda^+ \boldsymbol{a} \otimes \boldsymbol{N} \end{aligned} \tag{2.10}$$

and, thus, $\boldsymbol{F}$ and $\{\boldsymbol{a}, \lambda^{\pm}, \boldsymbol{N}\}$ define a complete set of—deformation and configurational—degrees of freedom for the laminate. Following Kohn [52], a laminate of rank-k is a layered mixture of two rank-$(k-1)$ laminates, which affords an inductive definition of laminates of any rank. As noted by Kohn [52], the construction of sequential laminates assumes a separation of scales: the length scale l_k of the kth-rank layering satisfies $l_k \ll l_{k-1}$.

Sequential laminates have a binary-tree structure. Indeed, with every sequential laminate we may associate a *graph* G such that: the nodes of G consist of all the sub-laminates of rank less than or equal to the rank k of the laminate; and joining each sub-laminate of order $1 \leq l \leq k$ with its two constituent sub-laminates of order $l-1$. The root of the graph is the entire laminate. Two sequential laminates will be said to have the same *structure* (alternatively, *topology* or *layout*) if their graphs are identical. Evidently, having the same structure defines an equivalence relation between sequential laminates, and the set of all equivalence classes is in one-to-one correspondence with the set $\mathcal{B}$ of binary trees.

Let $i = 1, \ldots, n$ be an enumeration of the nodes of G. Then, to each node i we may

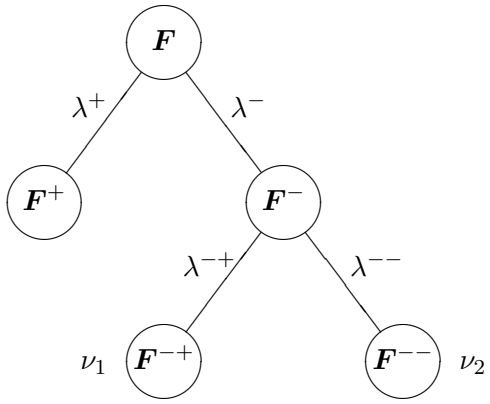

Figure 2.2: Example of a rank-two laminate. In this example, $\nu_1 = \lambda^-\lambda^{-+}$ and $\nu_2 = \lambda^-\lambda^{--}$.

associate a deformation $\boldsymbol{F}_i$. The root deformation is the average or macroscopic deformation $\boldsymbol{F}$. Each node in the tree has either two children or none at all. Nodes with a common parent are called siblings. Nodes without children are called leaves. Nodes which are not leaves are said to be interior. The deformations of the children of node i will be denoted $\boldsymbol{F}_i^{\pm}$. Each generation of nodes is called a level. The root occupies level 0 of the tree. The number of levels is the rank k of the tree. Level l contains at most 2^l nodes. The example in Fig. 2.2 represents a rank-two laminate of order four. The three leaves of the tree are nodes $\boldsymbol{F}^+$, $\boldsymbol{F}^{-+}$ and $\boldsymbol{F}^{--}$. The interior nodes are $\boldsymbol{F}$ and $\boldsymbol{F}^-$. The children of, e.g., node $\boldsymbol{F}^-$ are nodes $\boldsymbol{F}^{-+}$ and $\boldsymbol{F}^{--}$.

Compatibility demands that each pair of siblings be rank-one connected, i.e.,

$$\boldsymbol{F}_i^+ - \boldsymbol{F}_i^- = \boldsymbol{a}_i \otimes \boldsymbol{N}_i, \quad i \in \mathcal{I}_G \tag{2.11}$$

where $\boldsymbol{a}_i \in \mathbb{R}^3$, $\boldsymbol{N}_i \in \mathbb{R}^3$, $|\boldsymbol{N}| = 1$, is the normal to the interface between $\boldsymbol{F}_i^-$ and $\boldsymbol{F}_i^+$, and $\mathcal{I}_G$ denotes the set of all interior nodes. Let $\lambda_i^{\pm}$,

$$\lambda_i^- + \lambda_i^+ = 1, \quad \lambda_i^{\pm} \in [0, 1], \tag{2.12}$$

denote the volume fractions of the variants $\boldsymbol{F}_i^{\pm}$ with respect to node i. Then, the deformation of the parent variant is recovered in the form

$$\boldsymbol{F}_i = \lambda_i^- \boldsymbol{F}_i^- + \lambda_i^+ \boldsymbol{F}_i^+. \tag{2.13}$$

If $\boldsymbol{F}_i$ and $\{\boldsymbol{a}_i, \lambda_i^{\pm}, \boldsymbol{N}_i\}$ are known for an interior node i, then the deformation of its children is given by

$$\begin{aligned} \boldsymbol{F}_i^+ &= \boldsymbol{F}_i + \lambda_i^- \boldsymbol{a}_i \otimes \boldsymbol{N}_i \\ \boldsymbol{F}_i^- &= \boldsymbol{F}_i - \lambda_i^+ \boldsymbol{a}_i \otimes \boldsymbol{N}_i. \end{aligned} \tag{2.14}$$

Therefore, $\boldsymbol{F}$ and $\{\boldsymbol{a}_i, \lambda_i^{\pm}, \boldsymbol{N}_i, i \in \mathcal{I}\}$ define a complete and independent set of degrees of freedom for the laminate. A recursive algorithm for computing all the variant deformations $\boldsymbol{F}_i$, $i = 1, \ldots, n$ from $\boldsymbol{F}$ and $\{\boldsymbol{a}_i, \lambda_i^{\pm}, \boldsymbol{N}_i, i \in \mathcal{I}_G\}$ has been given by [64].

We shall also need the global volume fractions ν_l of all leaves $l \in \mathcal{L}_G$, where $\mathcal{L}_G$ denotes the collection of all leaves of G. These volume fractions are obtained recursively from the relations

$$\nu_i^{\pm} = \lambda_i^{\pm} \nu_i, \quad i \in \mathcal{I}_G \tag{2.15}$$

with $\nu_{\text{root}} = 1$ for the entire laminate, and satisfy the relation

$$\sum_{l \in \mathcal{L}_G} \nu_l = 1. \tag{2.16}$$

Thus, ν_l represents the volume occupied by leaf l as a fraction of the entire laminate. The Young measure (e.g., [60]) of the laminate consists of a convex combination of atoms $\delta_{\boldsymbol{F}_l}(\boldsymbol{F})$ with weights ν_l, $l \in \mathcal{L}$.

The average or macroscopic stress of the laminate may be expressed in the form

$$\boldsymbol{P} = \sum_{l \in \mathcal{L}_G} \nu_l \boldsymbol{P}_l \tag{2.17}$$

where

$$\boldsymbol{P}_l = W_{,\boldsymbol{F}}\left(\boldsymbol{F}_l\right), \quad l \in \mathcal{L}_G \tag{2.18}$$

are the first Piola-Kirchhoff stresses in the leaves. The average stress may be computed by recursively applying the averaging relation

$$\boldsymbol{P}_i = \lambda^- \boldsymbol{P}_i^- + \lambda^+ \boldsymbol{P}_i^+, \quad i \in \mathcal{I} \tag{2.19}$$

starting from the leaves of the laminate. A recursive algorithm for computing the average stress $\boldsymbol{P}$ from $\{\boldsymbol{P}_l, l \in \mathcal{L}\}$ and $\{\lambda_i^{\pm}, i \in \mathcal{I}_G\}$ has been given by [64].

2.3.1 Microstructural equilibrium

We begin by investigating the mechanical and configurational equilibrium of sequential laminates of a given structure. Thus, we consider an elastic material with strain-energy density $W(\boldsymbol{F})$ subject to a prescribed macroscopic deformation $\boldsymbol{F} \in \mathbb{R}^{3\times 3}$. In addition, we consider all sequential laminates with given graph G.

The equilibrium configurations of the laminate then follow as the solutions of the constrained minimization problem

$$GW(\boldsymbol{F}) = \inf_{\{\boldsymbol{a}_i, \lambda_i^{\pm}, \boldsymbol{N}_i, i \in \mathcal{I}_G\}} \quad \sum_{l \in \mathcal{L}_G} \nu_l W(\boldsymbol{F}_l) \tag{2.20}$$

$$\lambda_i^{\pm} \in [0,\, 1], \quad i \in \mathcal{I}_G \tag{2.21}$$

$$|\boldsymbol{N}_i| = 1, \quad i \in \mathcal{I}_G \tag{2.22}$$

where the $\boldsymbol{F}_l$ are obtained from the recursive relations (2.14). The effective or macroscopic energy of the laminate is $GW(\boldsymbol{F})$. If $W(\boldsymbol{F})$ is quasiconvex then it necessarily follows that $\boldsymbol{a}_i = \boldsymbol{0}$, $\forall i \in \mathcal{I}_G$, and $GW(\boldsymbol{F}) = W(\boldsymbol{F})$.

It is interesting to verify that the solutions of the minimization problem (2.20) are in both force and configurational equilibrium. Thus, assuming sufficient smoothness, the stationarity of the energy with respect to all deformation jump amplitudes yields the traction equilibrium equations

$$(\boldsymbol{P}_i^+ - \boldsymbol{P}_i^-) \cdot \boldsymbol{N}_i = \boldsymbol{0}, \quad i \in \mathcal{I}_G. \tag{2.23}$$

Stationarity with respect to all normal vectors yields the configurational-torque equilibrium equations

$$[\boldsymbol{a}_i \cdot (\boldsymbol{P}_i^+ - \boldsymbol{P}_i^-)] \times \boldsymbol{N}_i = \boldsymbol{0}, \quad i \in \mathcal{I}_G. \tag{2.24}$$

Finally, stationarity with respect to all volume fractions yields the configurational-force equilibrium equations

$$f_i = (W_i^+ - W_i^-) - (\lambda_i^+ \boldsymbol{P}_i^+ + \lambda_i^- \boldsymbol{P}_i^-) \cdot (\boldsymbol{a}_i \otimes \boldsymbol{N}_i) = 0, \quad i \in \mathcal{I}_G \tag{2.25}$$

where f_i is the configurational force which drives interfacial motion [75]. It bears emphasis that the leaf deformations $\boldsymbol{F}_l$ may in general be arbitrarily away from the minima of $W(\boldsymbol{F})$, and thus the equilibrium equations (2.23) must be carefully enforced. In addition, the minimization (2.20) has the effect of *optimizing* the volume fractions of all variants and

the corresponding interface orientations. If all the preceding stationarity conditions are satisfied, then it is readily verified that the average or macroscopic deformation (2.17) is recovered as

$$\boldsymbol{P} = GW_{,\boldsymbol{F}}\,(\boldsymbol{F}) \tag{2.26}$$

which shows that $GW(\boldsymbol{F})$ indeed supplies a potential for the average or macroscopic stress of the laminate.

The case in which the energy density $W(\boldsymbol{F})$ possesses the multiwell structure (2.1) merits special mention. In this case, the minimization problem (2.20-2.22) may be written in the form

$$GW(\boldsymbol{F}) = \inf_{\substack{\{\boldsymbol{a}_i,\lambda_i^{\pm},\boldsymbol{N}_i,\ i\in\mathcal{I}_G\} \\ \{m_l\in\{1,\ldots,M\},\ l\in\mathcal{L}_G\}}} \quad \sum_{l\in\mathcal{L}_G} \nu_l W_{m_l}(\boldsymbol{F}_l) \tag{2.27}$$

$$\lambda_i^{\pm} \in [0,\,1], \quad i \in \mathcal{I}_G \tag{2.28}$$

$$|\boldsymbol{N}_i| = 1, \quad i \in \mathcal{I}_G \tag{2.29}$$

where $\boldsymbol{m} = \{m_l \in \{1,\ldots,M\},\ l \in \mathcal{L}_G\}$ denotes the collection of wells which are active in each of the leaves. This problem may be conveniently decomposed into two steps: a first step involving energy minimization for a prescribed distribution of active wells, namely,

$$G_{\boldsymbol{m}}W(\boldsymbol{F}) = \inf_{\{\boldsymbol{a}_i,\lambda_i^{\pm},\boldsymbol{N}_i,\ i\in\mathcal{I}_G\}} \quad \sum_{l\in\mathcal{L}_G} \nu_l W_{m_l}(\boldsymbol{F}_l) \tag{2.30}$$

$$\lambda_i^{\pm} \in [0,\,1], \quad i \in \mathcal{I}_G \tag{2.31}$$

$$|\boldsymbol{N}_i| = 1, \quad i \in \mathcal{I}_G \tag{2.32}$$

followed by the optimization of the active wells, i.e.,

$$GW(\boldsymbol{F}) = \inf_{\{m_l \in \{1,\ldots,M\},\ l \in \mathcal{L}_G\}} G_{\boldsymbol{m}} W(\boldsymbol{F}). \tag{2.33}$$

It should be carefully noted that the minimizers of problem (2.20-2.22) may be such that one or more of the volume fractions $\lambda_i^{\pm}$ take the limiting values of 0 or 1. We shall say that a graph G is *stable* with respect to a macroscopic deformation $\boldsymbol{F}$ if at least one minimizer of (2.20-2.22) is such that

$$\lambda_i^{\pm} \in (0,\, 1), \quad \forall i \in \mathcal{I}_G \tag{2.34}$$

and we shall say that the graph is *unstable* or *critical* otherwise. The presence of sub-trees of zero volume in an unstable graph is an indication that the graph is not 'right' for the macroscopic deformation $\boldsymbol{F}$, i.e., the graph is unable to support a nontrivial microstructure consistent with $\boldsymbol{F}$. Unstable graphs are mathematically contrived and physically inadmissible, and, as such, should be ruled out by some appropriate means. This exclusion may be accomplished, e.g., by the simple device of assigning the offending solutions an infinite energy, which effectively rules them out from consideration; or by defining solutions modulo *null* sub-trees, i.e., sub-trees of vanishing volume. In the present approach, we choose to integrate the exclusion of null sub-trees into the dynamics by which microstructures are evolved, as discussed next.

2.3.2 Microstructural evolution

The problem (2.20-2.22) may be regarded as a partial rank-one convexification of $W(\boldsymbol{F})$ obtained by prescribing the graph G of the test laminates. The full rank-one convexification

follows from the consideration of all possible graphs, i.e.,

$$RW(\boldsymbol{F}) = \inf_{G \in \mathcal{B}} GW(\boldsymbol{F}) \tag{2.35}$$

where, as before, $\mathcal{B}$ is the set of all binary trees. In the particular case of energy densities of the form (2.1), we alternatively have

$$RW(\boldsymbol{F}) = \inf_{\substack{G \in \mathcal{B} \\ \{m_l \in \{1,\ldots,M\},\ l \in \mathcal{L}_G\}}} G_{\boldsymbol{m}} W(\boldsymbol{F}). \tag{2.36}$$

It is clear that this problem exhibits combinatorial complexity as the rank of the test laminates increases, which makes a direct evaluation of (2.35) or (2.36) infeasible in general.

Problems of combinatorial complexity arise in other areas of mathematical physics, such as structural optimization and statistical mechanics. Common approaches to the solution of these problems are to restrict the search to the most 'important' states within phase space, or importance sampling; or to restrict access to phase space by the introduction of some form of dynamics. In this latter approach the states at which the system is evaluated form a sequence, or 'chain', and the next state to be considered is determined from the previous states in the chain. If, for instance, only the previous state is involved in the selection of the new state, a Markov chain is obtained. In problems of energy minimization, a common strategy is to randomly 'flip' the system and accept the flip with probability one if the energy is reduced, and with a small probability if the energy is increased.

In other cases, the system possesses some natural dynamics which may be exploited for computational purposes. A natural dynamics for problem (2.35) may be introduced as follows. Evidently, the relevant phase space for this problem is $\mathcal{B}$, the set of all binary trees, and the aim is to define a flow $G(t)$ in this phase space describing the evolution of

the microstructure along a *deformation processes* $\boldsymbol{F}(t)$. Here and subsequently, the real variable $t \geq 0$ denotes time. A natural dynamics for $G(t)$ is set by the following conditions:

1. $G(t)$ must be stable with respect to $\boldsymbol{F}(t)$.

2. $G(t)$ must be accessible from $G(t^-)$ through a physically admissible transition.

The first condition excludes laminates containing null sub-trees, i.e., sub-trees of zero volume. The second criterion may be regarded as a set of rules for microstructural *refinement* and *unrefinement*.

In order to render these criteria in more concrete terms, we adopt an incremental viewpoint and seek to sample the microstructure at discrete times $t_0 = 0, \ldots, t_n, t_{n+1}, \ldots$. Suppose that the microstructure is known at time t_n and we are given a new macroscopic deformation $\boldsymbol{F}_{n+1} = \boldsymbol{F}(t_{n+1})$. In particular, let G_n be the graph of the microstructure at time t_n. We consider two classes of admissible transitions by which a new structure G_{n+1} may be reached from G_n:

1. The elimination of null sub-trees from the graph of the laminate, or *pruning*.

2. The splitting of leaves, or *branching*.

Specifically, we refer to branching as the process by which a leaf is replaced by a simple laminate. The criterion that we adopt for accepting or rejecting a branching event is simple energy minimization. Thus, let $l \in \mathcal{L}_{G_n}$ be a leaf in the microstructure at time t_n, and let $\boldsymbol{F}_l^n$ be the corresponding deformation. The energetic 'driving force' for branching of the leaf l may be identified with

$$f_l^n = W(\boldsymbol{F}_l^n) - R_1 W(\boldsymbol{F}_l^n) \tag{2.37}$$

where $R_1W(\boldsymbol{F})$ is given by (2.6). We simply accept or reject the branching of the leaf $l \in \mathcal{L}_{G_n}$ according to whether $f_l^n > 0$ or $f_l^n \leq 0$, respectively.

In the particular case in which $W(\boldsymbol{F})$ is of the form (2.1), the evaluation of $R_1W(\boldsymbol{F})$ may be effected by considering all pairs of well energy densities, one for each variant. However, since the well energy densities $W_m(\boldsymbol{F})$ are assumed to be quasiconvex and we rule out variants of zero volume, we may exclude from consideration the cases in which both variants of the laminate are in the same well. The evaluation of $R_1W(\boldsymbol{F})$ is thus reduced to the consideration of all distinct pairs of well energy densities.

The precise sequence of steps followed in calculations are as follows:

1. Initialization: Input $\boldsymbol{F}_{n+1}$, set $G_{n+1} = G_n$.

2. Equilibrium: Equilibrate laminate with G_{n+1} held fixed.

3. Evolution:

   (a) Are there null sub-trees?

      i. `YES:` Prune all null sub-trees, `GOTO` (2).

      ii. `NO:` Continue.

   (b) Compute all driving forces for branching $\{f_l^{n+1},\ l \in \mathcal{L}_{G_{n+1}}\}$.

   Let $f_{l_{\max}}^{n+1} = \max_{l \in \mathcal{L}_{G_{n+1}}} f_l^{n+1}$. Is $f_{l_{\max}}^{n+1} > 0$?

      i. `YES:` Branch leaf $l_{\max}$, `GOTO` (2).

      ii. `NO:` EXIT.

Several remarks are in order. The procedure just described may be regarded as a process of *continuation*, where the new microstructure is required to be close to the existing one in the sense just described. Evidently, since we restrict the class of microstructures which may

arise at the end of each time step, there is no guarantee that this continuation procedure delivers the solution of (2.35) for all $t \geq 0$. However, metastability plays an important role in many systems of interest, and the failure to deliver the absolute rank-one convexification at all times is not of grave concern in these cases. Indeed, the continuation procedure described above may be regarded as a simple model of metastability.

In this regard, several improvements of the model immediately suggest themselves. The branching criterion employed in the foregoing simply rules out branching in the presence of an intervening energy barrier, no matter how small, separating the initial and final states. An improvement over this model would be to allow, with some probability, for transitions requiring an energy barrier to be overcome, e.g., in the spirit of transition state theory and kinetic Monte Carlo methods. However, the implementation of this approach would require a careful and detailed identification of all the paths by which branching may take place, a development which appears not to have been undertaken to date.

2.4 Illustrative examples

As a first illustration of the sequential lamination algorithm presented in the foregoing, we apply it to a simple model of a Cu-Al-Ni shape-memory alloy, a material which has been extensively investigated in the literature (cf. [11, 12, 29, 58], and references therein). Photomicrographs taken from the experiments of Chu and James [29] (also reported by [58]) reveal sharp laminated microstructures, often of rank two or higher. In order to exercise the algorithm, in the examples that follow we simply take the material through a prescribed macroscopic deformation path.

2.4.1 Material model

Cu-Al-Ni undergoes a cubic to orthorhombic martensitic transformation and has, therefore, six variants in the martensitic phase described by the transformation stretches given by (1.8) and (1.9). For purposes of illustration of the sequential lamination algorithm we adopt a simple energy density of the form (2.1), with well energy densities

$$W_0(\boldsymbol{F}) = \frac{1}{8}(\boldsymbol{F}^T\boldsymbol{F} - \boldsymbol{I})\,\mathbb{C}_0\,(\boldsymbol{F}^T\boldsymbol{F} - \boldsymbol{I}) \tag{2.38}$$

for the austenitic phase, and

$$W_m(\boldsymbol{F}) = \frac{1}{8}[(\boldsymbol{F}\boldsymbol{U}_m^{-1})^T(\boldsymbol{F}\boldsymbol{U}_m^{-1}) - \boldsymbol{I}]\,\mathbb{C}_m\,[(\boldsymbol{F}\boldsymbol{U}_m^{-1})^T(\boldsymbol{F}\boldsymbol{U}_m^{-1}) - \boldsymbol{I}], \quad m = 1, \ldots, 6 \tag{2.39}$$

for the martensitic phases. In these expressions $\mathbb{C}_m$, $m = 0, \ldots, M$, are the elastic moduli at the bottom of the variants. These are (in MPa) [79, 85]

$$\mathbb{C}_0 = \begin{pmatrix} C_{11} & C_{12} & C_{12} & 0 & 0 & 0 \\ C_{12} & C_{11} & C_{12} & 0 & 0 & 0 \\ C_{12} & C_{12} & C_{11} & 0 & 0 & 0 \\ 0 & 0 & 0 & C_{44} & 0 & 0 \\ 0 & 0 & 0 & 0 & C_{44} & 0 \\ 0 & 0 & 0 & 0 & 0 & C_{44} \end{pmatrix} \tag{2.40}$$

where $C_{11} = 141.76$, $C_{12} = 126.24$ and $C_{44} = 97$ and

$$\mathbb{C}_1 = \begin{pmatrix} C_{11} & C_{12} & C_{13} & 0 & 0 & 0 \\ C_{12} & C_{22} & C_{23} & 0 & 0 & 0 \\ C_{13} & C_{23} & C_{33} & 0 & 0 & 0 \\ 0 & 0 & 0 & C_{44} & 0 & 0 \\ 0 & 0 & 0 & 0 & C_{55} & 0 \\ 0 & 0 & 0 & 0 & 0 & C_{66} \end{pmatrix} \tag{2.41}$$

where $C_{11} = 189$, $C_{22} = 141$ and $C_{33} = 205$, $C_{12} = 124$, $C_{13} = 45.5$, $C_{23} = 115$, $C_{44} = 54.9$,

$C_{55} = 19.7$, $C_{66} = 62.6$ and with the moduli of the remaining martensitic variants following by symmetry. The energy density defined by (2.1) and (2.39) is material frame indifferent, results in stress-free states at the bottoms of all wells, i.e., at $\boldsymbol{F} = \boldsymbol{I}$ and $\boldsymbol{F} = \boldsymbol{R}\boldsymbol{U}_m$, $\boldsymbol{R} \in SO(3)$, $m = 1, \ldots, 6$, assigns equal energy density to all unstressed variants, and exhibits all the requisite material symmetries.

2.4.2 Optimization

In the examples presented here, and in the finite element calculations presented in the following section, problem (2.20-2.22) is solved using Spellucci's [77] sequential quadratic programming (SQP) algorithm for constrained minimization. The SQP algorithm is an iterative procedure which requires an initial guess in order to start the iteration. In calculations we begin by setting the initial values of $\{\boldsymbol{a}_i, \lambda_i^{\pm}, \boldsymbol{N}_i, i \in \mathcal{I}_{G_{n+1}}\}$ at time t_{n+1} equal to the converged values at time t_n. The main issue arises in evaluating possible branching events, as in this case new interfaces arise for which no previous geometrical information exists. The selection of initial guesses for $\boldsymbol{a}_i$ and $\lambda_i^{\pm}$, $i \in \mathcal{I}_G$, offers no difficulty, and we simply set $\boldsymbol{a}_i = \boldsymbol{0}$ and $\lambda_i^{\pm} = 0$ or 1. The choice of the initial value of the new interface normals $\boldsymbol{N}_i$ requires more care since it strongly biases the resulting microstructure.

We have investigated two ways of initializing the normals $\boldsymbol{N}_i$ arising during branching. A first approach is based on sampling the unit sphere uniformly. Thus, we simply select initial values of $\boldsymbol{N}_i$ uniformly distributed over the unit sphere with some prespecified density and select the solution which results in the least energy. If two or more branched configurations possess the same energy, we select one at random. This exhaustive search approach is effective but costly owing to the large number of cases which need to be considered.

The second approach consists of priming the iteration using an initial guess derived from

Ball and James [11, 12] constrained theory for shape-memory materials. In this theory, the elastic moduli are presumed large compared to the transformation stresses, so that the geometry of the laminate can be obtained, to a first approximation, directly from the transformation strains. Conveniently, all resulting twinning relations between every distinct pair of martensitic wells can be tabulated beforehand. For Cu-Al-Ni this tabulation has been carried out by Bhattacharya, Li and Luskin [21], with the solutions given by (1.15) and (1.16) with use of Table 1.1. These results from the constrained theory may conveniently be used to start a branching calculation when the energy density is of the form (2.1). In this case, the branching calculation entails the consideration of every pair of well energy densities $W_m(\boldsymbol{F})$ and $W_n(\boldsymbol{F})$, $m, n = 1, \ldots, 6$, $m \neq n$, in the new leaves. The attendant iteration may then be started from the constrained solutions $\{\boldsymbol{a}, \boldsymbol{N}\}$ described above, with the initial value of $\lambda^{\pm}$ determined by means of a line search.

2.4.3 Martensite–martensite transition

Our first test case concerns the macroscopic deformation process

$$\boldsymbol{F}(t) = (1-t)\boldsymbol{U}_3 + t\boldsymbol{U}_4, \quad t \in [0,\, 1] \tag{2.42}$$

which takes the material from one variant of martensite to another. Fig. 2.3 shows the evolution of the energy, the component P_{13} of the first Piola-Kirchhoff stress, and the volume fraction λ of $\boldsymbol{U}_4$, respectively, for the unrelaxed and relaxed cases. In the calculations to follow the branching constructions employ the constrained geometry as an initial guess, as discussed in the foregoing.

The unrelaxed response shown in Fig. 2.3 exhibits an abrupt transition from the initial to

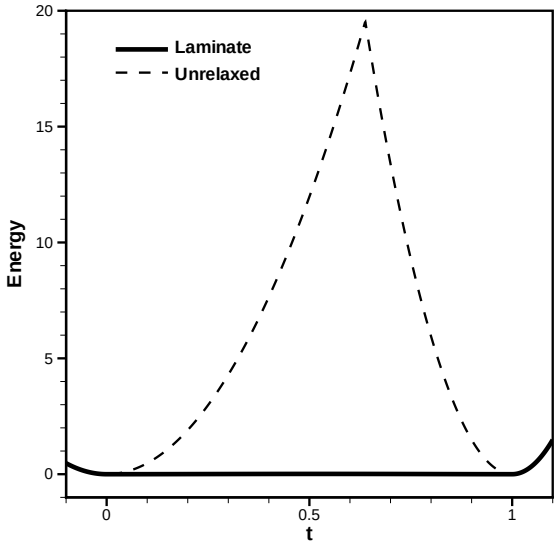

(a)

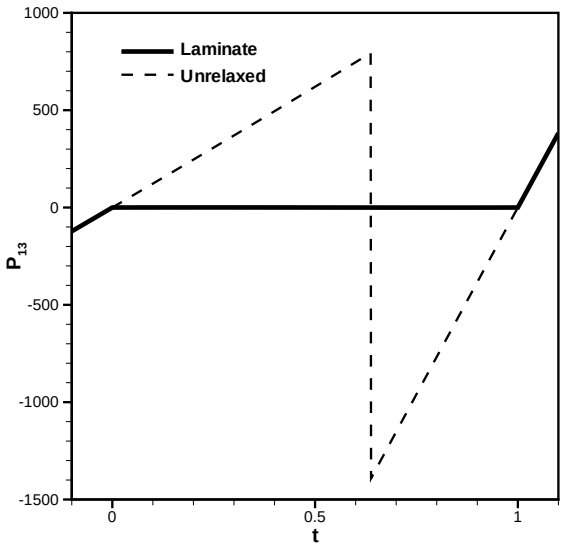

(b)

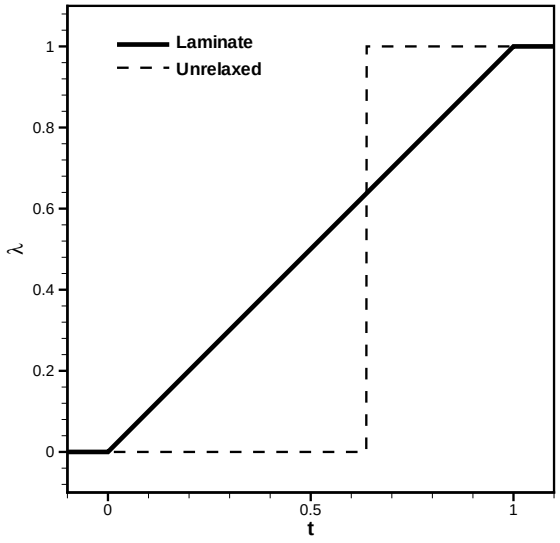

(c)

Figure 2.3: Martensite-to-martensite transition example. Comparison of unrelaxed and relaxed (a) energies, (b) stresses, and (c) volume fractions.

the final variant, as no mixed states are allowed to develop during the deformation process. By contrast, the relaxation algorithm results in the development of a rank-one laminate immediately following the onset of deformation. It should be carefully noted that the material is allowed to develop laminates of arbitrary rank, and that the persistency of a rank-one laminate is due to the fact that both leaves are stable against branching. The computed volume fraction λ increases linearly from 0 to 1. As a result of this evolving microstructure, the energy of the material is fully relaxed, and the material remains unstressed. In this example, the unloading response exactly traces in reverse the loading response, and hence no hysteresis is recorded.

2.4.4 Simple shear

Our second test case concerns macroscopic simple shear on the plane (010) and in the direction (100). The material is taken to be initially undeformed. The shear deformation is increased from zero up to a maximum value and then decreased back to zero. The calculations are carried out excluding the austenitic well from the definition (2.1) of the energy and considering the six martensitic wells only.

Fig. 2.4b shows a comparison of the computed unrelaxed and relaxed energies. By the exclusion of the austenitic well the material is forced to develop a rank-five laminate in its initial undeformed configuration. The graph of this laminate, and of all laminates which subsequently arise during deformation, is shown inlaid in Fig. 2.4a. As is evident from Fig. 2.4b, the relaxation algorithm ostensibly succeeds at fully relaxing the energy of the material. With increasing deformation, the computed microstructure undergoes transitions to rank-four and three laminates. A first rank-three laminate of order thirteen is first predicted which subsequently simplifies to a rank-three laminate of order seven.

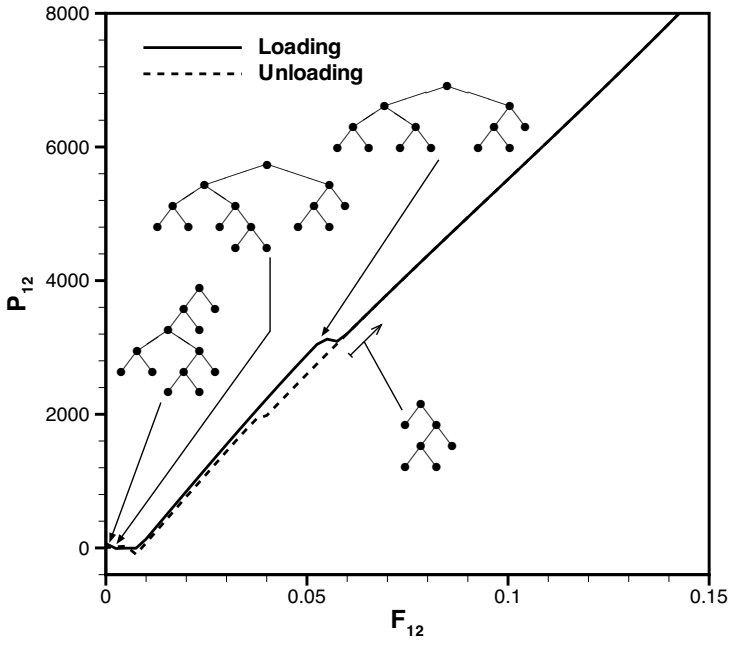

(a)

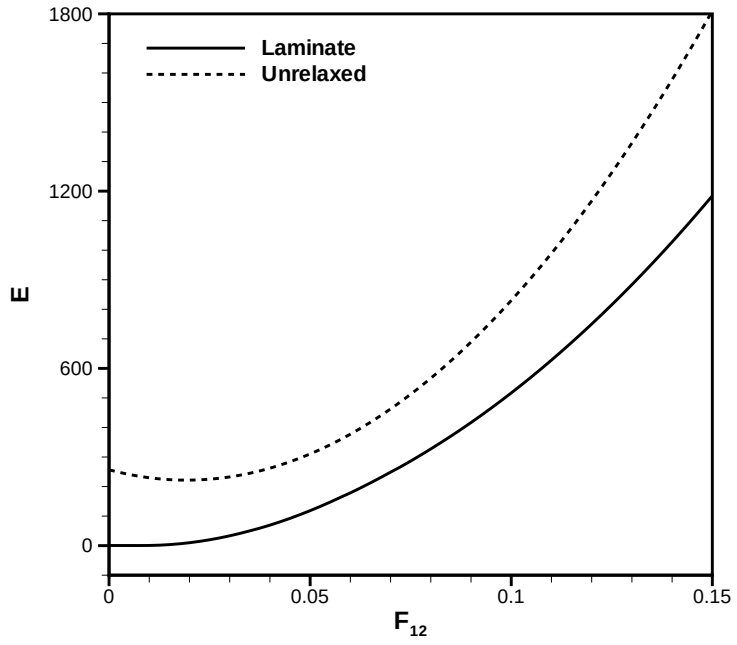

(b)

Figure 2.4: Simple shear example. a) P_{12} component of the first Piola-Kirchhoff stress tensor. The graph of the microstructures predicted by the relaxation algorithm are also shown inlaid. b) Unrelaxed and relaxed energies during loading.

As a result of this microstructural evolution, the relaxed energy remains well below the unrelaxed energy through the deformation, Fig. 2.4b. Upon unloading, the order-seven rank-three laminate is maintained down to zero deformation, suggesting that the initial microstructures computed during loading are metastable. Indeed, the unloading stress-strain curve lies below the loading one, resulting in a certain amount of hysteresis, which suggests that the order-seven rank-three laminate is indeed more efficient than the precursor microstructures.

2.5 Nonlocal extension

The simple branching criterion (2.37), which accounts for the energies of the variants only, neglects any energy barriers that may oppose the transformation and may lead to runaway refinement of the microstructure. In order to limit branching and, additionally, to estimate the size of the microstructure, we follow Ball and James [11] and take into consideration two additional sources of energy: the energy of the twin boundaries, and the mismatch energy contained within the boundary layers separating pairs of leaves. For instance, Boullay et al. [24], and James et al. [50] have investigated in detail the structure of branched needle microstructures that develop within the misfit boundary layers, e.g., at the edge of a martensite laminate. Such level of detail is well beyond the scope of this work. Our aim here is to derive a rough estimate of the misfit energy amenable to a straightforward calculation.

One such simple estimate may be derived as follows. Begin by enforcing 'rigid-device' boundary conditions

$$\boldsymbol{y}^{\mathrm{BL}} = \boldsymbol{y}_0 + \bar{\boldsymbol{F}}(\boldsymbol{x} - \boldsymbol{x}_0), \qquad x_3 = 0 \tag{2.43}$$

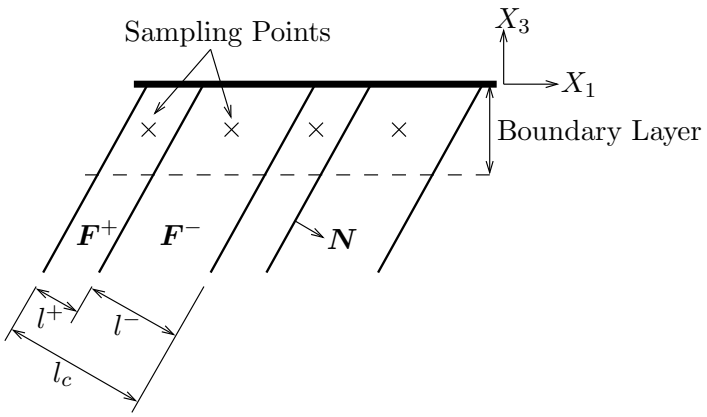

Figure 2.5: Schematic of interpolation boundary layer and scheme used to estimate misfit energy.

where $\bar{\boldsymbol{F}}$ is the average deformation in the laminate, $\boldsymbol{x}_0$ is a material point within the reference configuration of the laminate, and $\boldsymbol{y}_0 = \boldsymbol{y}(\boldsymbol{x}_0)$ is its position on the deformed configuration. This insulates the laminate from the details of the adjacent deformation field in the regions $x_3 > 0$ and $x_3 < -l$. A simple interpolating deformation mapping is then

$$\boldsymbol{y}^{\mathrm{BL}}(\boldsymbol{x}) = \boldsymbol{y}_0 - (\boldsymbol{y}(\boldsymbol{x}) - \boldsymbol{y}_0)\frac{x_3}{\Delta} + \bar{\boldsymbol{F}}(\boldsymbol{x} - \boldsymbol{x}_0)\left(1 + \frac{x_3}{\Delta}\right), \qquad -\Delta \leq x_3 \leq 0 \tag{2.44}$$

where $\boldsymbol{y}(\boldsymbol{x})$ is the deformation mapping of the laminate, and Δ is the boundary layer thickness. The boundary layer at $x_3 = -l$ can be given an identical treatment. The corresponding deformation gradient is

$$\boldsymbol{F}^{\mathrm{BL}}(\boldsymbol{x}) = -\boldsymbol{F}(\boldsymbol{x})\frac{x_3}{\Delta} + \bar{\boldsymbol{F}}\left(1 + \frac{x_3}{\Delta}\right) + \frac{1}{\Delta}[\bar{\boldsymbol{F}}(\boldsymbol{x} - \boldsymbol{x}_0) - (\boldsymbol{y}(\boldsymbol{x}) - \boldsymbol{y}_0)] \otimes \boldsymbol{e}_3. \tag{2.45}$$

We proceed to estimate the elastic energy of the region defined by the intersection of each variant with the boundary layer by a simple one-point quadrature rule. Let $\boldsymbol{x}^{\pm}$ be a pair of consecutive sampling points, Fig. 2.5, chosen such that $x_3^{\pm} = -\Delta/2$, and select $\boldsymbol{x}_0 = \boldsymbol{x}^-$

for simplicity. Then, it follows immediately from (2.45) that

$$\boldsymbol{F}^{\mathrm{BL}-} \equiv \boldsymbol{F}^{\mathrm{BL}}(\boldsymbol{x}^-) = \frac{1}{2}(\boldsymbol{F}^- + \bar{\boldsymbol{F}}). \tag{2.46}$$

Likewise,

$$\boldsymbol{F}^{\mathrm{BL}+} \equiv \boldsymbol{F}^{\mathrm{BL}}(\boldsymbol{x}^+) = \frac{1}{2}(\boldsymbol{F}^+ + \bar{\boldsymbol{F}}) + [\bar{\boldsymbol{F}}(\boldsymbol{x}^+ - \boldsymbol{x}^-) - (\boldsymbol{y}^+ - \boldsymbol{y}^-)] \otimes \boldsymbol{e}_3. \tag{2.47}$$

But, since $\boldsymbol{y}(\boldsymbol{x})$ is piecewise linear, it follows that

$$\boldsymbol{y}^+ - \boldsymbol{y}^- = \boldsymbol{F}^-(\lambda^-(\boldsymbol{x}^+ - \boldsymbol{x}^-)) + \boldsymbol{F}^+(\lambda^+(\boldsymbol{x}^+ - \boldsymbol{x}^-)) = \bar{\boldsymbol{F}}(\boldsymbol{x}^+ - \boldsymbol{x}^-) \tag{2.48}$$

and

$$\boldsymbol{F}^{\mathrm{BL}+} = \frac{1}{2}(\boldsymbol{F}^+ + \bar{\boldsymbol{F}}). \tag{2.49}$$

Collecting the above results we finally have

$$\boldsymbol{F}^{\mathrm{BL}\pm} = \frac{1}{2}(\boldsymbol{F}^\pm + \bar{\boldsymbol{F}}). \tag{2.50}$$

Within this approximation, the misfit boundary-layer energy density finally evaluates to

$$W^{\mathrm{BL}} = \lambda^-[W(\boldsymbol{F}^{\mathrm{BL}-}) - W(\boldsymbol{F}^-)] + \lambda^+[W(\boldsymbol{F}^{\mathrm{BL}+}) - W(\boldsymbol{F}^+)] \tag{2.51}$$

which furnishes a remarkably simple (though rough) estimate. We note that

$$\boldsymbol{F}^{\mathrm{BL}+} - \boldsymbol{F}^{\mathrm{BL}-} = \frac{1}{2}(\boldsymbol{F}^+ - \boldsymbol{F}^-) = \frac{1}{2}\boldsymbol{a} \otimes \boldsymbol{N} \tag{2.52}$$

and

$$\lambda^{-}\boldsymbol{F}^{\mathrm{BL}-} + \lambda^{+}\boldsymbol{F}^{\mathrm{BL}+} = \bar{\boldsymbol{F}}. \tag{2.53}$$

Thus, the deformations $\boldsymbol{F}^{\mathrm{BL}\pm}$ are rank-one compatible and match the average deformation of the laminate. Since the deformations $\boldsymbol{F}^{\pm}$ minimize the energy of the laminate among all rank-one laminates with average deformation $\bar{\boldsymbol{F}}$, it follows that $W^{\mathrm{BL}} \geq 0$, i.e., W^{BL} does indeed represents an *excess energy*.

For simplicity, we assume that the twin-boundary energy Γ per unit area is a constant independent of the deformation of the variants. Combining the preceding estimates, it follows that the total excess or *nonlocal* energy due to the twin boundaries and the misfit boundary layers contained within a region of the laminate of dimensions $L \times L \times l$ is

$$E^{\mathrm{NL}} = L^2 l \left\{ \frac{\Gamma}{l^c} + \frac{2\Delta}{l} W^{\mathrm{BL}} \right\}. \tag{2.54}$$

Taking $\Delta = l^c/2$, for definiteness, this expression reduces to

$$E^{\mathrm{NL}} = L^2 l \left\{ \frac{\Gamma}{l^c} + \frac{l^c}{l} W^{\mathrm{BL}} \right\}. \tag{2.55}$$

This excess energy may now be minimized with respect to l^c, with the result

$$l^c = \sqrt{\frac{\Gamma l}{W^{\mathrm{BL}}}} \tag{2.56}$$

which affords an estimate of l^c. The corresponding minimum excess energy per unit volume is

$$W^{\mathrm{NL}} \equiv \frac{E^{\mathrm{NL}}}{L^2 l} = 2\sqrt{\frac{\Gamma W^{\mathrm{BL}}}{l}}. \tag{2.57}$$

We note that this excess energy grows as $l^{-1/2}$, which tends to suppress microstructural refinement. In calculations, we interpret the excess energy density W^{NL} as an energy barrier for branching. Consideration of this energy barrier has the effect of reducing the local branching driving force (2.37) to

$$f_l^n = W(\boldsymbol{F}_l^n) - R_1 W(\boldsymbol{F}_l^n) - W^{\mathrm{NL}}(\boldsymbol{F}_l^n) \tag{2.58}$$

which effectively introduces a lower cut-off for the size of the microstructure and eliminates the possibility of runaway microstructural refinement.

2.6 Finite-element simulation of indentation in Cu-Al-Ni

The sequential lamination algorithm developed in the foregoing may conveniently be taken as a basis for multiscale simulation in situations in which there is a strict separation of scales: a macroscopic scale characterized by slowly-varying smooth fields; and a much smaller scale commensurate with the size of the evolving microstructure. As remarked by several authors [25, 27, 34, 58], these problems may be solved effectively by pushing the microstructure to the *subgrid* scale, while solving the well-posed relaxed problem on the computational grid.

In this section we present an example of the application of this multiscale approach in which the macroscopic problem is solved by the finite-element method, while the effective behavior is computed, simultaneously with the macroscopic solution, at the Gauss-point level using the sequential lamination algorithm developed in the foregoing. The particular problem considered concerns the quasistatic normal indentation of a Cu-Al-Ni shape-memory alloy by a spherical indenter. The domain of analysis and the computational mesh are shown in Fig. 2.6. The analysis is reduced to one quarter of the entire domain for sim-

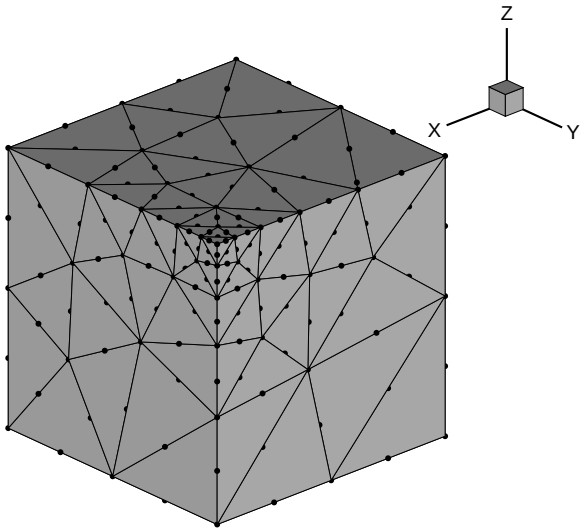

Figure 2.6: Computational domain and finite element mesh.

plicity. In particular, solutions exhibiting broken symmetry are ruled out by the analysis. The size of the computational domain is 20 mm $\times$ 20 mm $\times$ 20 mm. The radius of the indenter is 15 mm. The specimen is fully supported over its entire base, and the remainder of its boundary is free of tractions. The computational mesh contains 254 nodes and 105 ten-node quadratic tetrahedral elements. Contact between the indenter and the specimen is assumed to be frictionless and is enforced by a penalty method [67]. To ensure that the jacobian J of the deformation remains positive in all variants at all times, the simple energy of each well is augmented by a term of the form [62]

$$W^{\mathrm{vol}}(J) = \begin{cases} C(J^2 + J^{-2} - 2)^2, & J < 1 \\ 0, & \text{otherwise} \end{cases} \tag{2.59}$$

where C is a constant chosen sufficiently small to minimize the effect on the total energy. By design, $W^{\mathrm{vol}}(J)$ and its first and second derivatives vanish at $J = 1$. In addition, the twin-boundary and misfit energies are accounted for as part of the branching criterion as a means

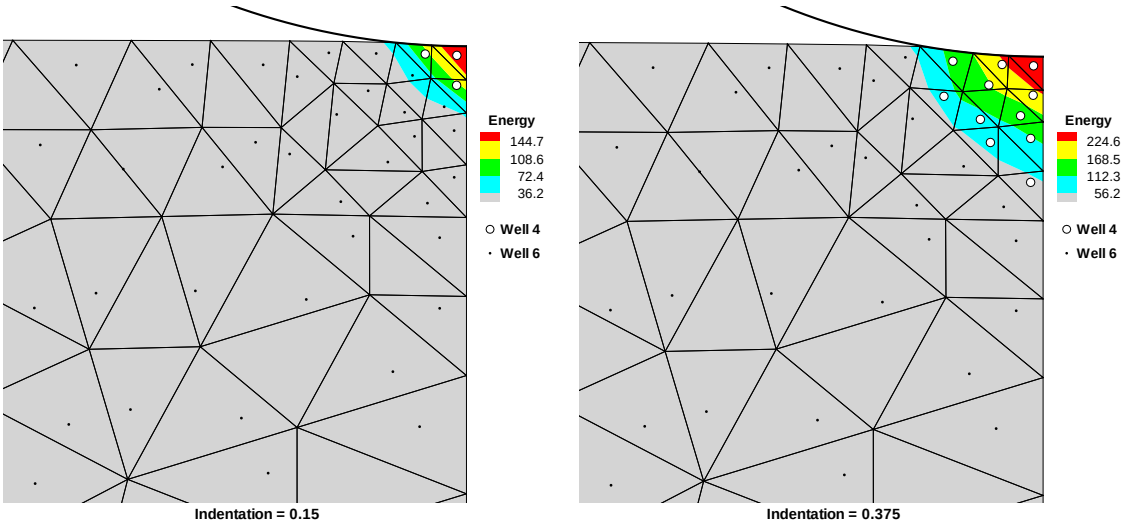

(a) (b)

Figure 2.7: Cross sections and energy-density contours for two unrelaxed solutions at depths of indentation: a) 0.150 mm, and b) 0.375 mm. The symbols designate the energy well which is activated at each Gauss point of the mesh.

of introducing a lower cutoff for the laminate size and preventing runaway microstructural refinement. In all calculations, the twin-boundary energy per unit area Γ is set to 1 J/m^2. The maximum size of the laminate at a particular Gauss point is set to the element size.

The finite-element solution is obtained by dynamic relaxation followed by a preconditioned conjugate-gradient iteration [73]. The high level of concurrency in the constitutive calculations was exploited via an MPI-based parallel implementation [66] on the ASCI Blue multiprocessing computer. Performance studies showed excellent load balancing and scalability.

Fig. 2.7 shows the *unrelaxed* deformed configurations, and the corresponding distribution of active energy wells at the Gauss points of the mesh, at depths of indentation of 0.150 and 0.375 mm. As is evident from this figure, two energy wells become active during indentation. The transformed zone under the indenter grows with depth of indentation, but the fineness

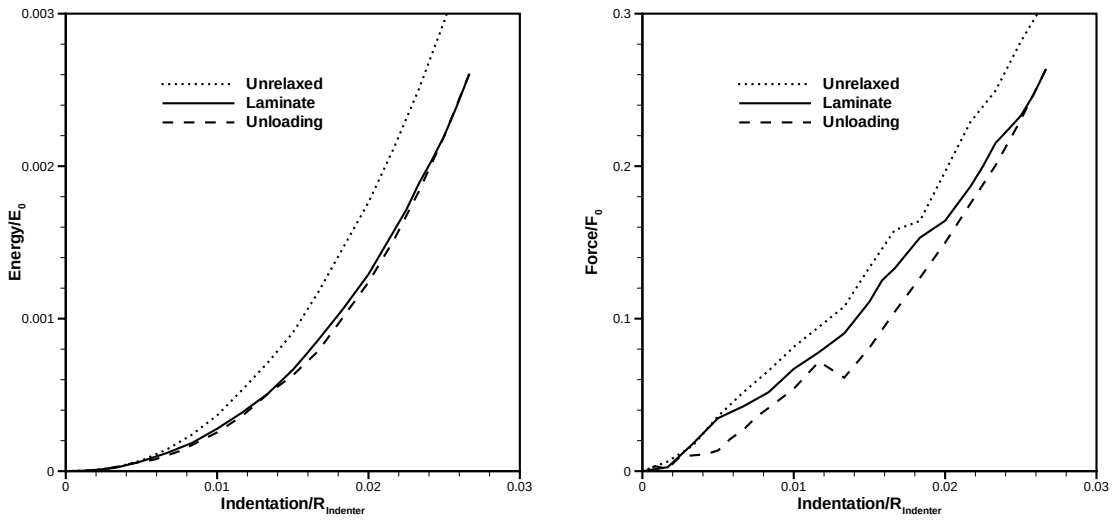

(a) (b)

Figure 2.8: a) Normalized total energy vs. normalized depth of indentation; b) Normalized indentation force vs. normalized depth of indentation.

of the variant arrangement is severely limited by the mesh size. Correspondingly, the total energies and indentation forces recorded during indentation are comparatively high, Fig. 2.8. In this figure the energy has been normalized by $E_0 = V_0 C_{11}^{Austenite}$, where V_0 is the volume of the undeformed specimen, while the force has been normalized by $F_0 = E_0/R_{Indenter}$.

The *relaxed* solution obtained using the sequential lamination algorithm differs markedly from the unrelaxed solution just described, Fig. 2.9. Thus, the relaxed deformation field is accompanied by the development of well-defined microstructures at the subgrid level. Some of the laminates generated by the sequential lamination algorithm are quite complex, reaching rank two. Of note is the appearance of a de-twinned zone directly under the indenter. The effect of relaxation on the total energy and indentation force is quite marked, Fig. 2.8, with the relaxed values lying well below the unrelaxed ones. Unloading exhibits the path-dependent nature of the algorithm, with the microstructure established at maximum

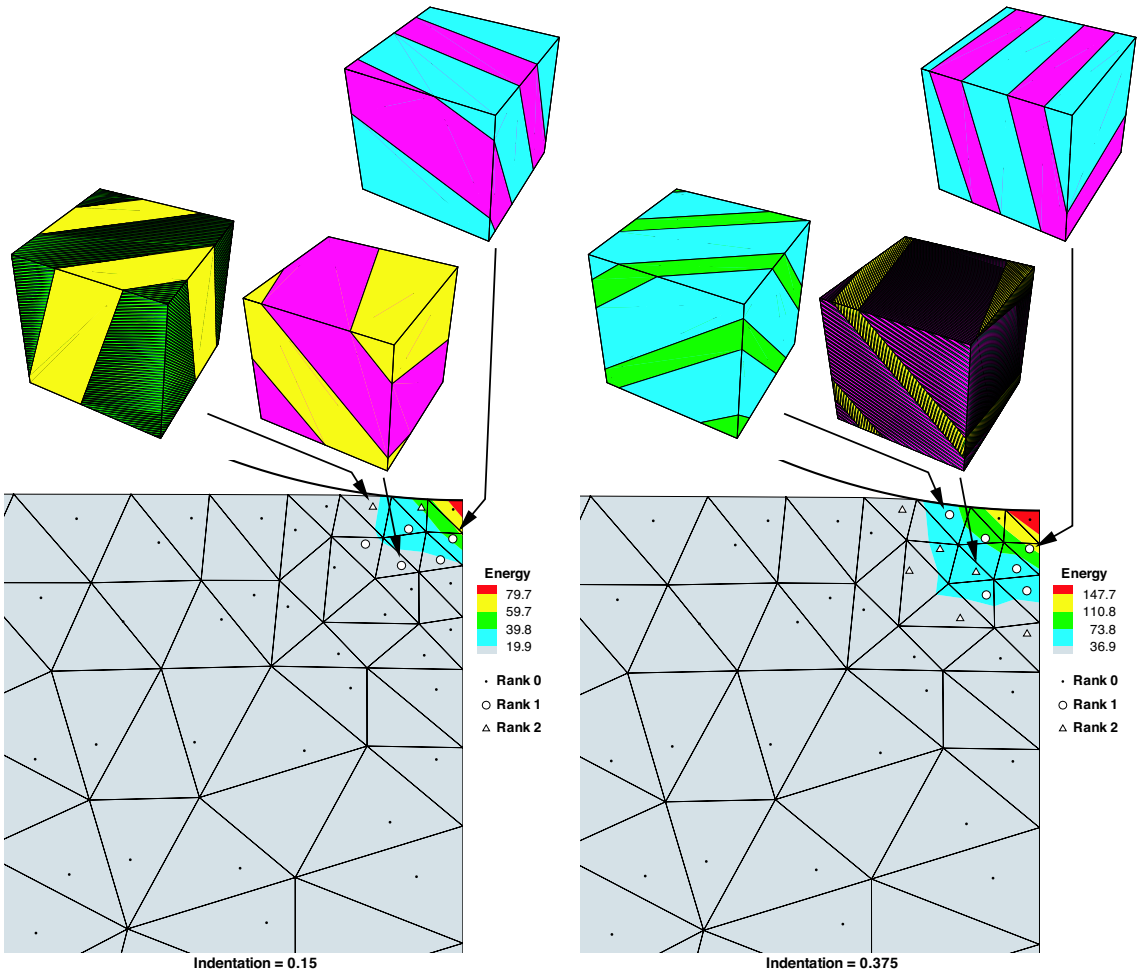

(a) (b)

Figure 2.9: Cross section and energy-density contours for relaxed solution at an indentation depth of: a) 0.150 mm, and b) 0.375 mm. The symbols indicate the rank of the microstructure at the Gauss points. The insets depict the geometry of the microstructure at the indicated sampling points, with each color representing an individual well, and are of identical size oriented such that the left face corresponds to the cross section plane.

load remaining in place during much of the unloading process, which in turn results in a soft response. The fineness of the microstructure is somewhat overpredicted by the calculations, with some of the variants attaining sub-micron thicknesses. In view of (2.56), this excessive refinement may owe to a low value of the twin-boundary energy Γ, or to an overestimation of the misfit energy W^{BL}, or both.

2.7 Summary and concluding remarks

We have presented a practical algorithm for partially relaxing multiwell energy densities. The algorithm is based on sequential lamination, but it is constrained in such a way that successive microstructures occurring along a deformation path are close to each other in a certain sense: the new microstructure should be reachable from the preceding one by a combination of branching and pruning operations. All microstructures generated by the algorithm are in static and configurational equilibrium. In particular, we optimize all the interface orientations and variant volume fractions, with the result that all configurational forces and torques are in equilibrium. We additionally allow the variants to be arbitrarily stressed and enforce traction equilibrium across all interfaces. Owing to the continuity constraint imposed upon the microstructural evolution, the predicted material behavior may be path-dependent and exhibit hysteresis.

In cases in which there is a strict separation of micro and macrostructural length scales, the proposed relaxation algorithm may effectively be integrated into macroscopic finite-element calculations at the subgrid level. We have demonstrated this aspect of the algorithm by means of a numerical example concerned with the indentation of a Cu-Al-Ni shape memory alloy [29] by a spherical indenter. The calculations illustrate the ability of the algorithm to generate complex microstructures, resulting in force–depth of indentation

curves considerably softer than otherwise obtained by direct energy minimization.

Several improvements to the present approach immediately suggest themselves. The relaxation algorithm, in its present form, does not account for energy barriers for branching. Thus, a significant improvement over this model would be to permit, with probability less than one, transitions requiring an energy barrier to be overcome, e.g., in the spirit of transition state theory and kinetic Monte Carlo methods. This extension would require a careful and detailed identification of all the paths by which branching may take place, and the attendant energy barriers. Another significant improvement would be to relax the configurational force equilibrium constraint and replace it by a kinetic relation governing interfacial motion [2, 3, 75]. Kinetic relations of this form can effectively be integrated into the variational principle with the aid of time discretization [63, 65].

Chapter 3

Algorithm verification

3.1 Introduction

This chapter is concerned with the verification of the lamination algorithm detailed in Chapter 2. The algorithm will be applied to four problems and the results compared to the known analytic solutions.

The first problem consists of three pairwise rank-one compatible wells representing anti-plane shears [72]. As the transformation stretches differ by a rank-one matrix, satisfying the twinning equation, it is expected to be an uncomplicated initial verification. The second model, studied by several authors including [8, 20, 83], involves four incompatible wells with an analytic relaxation that involves infinite rank laminations. This is a popular benchmark problem, with the algorithms of Dolzmann and Walkington [36, 39] and Aranda and Pedregal [5] both obtaining the exact result with recourse to statistical optimization approaches. The next verification test considers a model for nematic elastomers [35]. In contrast to the solutions considered previously, the energy consists of a single nonconvex well. The final calculation, a constitutive model for polycarbonate, also possesses a nonconvex well that, in addition to being relaxed itself, forms laminations with a second convex well [41]. These particular examples were chosen to provide a breadth of applications, without revisiting the

two-well problem considered in §2.4.3.

To solve these problems with the lamination algorithm we require an energy functional. For simplicity, the energy functional for each well in the first two problems was chosen to be

$$W(\boldsymbol{F}) = C\,\mathrm{trace}(\boldsymbol{B}^T\boldsymbol{B}) \tag{3.1}$$

with associated first Piola-Kirchoff stress

$$\boldsymbol{P}(\boldsymbol{F}) = 2C\boldsymbol{B} \tag{3.2}$$

where $\boldsymbol{B} \equiv \boldsymbol{F} - \boldsymbol{U}_i$, $\boldsymbol{U}_i$ are the well locations, and C is a constant. The third and fourth examples use different energy functionals, discussed later.

Additionally, the algorithm requires an initial guess for the lamination variables λ, $\boldsymbol{a}$, and $\boldsymbol{N}$ for each new branch, given the variants of the leaves. While λ can be found via a line search, the values of $\boldsymbol{a}$ and $\boldsymbol{N}$ are problem specific and will be discussed below.

The surface energy detailed in §2.5 is not relevant here and was not included.

3.2 Three-well model

The first verification test is a three-well problem related to twinning in BCC crystals (see [72] and references therein). While the general two-well problem has been studied for some time, e.g., [25, 38, 55, 61], with a solution in the linearized case first given by Kohn [52], the three-well problem is significantly more difficult [52], only recently yielding a solution [76]. The problem under consideration here is less general, with the three wells pairwise rank-one connected, i.e., they differ by a matrix of rank one without the need for the rotation $\boldsymbol{R}$ as

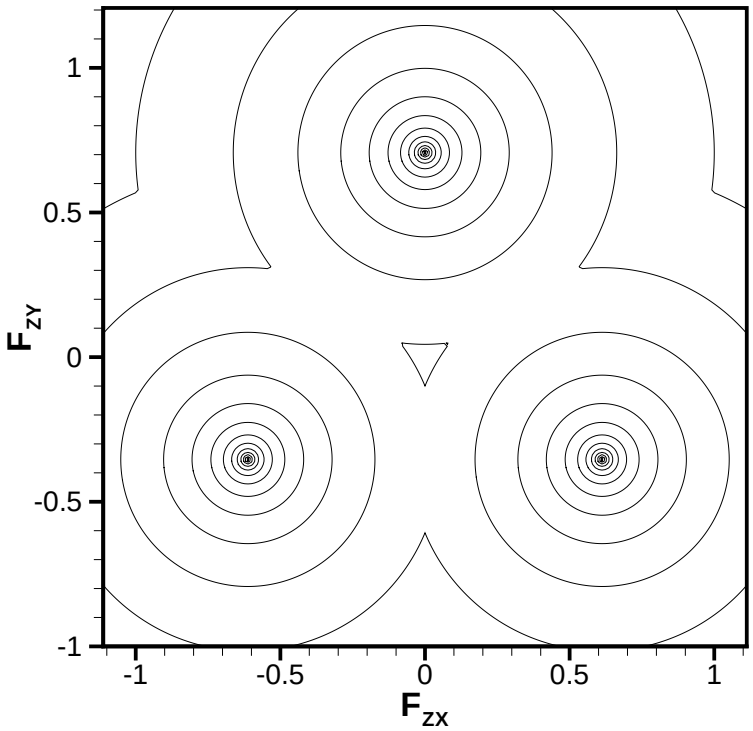

Figure 3.1: Contours of the unrelaxed energy for the three-well model. Note that the energy scale is logarithmic.

in (1.7).

For the present problem, the wells correspond to the three twinning shears, with the crystal lattice oriented such that they are anti-plane shears

$$\boldsymbol{U}_1 = \begin{pmatrix} 1 & 0 & 0 \\ 0 & 1 & 0 \\ 0 & \xi & 1 \end{pmatrix}, \quad \boldsymbol{U}_2 = \begin{pmatrix} 1 & 0 & 0 \\ 0 & 1 & 0 \\ -\frac{\sqrt{3}}{2}\xi & -\frac{1}{2}\xi & 1 \end{pmatrix}, \quad \boldsymbol{U}_3 = \begin{pmatrix} 1 & 0 & 0 \\ 0 & 1 & 0 \\ \frac{\sqrt{3}}{2}\xi & -\frac{1}{2}\xi & 1 \end{pmatrix}, \tag{3.3}$$

where $\xi = 1/\sqrt{2}$ is the magnitude of the twinning shear. This energy is illustrated in Fig. 3.1 for the energy functional given above. Note that here we are not including the undeformed variant at the origin.

We now require an initial guess for the optimization of new branches. As the variants

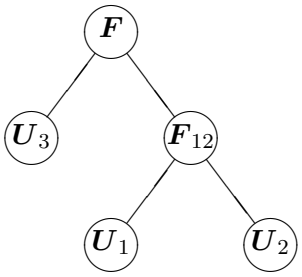

Figure 3.2: Tree representation of a solution to three rank-one connected wells.

are rank-one connected, we can express the difference between each pair of matrices with respect to $\{\boldsymbol{a}, \boldsymbol{N}\}$ as required

$$\boldsymbol{U}_i - \boldsymbol{U}_j = \boldsymbol{a}_{ij} \otimes \boldsymbol{N}_{ij}. \tag{3.4}$$

This yields the value

$$\boldsymbol{a} = (0, 0, \sqrt{3/2}) \tag{3.5}$$

for every pair of wells, with $\boldsymbol{N}$ given in Table 3.1.

wells	1	2	3
1		$(\frac{1}{2}, \frac{\sqrt{3}}{2}, 0)$	$(-\frac{1}{2}, \frac{\sqrt{3}}{2}, 0)$
2	$(-\frac{1}{2}, -\frac{\sqrt{3}}{2}, 0)$		$(-1, 0, 0)$
3	$(\frac{1}{2}, -\frac{\sqrt{3}}{2}, 0)$	$(1, 0, 0)$	

Table 3.1: Initial guess $\boldsymbol{N}$ for lamination between the indicated wells for the three-well problem.

It is known that three pairwise rank-one connected wells can be fully relaxed inside their convex hull [26]. This can be demonstrated by constructing the microstructure illustrated in Fig. 3.2 for $\boldsymbol{F}$ in the convex hull of $\boldsymbol{U}_i$. The deformation $\boldsymbol{F}_{12}$ can be constructed via

$$\boldsymbol{F}_{12} = \boldsymbol{U}_1 + \lambda \boldsymbol{a} \otimes \boldsymbol{N} = \boldsymbol{U}_2 - (1 - \lambda) \boldsymbol{a} \otimes \boldsymbol{N} \tag{3.6}$$

for an arbitrary $\boldsymbol{F}_{12}$ that is a convex combination of $\boldsymbol{U}_1$ and $\boldsymbol{U}_2$. We then wish to show

that this resulting deformation is rank-one compatible with the remaining well $\boldsymbol{U}_3$, i.e, that

$$\text{rank}(\boldsymbol{F}_{12} - \boldsymbol{U}_3) = 1 \tag{3.7}$$

thus allowing the construction of the illustrated zero energy microstructure. Substituting one half of (3.6) into (3.7)

$$\text{rank}(\boldsymbol{F}_{12} - \boldsymbol{U}_3) = \text{rank}(\boldsymbol{U}_1 + \lambda \boldsymbol{a} \otimes \boldsymbol{N} - \boldsymbol{U}_3) \tag{3.8}$$

and then using the pairwise connection between $\boldsymbol{U}_1$ and $\boldsymbol{U}_3$ allows this to be simplified to

$$\text{rank}(\boldsymbol{F}_{12} - \boldsymbol{U}_3) = \text{rank}(\boldsymbol{b} \otimes \boldsymbol{M} + \lambda \boldsymbol{a} \otimes \boldsymbol{N}) \tag{3.9}$$

where $\boldsymbol{U}_1 - \boldsymbol{U}_3 = \boldsymbol{b} \otimes \boldsymbol{M}$. Chipot et al. [26] showed that for a lamination of pairwise connected wells, either all of the associated shear vectors $\boldsymbol{a}$ or normals $\boldsymbol{N}$ must be parallel. For this specific problem, (3.5) indicates that $\boldsymbol{a} = \boldsymbol{b}$ in (3.9). Using this relation with (3.9) yields the required result.

The above fully relaxed construction was obtained exactly by the lamination algorithm, as illustrated in Fig. 3.3.

3.3 Four-well model

The next problem under consideration is the four-well problem, detailed in Müller [60] and references therein. This problem has been studied independently by several authors

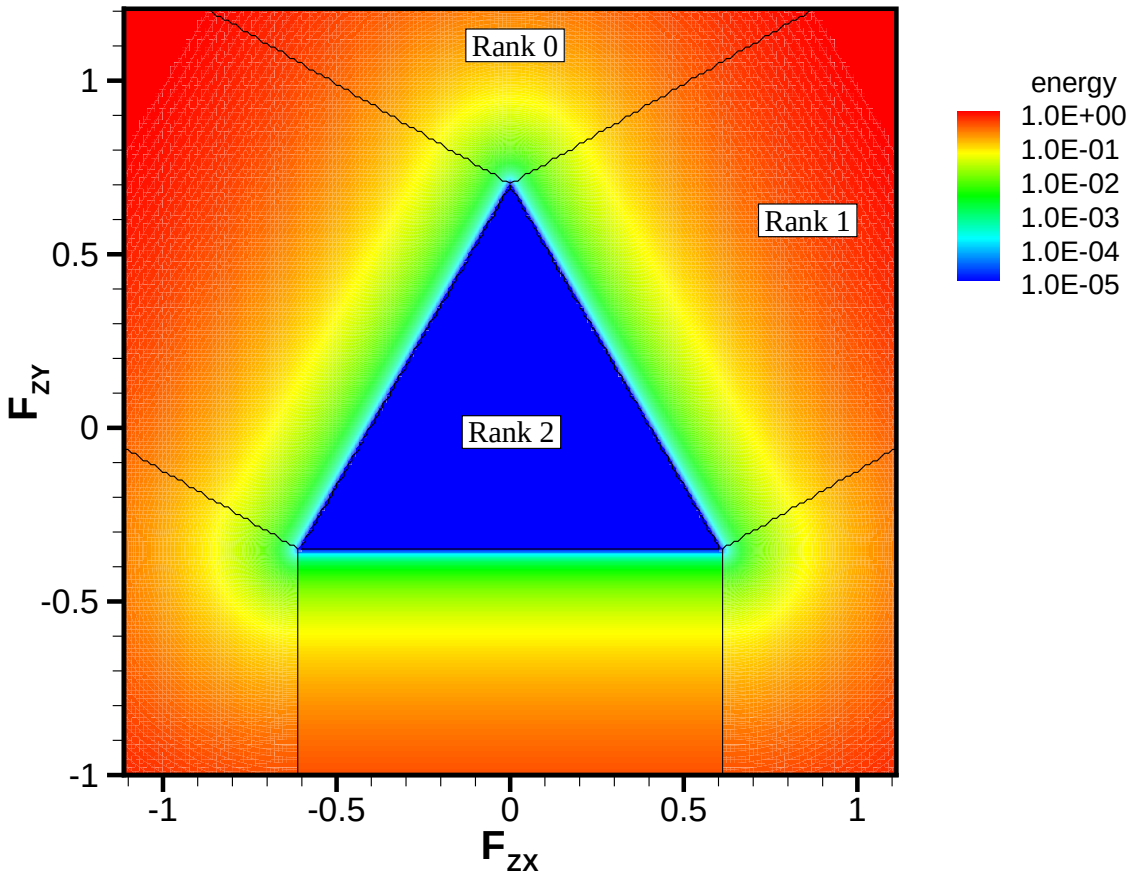

Figure 3.3: Laminate energy obtained for three-well model. The lines are contours of laminate rank, as indicated, while the colors are energy contours on a logarithmic scale.

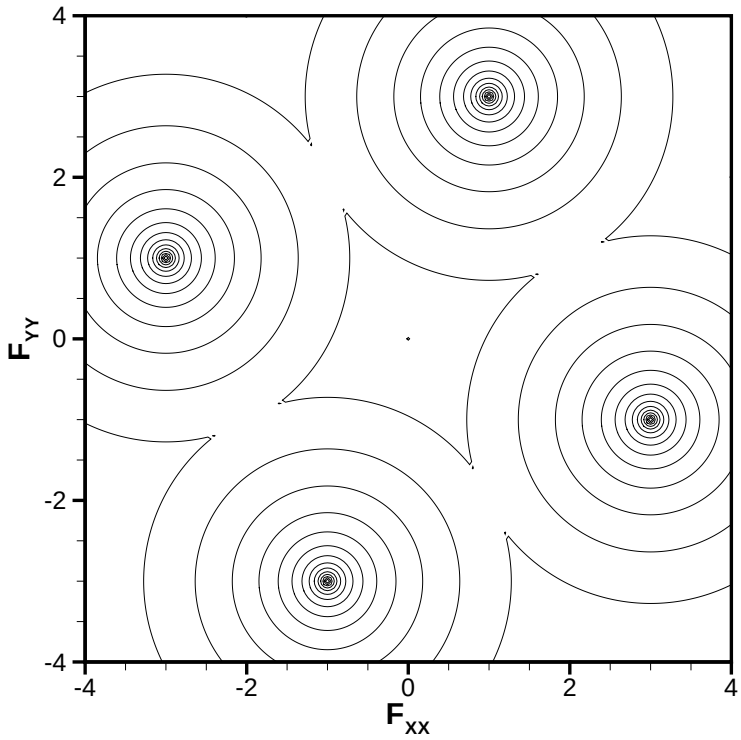

Figure 3.4: Contours of the unrelaxed energy for the four-well model. The energy is on a logarithmic scale with a value of 10.0 at $\boldsymbol{F}_{xx} = \boldsymbol{F}_{yy} = 0$.

including [5, 8, 20, 36, 39, 83], and consists of the four two-dimensional diagonal matrices:

$$\begin{aligned} \boldsymbol{A}_1 &= -\boldsymbol{A}_3 = \mathrm{diag}(-1, -3) \\ \boldsymbol{A}_2 &= -\boldsymbol{A}_4 = \mathrm{diag}(-3, 1) \end{aligned} \tag{3.10}$$

illustrated in Fig. 3.4 using the aforementioned energy functional. Note that the wells are not rank-one connected, i.e., $\mathrm{rank}(\boldsymbol{A}_i - \boldsymbol{A}_j) \neq 1$.

For convenience, we now define four other matrices $\boldsymbol{J}_i$, Fig. 3.5. It can be shown [60] that points inside the shaded region $\mathscr{R}$, as well as along the lines connecting $\boldsymbol{J}_i$ and $\boldsymbol{A}_i$, can be constructed via a lamination that converges to zero energy as the laminate rank tends to infinity. The proof, by construction, involves successive laminations between pairs $\{\boldsymbol{A}_i, \boldsymbol{J}_i\}$. An arbitrary matrix $\boldsymbol{F}$, interior to $\mathscr{R}$, is decomposed into a laminate of the points $\boldsymbol{F}_1$ and

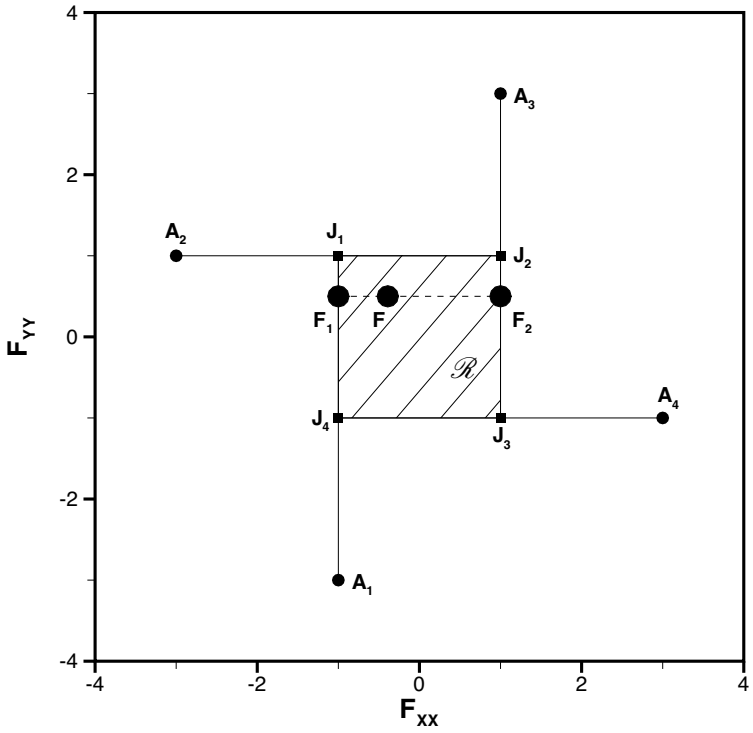

Figure 3.5: Diagram of the four-well problem illustrating relaxed region $\mathscr{R}$ (cross-hatched), wells A_i, auxiliary matrices J_i, and the matrices $\{F, F_1, F_2\}$ from the text.

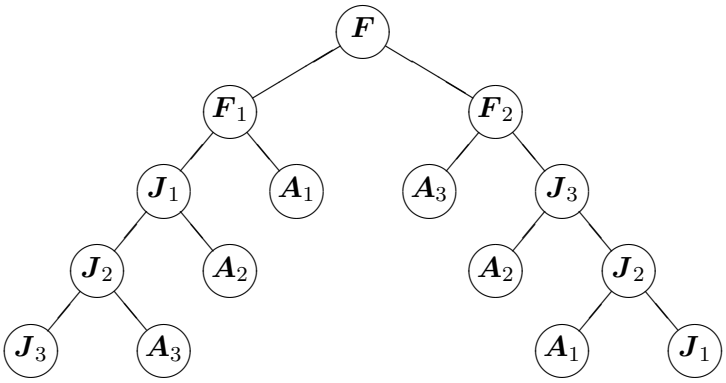

Figure 3.6: Tree representation of an intermediate laminate in the analytic solution to the four-well problem. Refer to Fig. 3.5 for the definitions of $\{\boldsymbol{A}_i, \boldsymbol{J}_i, \boldsymbol{F}, \boldsymbol{F}_i\}$.

$\boldsymbol{F}_2$ on the boundary. Each of these boundary points can then be expressed as a laminate involving pairs of $\boldsymbol{A}_i$ and $\boldsymbol{J}_i$. One laminate in this infinite sequence is shown in Fig. 3.6. The next laminate in the sequence for the left half of this tree is constructed by expressing $\boldsymbol{J}_3$ as

$$\boldsymbol{J}_3 = \frac{1}{2}(\boldsymbol{A}_4 + \boldsymbol{J}_4) \tag{3.11}$$

after which the pattern repeats. Observe that, because the leaf deformation gradients $\boldsymbol{A}_i$ as in (3.11) are at zero energy, the energy is reduced by a factor of two with each successive lamination after the initial lamination on the boundary (e.g., starting with leaf $\boldsymbol{J}_1$ on the left of Fig. 3.6).

Recall that the lamination algorithm requires an initial value of $\{\lambda, \boldsymbol{a}, \boldsymbol{N}\}$ for each new branch, given the variants of the two leaves. As the region of interest includes the zero matrix and the 'transformation matrices' have negative determinants, it is not clear that one should apply the twinning equation [17]

$$\boldsymbol{Q}\boldsymbol{A}_i - \boldsymbol{A}_j = \boldsymbol{a} \otimes \boldsymbol{N} \tag{3.12}$$

where $\boldsymbol{Q} \in SO(3)$, $\boldsymbol{a}, \boldsymbol{N} \in \mathbb{R}^3$, and $|\boldsymbol{N}| = 1$, as is done in Chapter 2 with Cu-Al-Ni. However, laminations between pairs $\{\boldsymbol{A}_i, \boldsymbol{J}_i\}$ play a central role in the analytic solution constructed above. Each pair is rank-one connected, and can be expressed using (3.4) in terms of $\boldsymbol{a}$ and $\boldsymbol{N}$ to yield

$$\begin{aligned}
\{\boldsymbol{J}_1, \boldsymbol{A}_1\} \quad &\Rightarrow \quad \boldsymbol{a}_1 = (0,4), \quad \boldsymbol{N}_1 = (0,1) \\
\{\boldsymbol{J}_2, \boldsymbol{A}_2\} \quad &\Rightarrow \quad \boldsymbol{a}_2 = (4,0), \quad \boldsymbol{N}_2 = (1,0) \\
\{\boldsymbol{J}_3, \boldsymbol{A}_3\} \quad &\Rightarrow \quad \boldsymbol{a}_3 = (0,4), \quad \boldsymbol{N}_3 = (0,-1) \\
\{\boldsymbol{J}_4, \boldsymbol{A}_4\} \quad &\Rightarrow \quad \boldsymbol{a}_4 = (4,0), \quad \boldsymbol{N}_4 = (-1,0).
\end{aligned} \tag{3.13}$$

Unfortunately, these values are for laminations between $\boldsymbol{J}$ and $\boldsymbol{A}$. Furthermore, recall that the deformation gradient at the leaves need not coincide with $\boldsymbol{A}_i$; the leaf variant only indicates which $\boldsymbol{A}_i$ is used in the energy functional. It is thus not clear which of these four pairs of values are applicable for a given pair of variants, as required by the lamination algorithm. For robustness, the minimum energy solution is selected using each of these four cases.

To preclude infinite branching in this numerical test, the algorithm was modified to require that the energy reduction obtained by branching be larger than a numerical tolerance, chosen here to be 0.001 (note that at the origin the unrelaxed energy attains a value of 10.). If this tolerance is much smaller the algorithm develops extremely high rank laminates and the computational effort quickly becomes unreasonable.

The lamination was computed on a grid of points in the F_{xx}–F_{yy} plane, Fig. 3.7. As implemented, the algorithm is not able to obtain satisfactory results near the origin, although the solution elsewhere is encouraging.

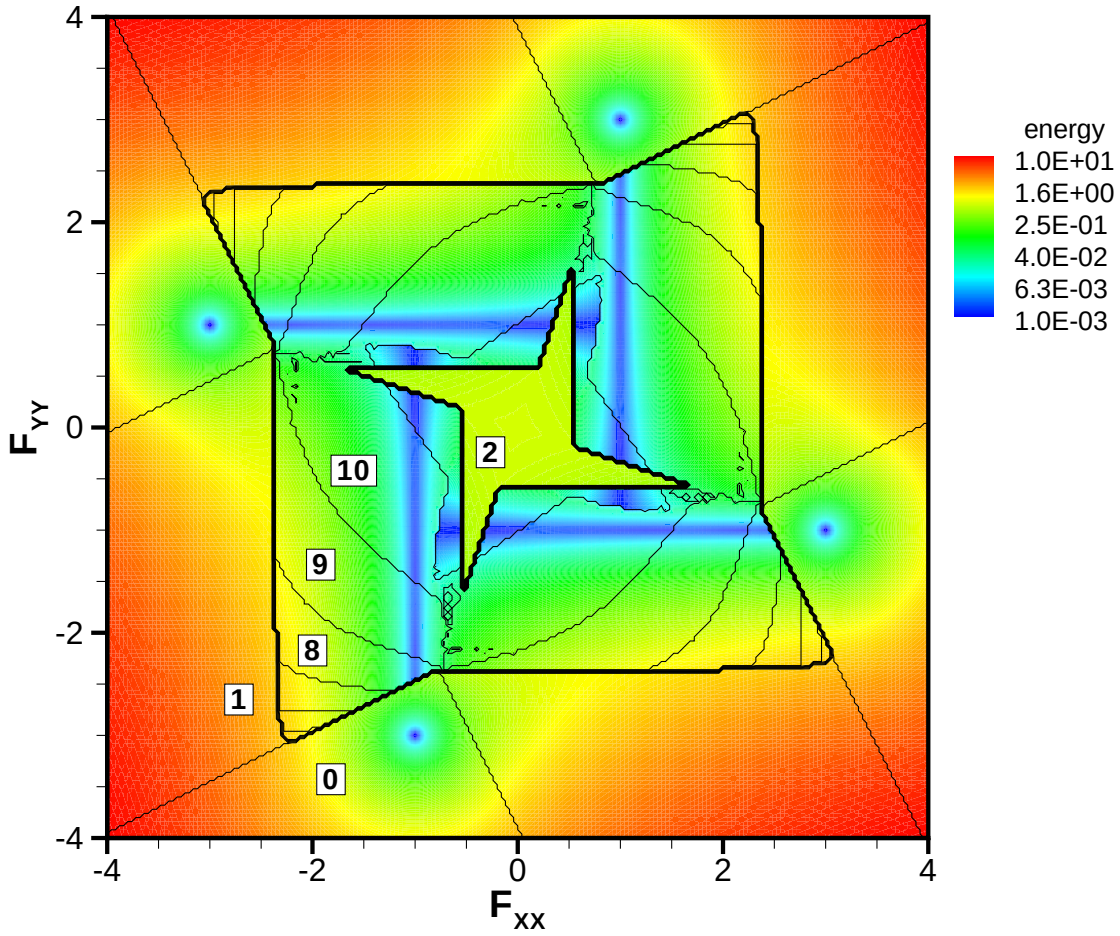

Figure 3.7: Initial relaxation for the four-well model, computed directly at each point. The lines are contours of laminate rank, with several values indicated, while the color represents energy on a logarithmic scale.

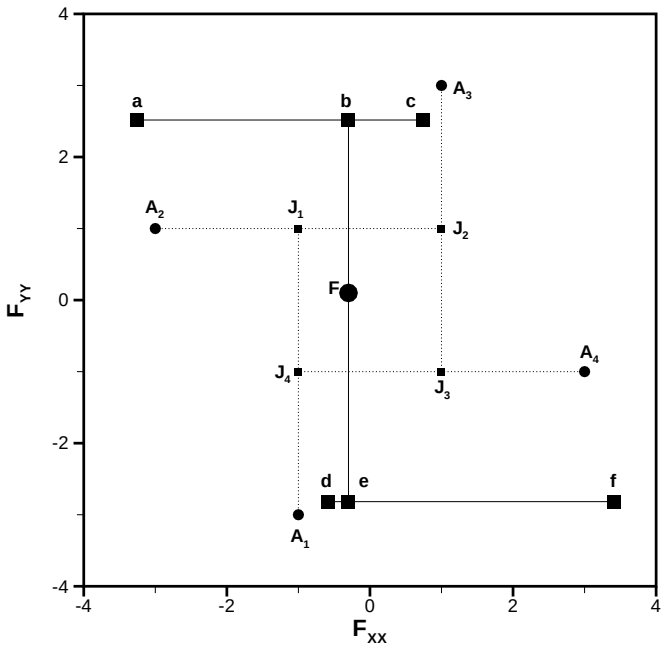

Figure 3.8: Diagram of solution obtained at $\boldsymbol{F} = \mathrm{diag}(-0.3, 0.1)$ for the four-well problem.

A schematic of the laminate obtained at $\boldsymbol{F} = \mathrm{diag}(-0.3, 0.1)$ in this central region is plotted in Fig. 3.8. In these diagrams, laminations are represented by points joined by horizontal or vertical lines. Leaves are associated with unconnected line endpoints, an intersection represents an interior node, and volume fractions are related to segment length. For the laminate in Fig. 3.8, the root is $\boldsymbol{F}$, with children $\boldsymbol{b}$ and $\boldsymbol{e}$. The volume fraction for $\boldsymbol{c}$ with respect to its parent $\boldsymbol{b}$ is $\lambda_c = \overline{\boldsymbol{ab}}/\overline{\boldsymbol{ac}}$, while the total volume fraction is $\nu_c = \lambda_c \overline{\boldsymbol{Fe}}/\overline{\boldsymbol{be}}$, where, e.g., $\overline{\boldsymbol{ab}}$ indicates the length of the line segment between $\boldsymbol{a}$ and $\boldsymbol{b}$.

Near the origin, the analytic solution described above would construct a microstructure that has a very high energy for the initial two levels shown in Fig. 3.6. However, the numerical algorithm constructs solutions via recursive branching of the existing laminate, minimizing the energy after each branching, and terminating when no further rank-one branch reduces the total energy. The algorithm is thus unable to construct laminates in

which a rank-one branch leads to an increase in energy, but further branching would result in an energy reduction. Essentially, this represents an energy barrier for branching.

Given the solution in Fig. 3.8, evidently there is no rank-one branching of the leaves $\{\boldsymbol{a}, \boldsymbol{c}, \boldsymbol{d}, \boldsymbol{f}\}$ that reduces the total energy. This is readily apparent, given the quadratic energy functional and location of the leaves in the figure, for a fixed location of the leaves (discounting the global optimization of $\{\lambda_i, \boldsymbol{a}_i, \boldsymbol{N}_i\}$), but is not obvious in the general case. This energy barrier also explains the failure of the algorithm to laminate close to the wells themselves, even along the lines $\overline{\boldsymbol{A}_i\boldsymbol{J}_i}$, due to the relatively small unrelaxed energy close to the well.

It is envisioned that the ultimate use of this algorithm is to incrementally deform a material from a known initial microstructure. The evolution of the microstructure along such a deformation path should assist the algorithm in overcoming the energy barrier discussed. The calculation in Fig. 3.7 was thus repeated in this fashion by computing the result at each point $\boldsymbol{X}$ in the figure via the arbitrary linear deformation path

$$\boldsymbol{F}(t) = (1-t)\boldsymbol{A}^* + t\boldsymbol{X}, \quad t \in [0,\, 1] \tag{3.14}$$

starting from the location $\boldsymbol{A}^*$ of the nearest well (where the microstructure is known to consist of this single variant).

The incremental results, Fig. 3.9, indicate that the algorithm was able to obtain a fully relaxed result, within the numerical tolerance discussed above, along the lines connecting each pair $\{\boldsymbol{A}_i, \boldsymbol{J}_i\}$, discounting the small regions near the wells themselves. In the interior of $\mathscr{R}$ the algorithm is able to relax the energy to 1.5% or less of the initial value, but does not obtain the exact result.

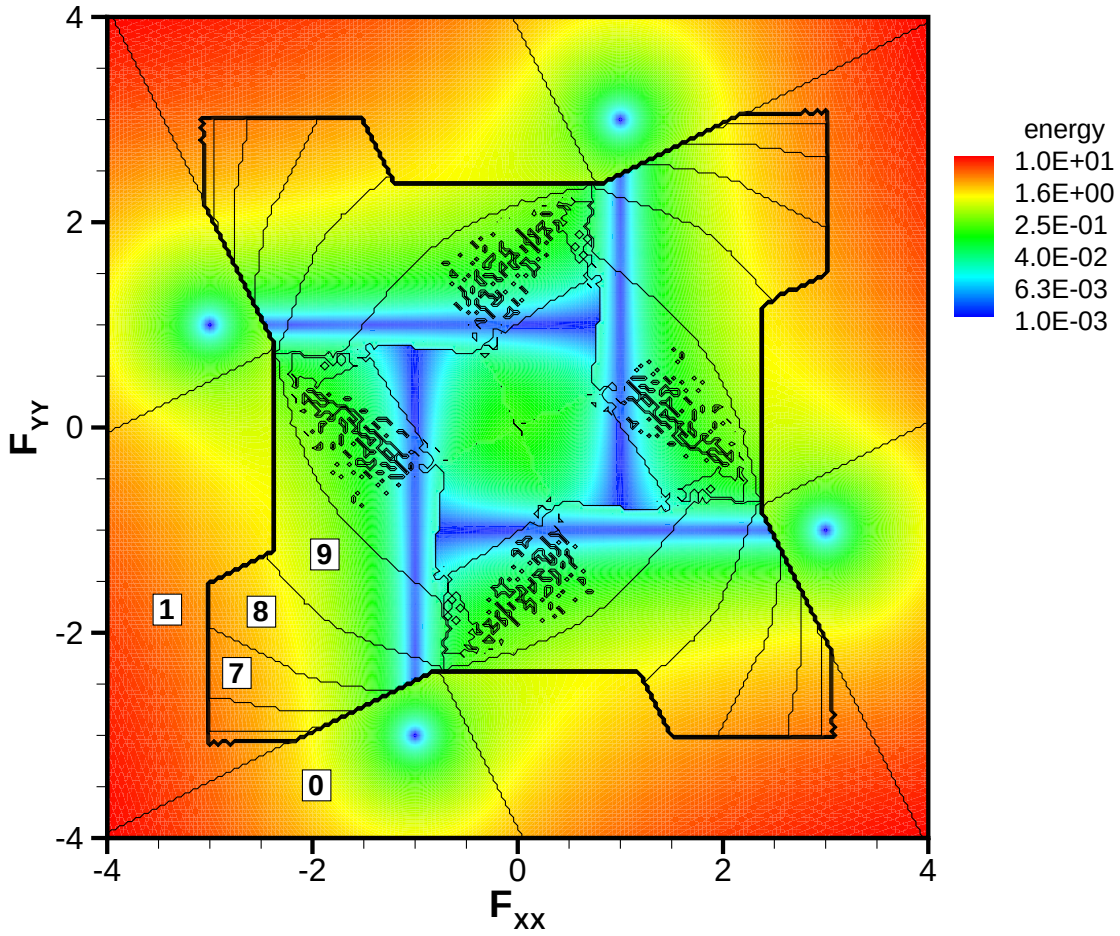

Figure 3.9: Laminate energy for the four-well model obtained via an incremental deformation path. The lines are contours of laminate rank, with several values indicated. Note that the energy scale is logarithmic.

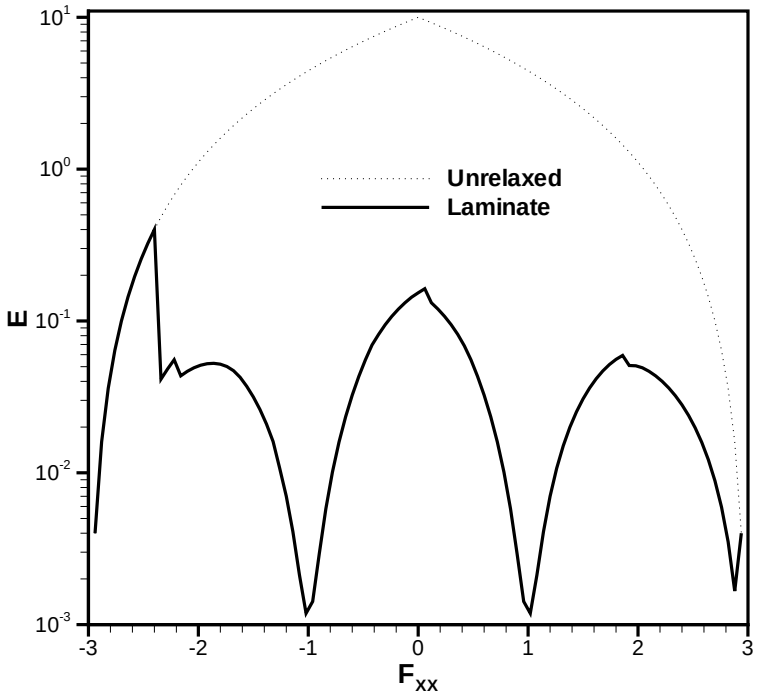

Figure 3.10: Laminate energy obtained for the four-well model for a deformation path from $\boldsymbol{A}_2$ to $\boldsymbol{A}_4$. Note that the energy scale is logarithmic.

For further illustration, results were obtained for the deformation path

$$\boldsymbol{F}(t) = (1-t)\boldsymbol{A}_2 + t\boldsymbol{A}_4, \quad t \in [0,\, 1] \tag{3.15}$$

between two of the wells, Fig. 3.10. Except for a few isolated points, the laminate is rank-eleven in the interval $\boldsymbol{F}_{xx} = [-2.4, 3]$ where lamination is obtained. Unlike the results in Fig. 3.9, the deformation is incremented from the left of the figure continuously to the right, with the lamination starting from the microstructure obtained in the previous step. Thus, although the algorithm cannot overcome the energy barrier for $\boldsymbol{F}_{xx} < -2.4$, the laminate that is eventually created is energetically favorable up to $\boldsymbol{F}_{xx} = 3$.

To observe the difficulties encountered close to the origin, we shall examine the microstructure obtained at $\boldsymbol{F} = \mathrm{diag}(-0.3,\, 0.1)$ under the deformation (3.15). The analytic

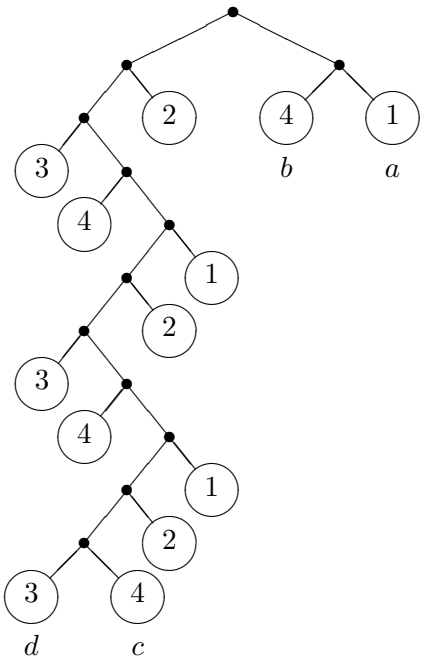

Figure 3.11: Graph of the rank-eleven solution obtained at $\boldsymbol{F} = \mathrm{diag}(-0.3,\ 0.1)$ for a deformation path from well $\boldsymbol{A}_2$ to well $\boldsymbol{A}_4$. The variant number (indicating $\boldsymbol{A}_1$, $\boldsymbol{A}_2$, $\boldsymbol{A}_3$, or $\boldsymbol{A}_4$) is given for each of the leaves.

solution for this point is a zero energy balanced tree, as shown in Fig. 3.6, but of infinite extent. The numerical results, Fig. 3.11, appear significantly different. However, the entire left half of this tree can be made to resemble the left half of analytic solution in Fig. 3.6 by appropriate switching of left and right-hand leaves, corresponding to changes in the sign of $\boldsymbol{N}$. This solution is further plotted on the F_{xx}–F_{yy} plane, Fig. 3.12. Examining the details of the leaves $\boldsymbol{a}$ and $\boldsymbol{b}$ from Fig. 3.11 indicates that they are nearly identical to nodes $\boldsymbol{d}$ and $\boldsymbol{f}$ shown in Fig. 3.8, and furthermore account for 90% of the total energy. The other terminal leaves, $\boldsymbol{c}$ and $\boldsymbol{d}$, have a very low volume fraction and do not contribute significantly to the energy. Although the chosen incremental deformation path significantly reduced the total energy, it was only successful in overcoming the energy barrier for one of the rank-two leaves in Fig. 3.11.

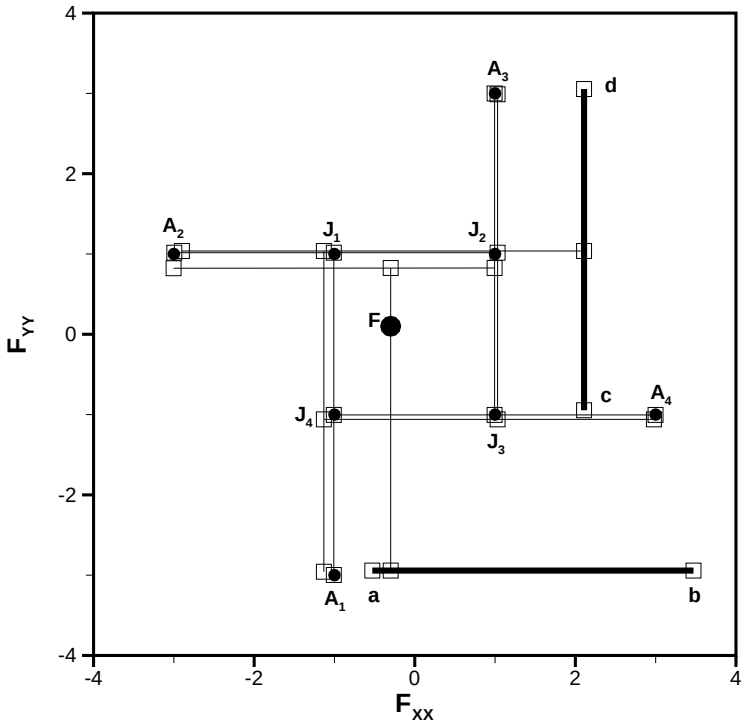

Figure 3.12: Diagram of solution obtained at $\boldsymbol{F} = \mathrm{diag}(-0.3, 0.1)$ for the four-well problem using an incremental deformation path.

3.4 Nematic elastomer model

The next example is a model for nematic elastomers first proposed by Bladon et al. [23, 84], and studied extensively by DeSimone and Dolzmann [32, 35, 37], who showed it qualitatively reproduced experimental results [88].

The energy model of Bladon et al. can be written as [37]

$$W(\boldsymbol{F}) = \beta^2 \left(|\boldsymbol{F}|^2 - \frac{\beta^6 - 1}{\beta^6} |\boldsymbol{F}^T \boldsymbol{d}|^2 \right) - 3 \tag{3.16}$$

where $\boldsymbol{d}$, $|\boldsymbol{d}| = 1$, is the director, a characteristic direction in the elastomer, β is a constant, and the deformation gradient $\boldsymbol{F} \in \mathbb{R}^{3\times 3}$ is restricted such that $\det(\boldsymbol{F}) = 1$. As $\boldsymbol{d}$ is an independent variable, (3.16) can be minimized first with respect to the director. This energy can be expressed using the eigenvalues λ_i^2 of $\boldsymbol{C} = \boldsymbol{F}^T \boldsymbol{F}$, ordered such that $\lambda_1 < \lambda_2 < \lambda_3$, with the restriction that $\lambda_1 \lambda_2 \lambda_3 = 1$. This form allows for the trivial minimization of the term involving $\boldsymbol{d}$, resulting in the energy functional to be considered here

$$W(\boldsymbol{F}) = \beta^2 \lambda_1^2 + \beta^2 \lambda_2^2 + \frac{\lambda_3^2}{\beta^4} - 3. \tag{3.17}$$

The energy (3.17) represents a continuum of $SO(3)$ invariant states, rather than individual energy wells as previously considered, and essentially can form laminations with reoriented versions of itself. DeSimone and Dolzmann have obtained the quasiconvexifica-

tion of this energy [35]

$$W^{qc}(\boldsymbol{F}) = \begin{cases} 0, & \lambda_3 \leq \beta^2, \\ \frac{2}{\beta\lambda_1} + \beta^2\lambda_1^2 - 3, & \lambda_1\lambda_3^2 \leq \beta^3, \\ W(\boldsymbol{F}), & \lambda_1\lambda_3^2 \geq \beta^3, \end{cases} \tag{3.18}$$

where the three solutions represent a liquid phase, intermediate phase, and solid phase, respectively.

Following the construction of W^{qc}, we shall consider as initial guesses those laminations in which one of the three principal stretches λ_i remains constant. This results [35] in an initial guess $\lambda = 1/2$, with $\boldsymbol{a}$ and $\boldsymbol{N}$ chosen to be the eigenvectors perpendicular to the lamination direction. Thus, e.g., for laminations along lines in which λ_1 is constant, the initial guess is taken to be $\boldsymbol{a} = \boldsymbol{v}_2$ and $\boldsymbol{N} = \boldsymbol{v}_3$, where $\boldsymbol{v}_i$ is the eigenvector corresponding to λ_i^2. The lamination direction is determined for each branching via energy minimization.

Applying the lamination algorithm, using $\beta^2 = 1.26$, yields the exact solution, Fig. 3.13 (compare with Fig. 3 in [35] with $\beta^2 = r^{1/3}$).

3.5 Polycarbonate model

The final verification test involves a constitutive model for polycarbonate that is similar to the nematic elastomer model just discussed. Of particular interest is the nearly perfectly-plastic behavior of the material characterized by the appearance of nanoscale laminations between elastic and plastic 'phases' [42]. Here we focus on algorithm verification rather than the details of the development of the model or its comparison with experiment. For further discussion regarding these topics see [41].

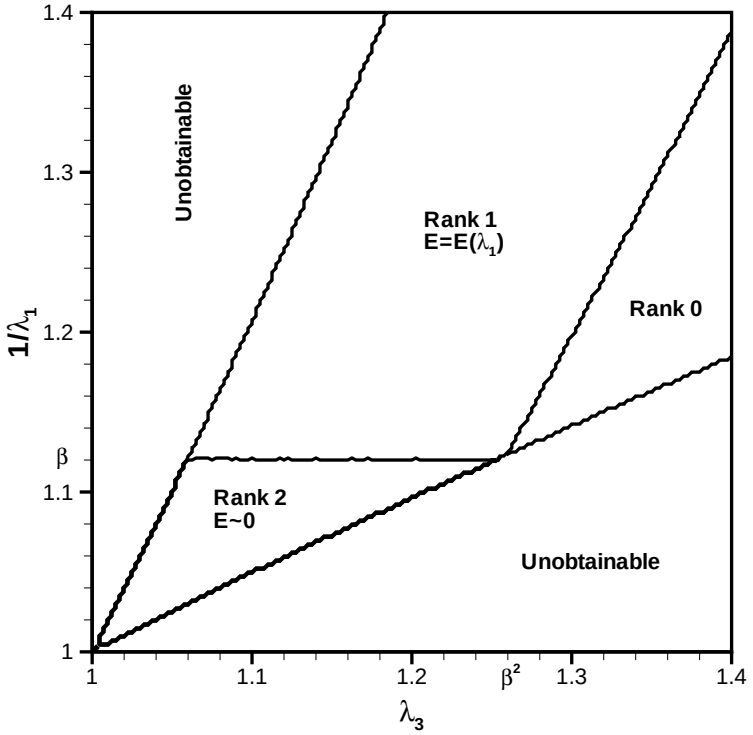

Figure 3.13: Lamination result for the nematic elastomer model, corresponding closely to the exact solution.

The model involves two energy wells

$$W_1 = \lambda_1^2 + \lambda_2^2 + \lambda_3^2 - 3 \tag{3.19}$$

$$W_2 = \eta^2\lambda_1^2 + \lambda_2^2 + \left(\frac{\lambda_3}{\eta}\right)^2 + dU - 3 \tag{3.20}$$

where again the λ_i^2 are the eigenvalues of $\boldsymbol{C} = \boldsymbol{F}^T\boldsymbol{F}$, ordered such that $\lambda_3 \geq \lambda_2 \geq \lambda_1 \geq 0$, and where the energy has been normalized by $\mu/2$, with μ the shear modulus. As in the DeSimone-Dolzmann model discussed beforehand, we are presently restricting this model to isochoric deformations, i.e., $\lambda_1\lambda_2\lambda_3 = 1$. The elastic response is embodied in W_1, which is essentially just (3.1). The second well is similar to (3.17) in that it consists of an $SO(3)$ continuum of states. However, this well can form laminations with the first well in addition to the 'self-laminations' encountered in the nematic elastomer model. W_2 is at a higher energy than W_1 in the undeformed state, but becomes preferred at high shear. This well thus represents plasticity with the amount of plastic yield and plastic work related to η and dU respectively.

The relaxation of this energy corresponding to the polyconvex envelope has been obtained by Fortunelli et al. [41] using a parabolic approximation of the energy. As the solution is symmetric about $\lambda_2 = 1$ in the $(1/\lambda_1,\, \lambda_3)$ plane, we will state the result for $\lambda_2 \leq 1$

$$W^{pc}(\boldsymbol{F}) = \begin{cases} W_1, & \alpha < \alpha_1, \\ W_a, & \alpha_1 \leq \alpha \leq \alpha_2 \text{ and } \lambda_2^{crit} \leq \lambda_2 \leq 1, \\ W_b, & \alpha_1 \leq \alpha \leq \alpha_2,\ \lambda_2 \leq \lambda_2^{crit} \text{ and } \lambda_3 \leq \lambda_3^{crit}, \\ W_c, & \lambda_3 > \lambda_3^{crit} \text{ and } \frac{1}{\lambda_1} \leq \sqrt{\eta\lambda_3}, \\ W_2, & \text{otherwise}, \end{cases} \tag{3.21}$$

where:

$$W_a = \lambda_2^2 + \frac{2}{\lambda_2} + \frac{dU}{\gamma}\sqrt{\lambda_2}\left(\alpha - \frac{dU}{4\gamma}\sqrt{\lambda_2}\right) - 3, \tag{3.22}$$

$$W_b = W_b(\lambda_3) = W_a|_{\lambda_2=\lambda_2^{crit}}, \tag{3.23}$$

$$W_c = \left(\frac{\lambda_3}{\eta}\right)^2 + 2\frac{\eta}{\lambda_3} + dU - 3, \tag{3.24}$$

$$\alpha = \lambda_3 - \lambda_1, \tag{3.25}$$

$$\alpha_1 = \frac{dU}{2\gamma}\sqrt{\lambda_2}, \tag{3.26}$$

$$\alpha_2 = \frac{\gamma}{\sqrt{\lambda_2}} + \frac{dU}{2\gamma}\sqrt{\lambda_2}, \tag{3.27}$$

$$\gamma = \eta - \frac{1}{\eta}. \tag{3.28}$$

The value for λ_2^{crit} is obtained at each value of λ_3 by solving

$$\left.\frac{dW_a}{d\lambda_2}\right|_{\lambda_3} = 0 \tag{3.29}$$

using the relation $\lambda_1\lambda_2\lambda_3 = 1$ to eliminate λ_1. We also define λ_3^{crit} as the intersection between $\alpha = \alpha_2$ and $\lambda_2^{crit}(\lambda_3)$, and $\lambda_1^{crit} = 1/\lambda_2^{crit}\lambda_3^{crit}$. The different regions in the relaxed energy can be characterized as follows: the energy W_a arises through rank-one laminations between W_1 and W_2, W_b is a rank-two laminate between W_1 and a laminate of W_2, and W_c is a self-lamination of W_2.

The lamination algorithm again requires initial guesses for $\{\lambda, \boldsymbol{a}, \boldsymbol{N}\}$. For laminations involving W_2 laminating with itself the initial guess is identical to that given in §3.4. For laminations between the two wells we refer to the construction of the solution [41]. We again attempt laminations such that each of the three eigenvalues λ_i are constant. The eigenvalue λ_i under consideration will be denoted by ζ_2, the remaining two eigenvalues ζ_1 and ζ_3 are

ordered such that $\zeta_1 \leq \zeta_3$. As derived by Fortunelli et al., the appropriate lamination values are

$$\boldsymbol{N} = -f_1 \boldsymbol{v}_1 + f_2 \boldsymbol{v}_2 \tag{3.30}$$

$$\boldsymbol{a} = |A| \left(f_1 \boldsymbol{v}_1 + f_2 \boldsymbol{v}_2 \right) \tag{3.31}$$

$$\lambda = \frac{4 \left(\eta - 1 \right) \alpha \sqrt{\zeta_2} - dU \zeta_2}{8 \left(\eta - 1 \right)^2} \tag{3.32}$$

where $\boldsymbol{v}_i$ is the eigenvector corresponding to ζ_i, with the values α, f_1, f_2, and $|A|$ given by

$$\alpha = \zeta_3 - \zeta_1 \tag{3.33}$$

$$f_1 = \sqrt{\frac{\zeta_1}{\zeta_1 + \zeta_3}} \tag{3.34}$$

$$f_2 = \sqrt{\frac{\zeta_3}{\zeta_1 + \zeta_3}} \tag{3.35}$$

$$|A| = 2 \left(\eta - 1 \right) \zeta_1 \zeta_3. \tag{3.36}$$

With the above expressions for the unrelaxed energy and initial guesses it is straightforward to apply the lamination algorithm. For the following calculations, we take $\eta = 1.06$, and $dU = 0.006$. The resulting energy 'phase' diagram is shown in Fig. 3.14. In this diagram W_a is the rank-one region along the diagonal, defined by diagonal lines corresponding to λ_2^{crit} in two directions and α_1 and α_2 in the remaining directions. The rank-two region to either side is W_b, further defined by the vertical line λ_3^{crit}. Finally, W_c is the remaining rank-one area bounded by the given parabola and λ_3^{crit}.

As indicated, the material of interest exhibits very soft behavior. Examining the cauchy mises stress response, Fig. 3.15, clearly indicates the areas of constant stress corresponding to W_b in (3.21). The central region identified with energy W_a is also at a constant stress

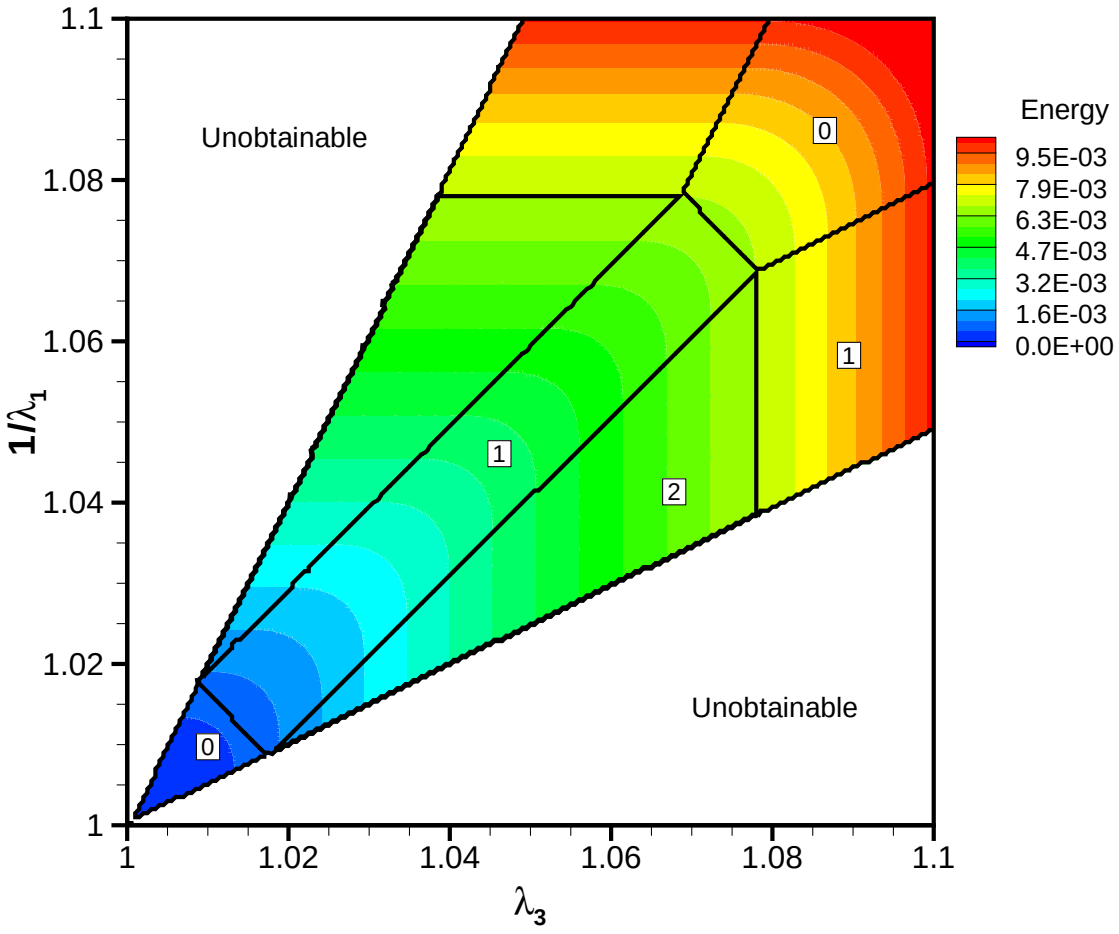

Figure 3.14: Phase diagram of polycarbonate model obtained via lamination. The colors indicate total energy, while the lines demarcate regions of constant laminate rank as indicated. The rank-two regions are at constant mises stress. Note the regions that are unobtainable due to the isochoric constraint.

along lines parallel to pure shear, $\lambda_2 = 1$, with a yield point defined by α_1, and continued hardening after the curve given by α_2.

Closer examination of the energy along the diagonal line $\lambda_2 = 1$ displays a constant slope tangent to both energy wells, Fig. 3.16. The figure also gives an indication of the robust performance of the algorithm in obtaining the relaxed solution along this entire tangent line.

Finally, plotting the stress-strain response for both shear and tension, Fig. 3.17, gives an indication of the performance of the model in predicting experimental results. Note that this figure was obtained from Fig. 3.14, with tension corresponding to the parabola

$$\lambda_1 = \lambda_2 = \frac{1}{\sqrt{\lambda_3}}. \tag{3.37}$$

This model, still under development, obtains a region of perfectly plastic behavior followed by hardening. Planned extensions to the model, including volumetric and hydrostatic pressure effects and hysteresis, are necessary to compare to experimental data [22]. Initial results of the enhanced model are promising. Notwithstanding the current physical applicability, the lamination algorithm obtained the correct analytic result.

3.6 Conclusions

In this chapter we have performed verification tests of the lamination algorithm detailed in Chapter 2 via the solution of several problems with analytic solutions.

The anti-plane shear problem was not especially difficult because the transformation stretches were pairwise rank-one connected (without the need for a rotation). Nevertheless, the method did obtain the exact result, providing an initial verification of basic correctness.

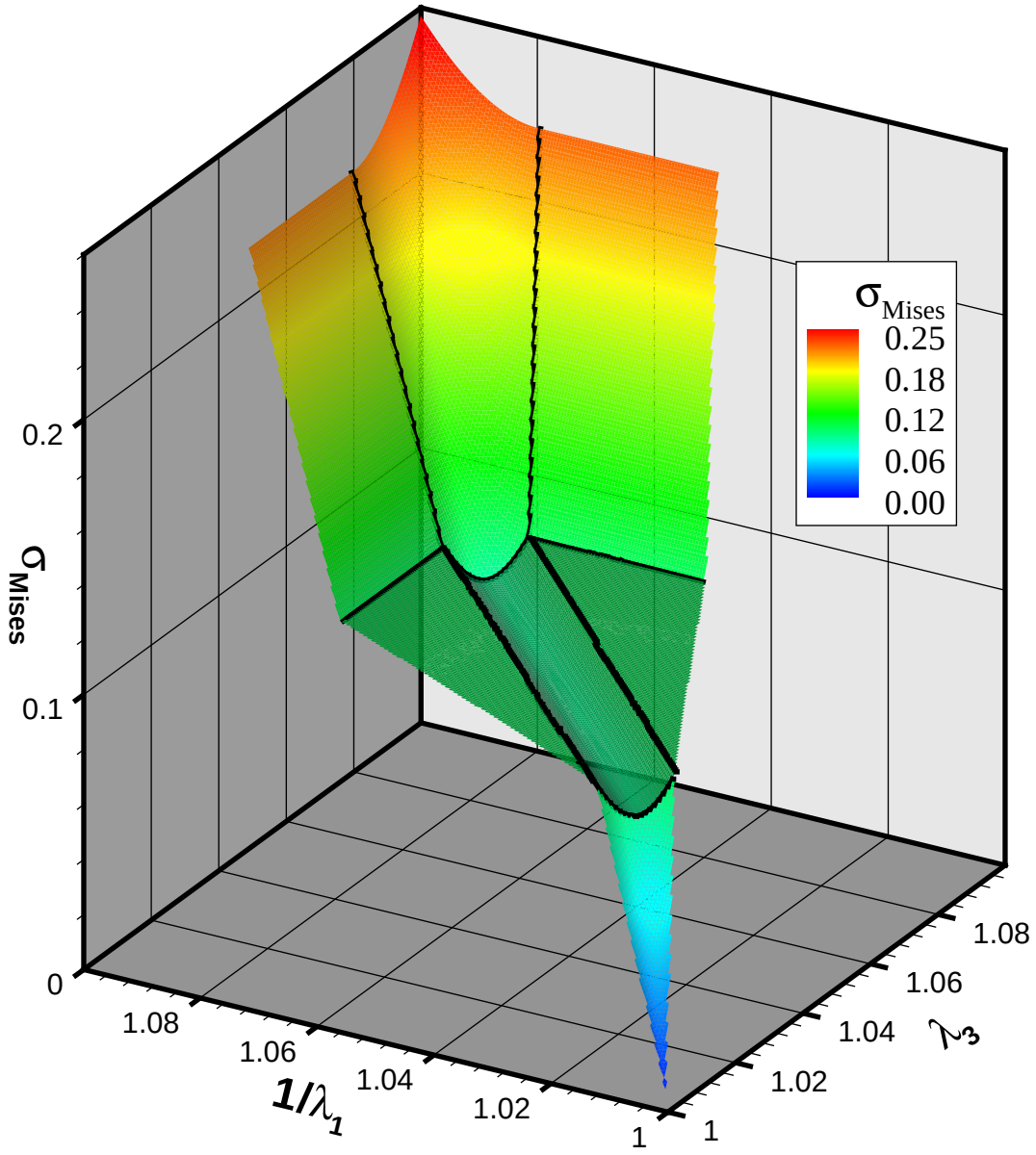

Figure 3.15: Mises stress response of relaxed polycarbonate model as a function of $1/\lambda_1$ and λ_3. Notice the flat regions corresponding to energy W_b in (3.21).

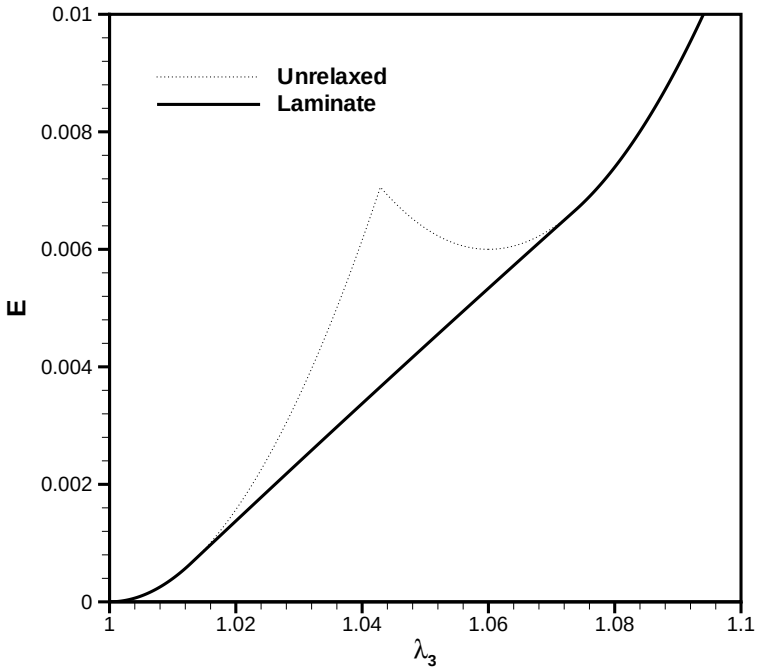

Figure 3.16: Lamination of polycarbonate model in pure shear (along line $\lambda_2 = 1$) compared with the unrelaxed result.

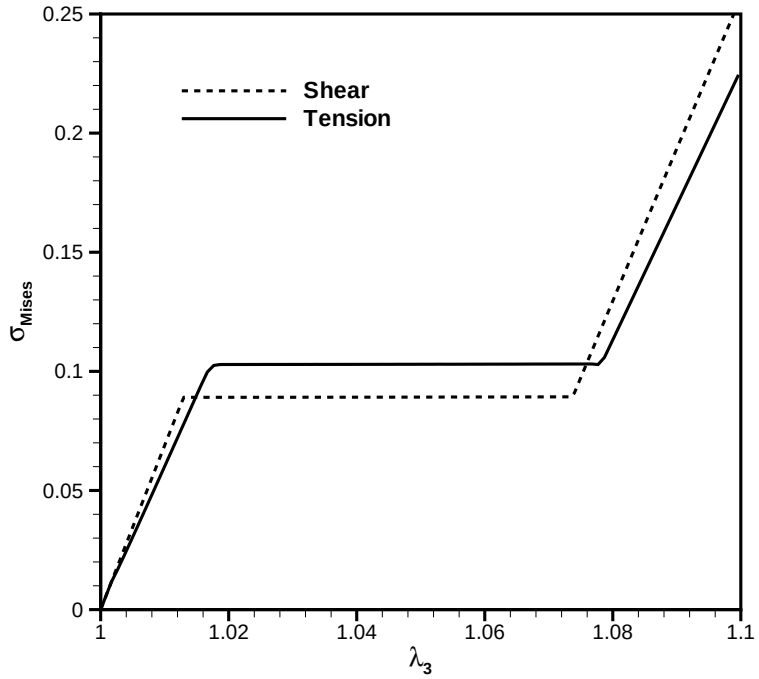

Figure 3.17: Polycarbonate model stress-strain response in pure shear and tension.

The four-well problem, without rank-one connected wells, proved to be more challenging. The exact solution prescribes zero energy laminates in the region $\mathscr{R}$ and along the line segments $\overline{\boldsymbol{A}_i\boldsymbol{J}_i}$ in Fig. 3.5. While the algorithm is able to obtain the exact result along portions of these line segments, computing the lamination afresh at each point in this plane results in an energy reduction of less than 10% near the origin. This difficulty can be attributed to an 'algorithmic' energy barrier to branching inherent in the method chosen for microstructural evolution: that each rank-one branching must result in an energy reduction (see §2.3.2). The introduction of an incremental deformation path in the spirit of a physical application allows for the development of high rank laminates in the central region. While these microstructures are still limited by the energy barrier from completely relaxing the energy, they are able to reduce the energy in $\mathscr{R}$ by more than 98.5%. While this is not the optimal result obtained by Dolzmann and Walkington [36, 39] and Aranda and Pedregal [5], the present work utilizes a more practical deterministic optimization routine. While the aforementioned energy barrier was not designed to mimic a specific physical process, it is reflective of the metastability and activation energies present in physical processes. With this realization, this feature of the sequential lamination algorithm is not undesirable.

The nematic elastomer model was more unusual in that it consisted of the relaxation of one nonconvex 'well' formulated in terms of the principal stretches, possessing an $SO(3)$ continuum of minima. Given the relatively obvious initial guesses for the plane normal and shear direction, the algorithm attained the exact result.

The final verification test concerned a constitutive relation, still under development, for polycarbonate materials. This two well model has one 'elastic' well at the origin with a second well that is activated in shear. The second well, similar to the nematic elastomer model, is again nonconvex. By attempting laminations both between the elastic and plastic

wells in addition to the relaxation of the second well itself, the model is able to obtain a perfectly plastic response followed by hardening reminiscent of the polycarbonate material of interest.

Given reasonable expressions for $\{\boldsymbol{a}, \boldsymbol{N}\}$ with which to initiate the laminate optimization (obtaining λ from a line search if necessary) the calculations produced good results, as discussed. For the anti-plane shear problem these values were obvious. Reasonable values were also obtained for the four-well and nematic elastomer calculations with little difficulty, but with knowledge of the exact solution. The relaxation of the polycarbonate model was quite sensitive to the initial guess, but it is unclear if one could obtain useful initial values without access to the relaxation. This then identifies one drawback to the general applicability of the present approach. However, in applications in which initial guesses are readily available, such as anti-plane shear, the nematic elastomer model, and martensites, this difficulty is not a consideration.

Chapter 4

Experimental validation: Cu-Al-Ni tension test

4.1 Introduction

Experimental validation is an important step in the development of any practical material model. The lamination algorithm presented in the foregoing provides both an explicit construction of the material microstructure and the macroscopic behavior. It is thus advantageous to compare the numerical model to experimental results that provide similar data. Fortunately, Shield [74] performed tension test experiments at several orientations on the same Cu-Al-Ni alloy studied in §2.4, and obtained both stress-strain curves and images of the microstructure present on the specimen surface.

Various constitutive models that are relevant to this experiment have been developed. For instance, Gao and Brinson [43] have developed a simplification of the 'Multivariant' model, a small strain approach based on the evolution of the volume fractions of variant 'inclusions' in an austenite matrix, that includes hysteresis and temperature effects. With proper fitting of the parameters, the model provides reasonable predictions of the transformation stress and hysteresis. The model of Govindjee and coworkers [45–47] is based on a lower-bound of the quasiconvexification of the energy. Reminiscent of plasticity models,

a dissipation argument is used to derive variant volume fraction evolution equations that are integrated using a generalization of the 'trial elastic-step' method popular in plasticity. While the approach ignores large deformations and is limited to isotropic moduli, the comparison with Shield's experiment is surprisingly good. As a final example, Stupkiewicz and Petryk [78] present a model based on sequential lamination and the linear theory of martensites [16]. The algorithm utilizes a local criterion for transformation, with the requirement that the thermodynamic driving force exceed a critical value for transformation to occur, producing hysteresis. With the assumption of an austenite–twinned martensite microstructure, the authors obtain the correct trends for the transformation stresses and hysteresis. While the above theories generally produce respectable results, they are all limited to small deformations, and are not as widely applicable as the present algorithm.

This chapter will first discuss the Schmid law used in the design of the experiment, and then briefly review the experimental results. The lamination algorithm as described in Chapter 2 will then be used, both at a single point and via a finite element calculation, to model the experiment. Based on these results, the algorithm will be extended and the calculation repeated.

4.2 Schmid law material model

Shield used an approximate model similar to the resolved shear stress (RSS) or Schmid law, but based on the work of transformation, to predict the transformation stress and the participating variants and their geometry. Zhang et al. [87] have presented a comparison between a similar transformation work formulation and the RSS approach, providing a stereographic projection indicating the most favorable Type I and Type II twins for each model, and concluded that the work model more accurately predicts their experimental

results.

Shield's derivation [74] begins with an approximation for the work of transformation

$$W_i = \text{trace}((\boldsymbol{U}_i - I)\boldsymbol{\sigma}) \tag{4.1}$$

where $\boldsymbol{\sigma}$ is the applied stress and $\boldsymbol{U}_i$ is the transformation stretch of variant i. This neither accounts for surface or nucleation energy, nor does it account for elastic effects (the 'constrained' model [11, 12]). Although the specimen is to be deformed uniaxially, this does not imply that the state of stress remains purely axial. In this approximation, however, the stress is assumed to be

$$\sigma = s\boldsymbol{e} \otimes \boldsymbol{e} \tag{4.2}$$

where s is the magnitude and $\boldsymbol{e}$ is the axial direction. As shown in §1.1, Cu-Al-Ni cannot form an interface between austenite and individual martensite phases. This requires that $\boldsymbol{U}_i$ in (4.1) be the average deformation gradient of one of the 96 twinned-martensite laminates (8 solutions for each of 12 compatible martensite variant pairs) that are compatible with austenite in the constrained model. The deformation can thus be expressed as

$$\boldsymbol{U}_i = \boldsymbol{I} + \boldsymbol{b}_i \otimes \boldsymbol{m}_i \tag{4.3}$$

for the habit-plane solution i. The work required thus becomes

$$W_i = s(\boldsymbol{b}_i \cdot \boldsymbol{e})(\boldsymbol{m} \cdot \boldsymbol{e}). \tag{4.4}$$

Solving for s and minimizing yields

$$s_{cr} = \min_{i \in habit-plane} \frac{W_{cr}}{(\boldsymbol{b}_i \cdot \boldsymbol{e})(\boldsymbol{m}_i \cdot \boldsymbol{e})} \tag{4.5}$$

where W_{cr} is a material property similar in intent to the critical resolved shear stress. This transformation stress is a function of the tensile direction $\boldsymbol{e}$, and has been plotted via stereographic projection in Fig. 3 of [74]. This approach thus predicts the formation of the microstructure i that minimizes (4.5) for a given orientation.

4.3 Summary of experimental results

A brief summary of the relevant data and results from Shield [74] are presented here for convenience.

Shield performed Cu-Al-Ni tension test experiments at three different crystal orientations, and obtained the stress-strain response and images of the microstructures visible on the sample surface. The tests discussed here were performed under displacement control with fixed grips and at a temperature of 40°C. The 'dog-bone' test specimens were 38 mm long × 9.5 mm wide × 1 mm thick overall, with a 19 mm long × 6 mm wide gauge section. The samples were heat-treated such that they initially were composed entirely of the austenite phase. The material properties of Cu-Al-Ni are detailed in (1.8), (1.9) and §2.4.1, while the crystallographic orientations are supplied in Table 4.1. These three material orientations were chosen via (4.5) to be near the minimum, at an intermediate value, and at the maximum transformation stress, respectively.

The experimental stress-strain response, Fig. 4.1, and corresponding microstructures, Fig. 4.2, are given for each of the three sample orientations.

Orientation	Surface normal	Tension axis
A1-T1	$(-0.380, 0.925, 0.0)$	$(0.925, 0.380, 0.0)$
A1-T2	$(0.707, -0.707, 0.0)$	$(-0.447, -0.447, 0.775)$
A1-T3	$(0.707, -0.707, 0.0)$	$(-0.577, -0.577, 0.577)$

Table 4.1: Experiment specimen material orientations with respect to cubic axes. Orientation names are from Shield [74].

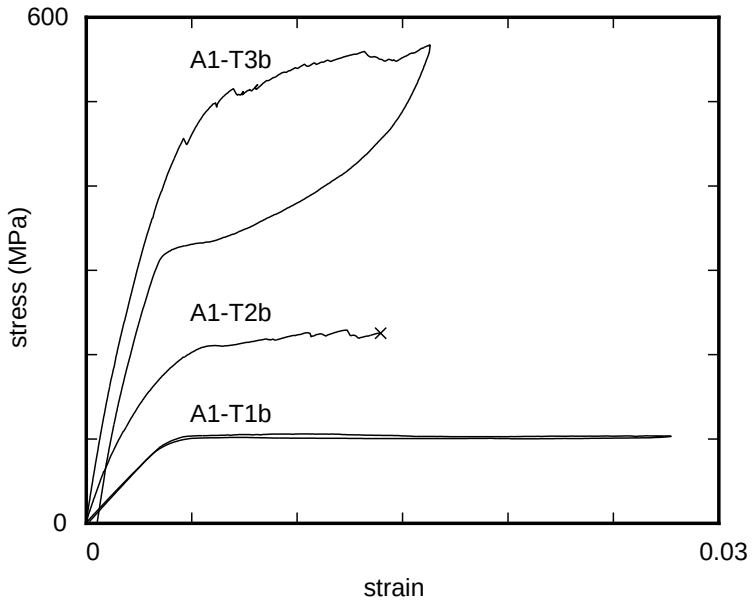

Figure 4.1: Experimentally obtained stress-strain response for Cu-Al-Ni at three material orientations [74] (reproduced with permission).

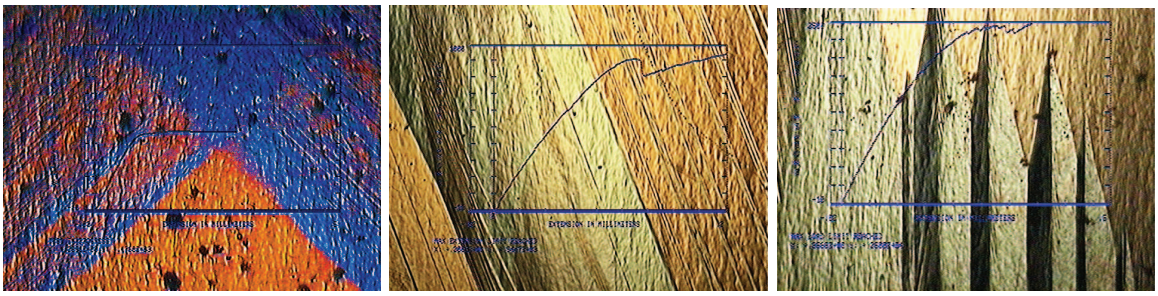

(a) (b) (c)

Figure 4.2: Microstructures visible on sample surface during tension tests for orientations: (a) A1-T1, (b) A1-T2 and (c) A1-T3. Notation and figures from Shield [74] (reproduced with permission).

The results for orientation A1-T1 indicate a short linear region followed by a nearly flat plateau, Fig. 4.1. The sample remained in the austenite phase until the knee in the curve, after which microstructures were observed, Fig. 4.2(a). In this figure orange and blue correspond to austenite and martensite, respectively. Of note, the two microstructures which appear as sets of crossed 45° lines were observed to respond independently during the experiment. Each individual blue region corresponds to a lamination of two martensite phases, with austenite–martensite interfaces perpendicular to the sample surface.

As expected, specimen A1-T2 was significantly stiffer than the first sample. However, it did not exhibit a linear regime. The observed decrease in stiffness was accompanied by the appearance of fine lamellae in the sample immediately upon the onset of loading. Near the plateau in the stress-strain curve the martensite areas were observed to grow rapidly, until the sample appeared as shown in Fig. 4.2(b). In this figure the austenite is the lighter of the two colors, with either side of the image consisting of several adjacent regions of twinned-martensite. The austenite–martensite interfaces appear as nearly vertical lines. The sample finally broke due to the out-of-plane deformation and the fixed-grip boundary conditions. Shield investigated this transverse response in a further set of experiments, but we will focus on the initial data.

The stiffest sample, A1-T3, also displayed initially nonlinear behavior accompanied by the formation of martensite. Up until the cusp at ∼500 MPa in Fig. 4.1 the microstructure appeared similar to that of specimen A1-T2, followed by the formation of twinned-martensite wedges, Fig. 4.2(c). Shield attributed the large amount of hysteresis observed in this test, as compared to the minimal hysteresis present in sample A1-T1, to the coupling between the martensite laminates on the left and right sides of each wedge.

See Table 4.2 for a summary of the experimental results [74]. Note that the variants were not identified experimentally, but inferred from the Schmid calculations.

Orientation	Modulus (GPa)	σ_{xform} (MPa)	ϵ_{xform}	Variants	A-M interface
A1-T1	26.7	108	0.45%	$(3,5)$ and $(4,5)$	46.8°
A1-T2	72.0	211	0.50%	$(2,4)$	21.4°
A1-T3 (initial)	158	511	0.65%	$(4,5)$ or $(2,4)$	9.8°
A1-T3 (wedge)				$(2,4)$	15.5°

Table 4.2: Summary of experimental results indicating initial modulus, transformation stress and strain, expected pair(s) of martensite variants, and the measured angle of the austenite–martensite interface. The variants are labeled as in Chapter 2, not [74], while the austenite–martensite interface angle is with respect to the tension axis in the plane of the sample.

4.4 Numerical results

In this section we present the application of the lamination algorithm to a model of the Shield experiment. To obtain physically realizable solutions we require the volumetric constraint (2.59) to enforce a positive jacobian of deformation. To limit branching, the nonlocal energy model presented in §2.5 is used, with the twin-boundary energy per unit area Γ set to 1 $\mathrm{J/m^2}$.

4.4.1 Initial single point calculations

For a first comparison, the laminate algorithm was applied to a single material point for each sample orientation. Although the macroscopic sample is under axial deformation, a representative infinitesimal deformation gradient is unclear. As a first approximation, only the axial component F_{33} was specified, with the other components of the deformation gradient obtained through a conjugate-gradient energy minimization. This is equivalent to a stress-free condition for the optimized components, and thus corresponds to a state of axial stress.

The computed stress-strain curves, Fig. 4.3, over-predict the transformation stress by almost exactly an order of magnitude. The sharp drop in the stress after transformation, with a corresponding discontinuity in the energy, is due to the pointwise nature of the

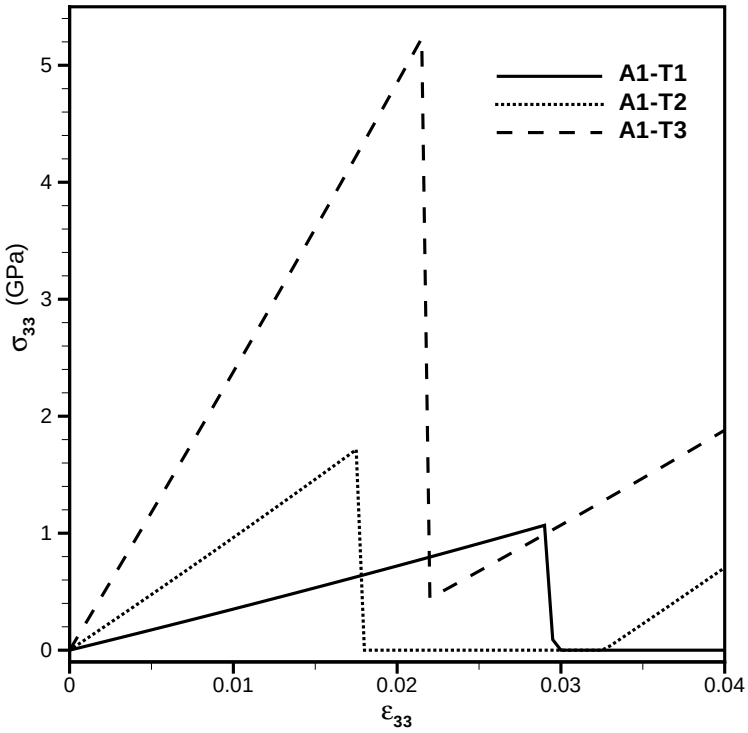

Figure 4.3: Initial single material point response for Cu-Al-Ni tension test.

calculation; the entire sample is transforming to the softer, lower energy, laminate. Note that the algorithm is able to completely relax the energy for orientation A1-T1 and A1-T2. Somewhat unexpectedly, the computed microstructures were simple laminates, versus the experimentally observed rank-two austenite–twinned martensite.

The modulus of 34.4 GPa obtained for A1-T1 is significantly higher than the experimental value of 26.7 GPa. The computed value does correspond to that obtained from linear elasticity for uniaxial stress using the given orientation and the stated moduli (2.40). The discrepancy is attributable to the $\sim 1^\circ$ orientation uncertainty and variation in material processing. The moduli at the other two orientations are influenced by these effects as well as the unexpected nonlinear softening discussed above.

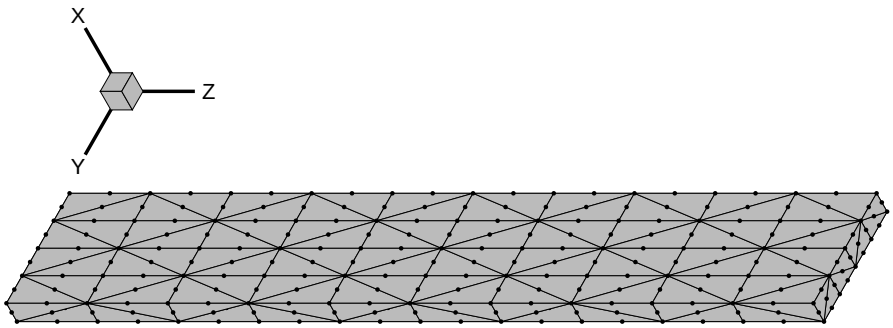

Figure 4.4: Finite element mesh of test specimen.

4.4.2 Finite element simulation

To better capture the experimental behavior, the lamination algorithm was used at the *subgrid* of a finite element model of the test specimen. This approach is of significant computational cost, requiring a parallel implementation and more robust solver consisting of an initial dynamic relaxation followed by a conjugate-gradient iteration. The mesh, Fig. 4.4, consists of 200 ten-node quadratic tetrahedral elements, and is 1 mm $\times$ 6 mm $\times$ 38 mm. Although the specimen and loading both possess several planes of symmetry, the experimental results do not; the mesh thus corresponds to the entire effective specimen. Unlike the single-point calculations, the boundary conditions here are unambiguous: the $\pm z$ faces are fixed except for prescribed z displacements on the $+z$ face, with the remainder of the boundary traction-free.

The stress-strain response, Fig. 4.5, is still at odds with the experimental results. The microstructures are again rank-one laminates as obtained above. As expected, the sharp drop accompanying transformation in the previous results does not occur here. While it is encouraging that the more realistic model and boundary conditions have reduced the transformation stresses, the continuing discrepancy is indicative of missing physical pro-

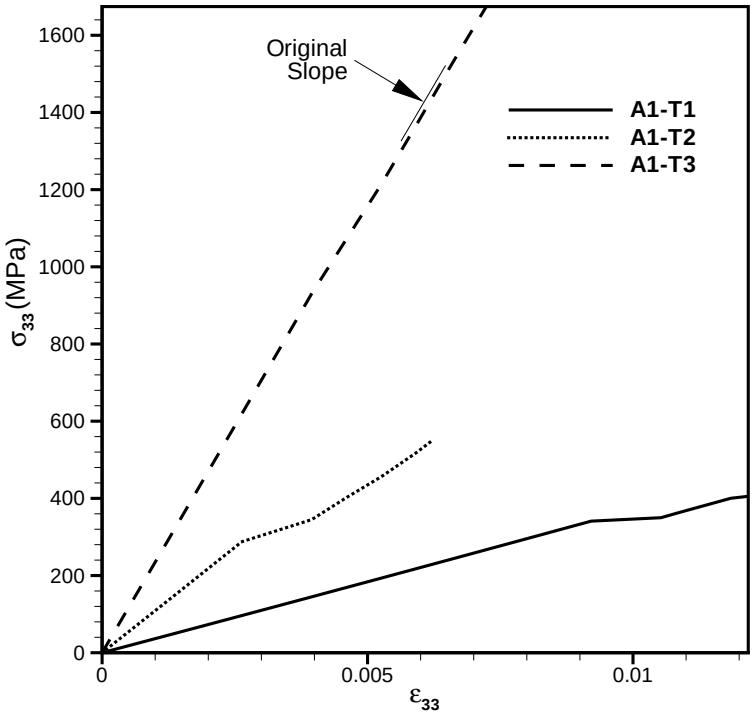

Figure 4.5: Stress-strain response of finite element simulation.

cesses in the model. Although it was expected that the sequential lamination algorithm, as implemented, would obtain the correct rank-two lamination, this clearly is not the case.

4.4.3 Austenite–twinned martensite extension

To attempt to reduce the high transformation stresses, the algorithm was modified to explicity allow for the direct formation of an austenite–twinned martensite microstructure. Thus, whenever a leaf is considered for branching (refer to §2.3.2) the algorithm tests both the two simple laminates as well as the eight austenite–twinned martensite microstructures for each pair of martensite wells, Fig. 4.6. The habit-plane solution, available, e.g., in either Shield [74] or Bhattacharya [17], and discussed in §1.1.2, provides the initial guess for $\{\lambda_2, \boldsymbol{a}_2, \boldsymbol{N}_2\}$ and $\{\boldsymbol{a}_1, \boldsymbol{N}_1\}$, while λ_1 is found by a line search.

This refinement was tested on a single Cu-Al-Ni laminate by loading from the austen-

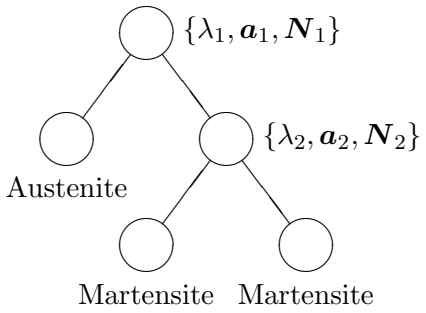

Figure 4.6: Tree representation of an austenite–twinned martensite microstructure.

ite transformation stretch to the transformation stretch of one of the martensitic variants through the linear interpolation

$$\boldsymbol{F}(t) = (1-t)\boldsymbol{I} + t\boldsymbol{U}_1 \tag{4.6}$$

where $\boldsymbol{I}$ and $\boldsymbol{U}_1$ are the stretches of the austenite and martensite phases, respectively. The lamination is again constrained by surface energy effects. It is evident, Fig. 4.7, that the transformation stress is greatly reduced.

4.4.4 Extended algorithm results

The tensile response was computed using the extended branching procedure. Due to time constraints it was not possible to recompute the finite element simulation. Instead, two sets of single point calculations were obtained for extremes in the conditions imposed on the deformation gradient $\boldsymbol{F}$. The first calculation fixed only the axial component F_{33}, with the remaining components obtained via minimization, as above, and will be referred to as the 'free BC' or axial stress case. In contrast, for the 'fixed BC' case only the F_{11} and F_{22} components were optimized, with F_{33} again providing the load, while the other components were fixed at zero.

The improved algorithm is successful in reducing the transformation stress, Fig. 4.8, for

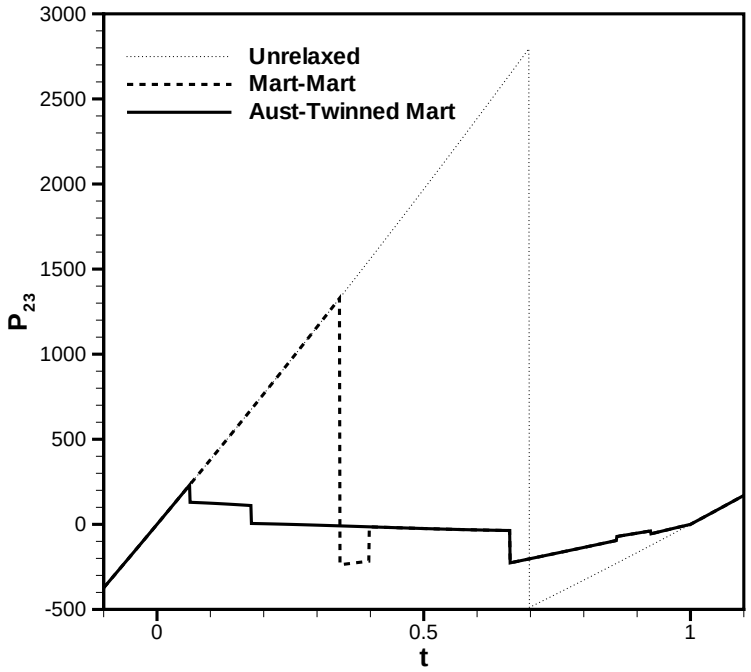

Figure 4.7: Comparison of stress response with and without explicit austenite–martensite branching. The loading is given by (4.6).

either boundary/loading condition. In the free boundary condition case, Fig. 4.8(a), while the transformation strain of A1-T1 is double the experimental value, it is quite reasonable for the other two orientations. However, the transformation stresses are still higher than experiment by about a factor of three. This discrepancy is certainly due in part to the nonlinear softening observed in the experiment for A1-T2 and A1-T3 caused by the development of microstructure from the onset, as well as uncertainty in the experimental crystal orientation. Finally, note that the lamination has resulted in a nearly stress-free state after transformation.

In the stiffer loading case, Fig. 4.8(b), the moduli have increased for the first two orientations, resulting in a reduction in the transformation strain. The response of sample A1-T3 is virtually unchanged up to transformation, but the more restrictive conditions do not allow the material to completely relax. This behavior is also evident for A1-T2.

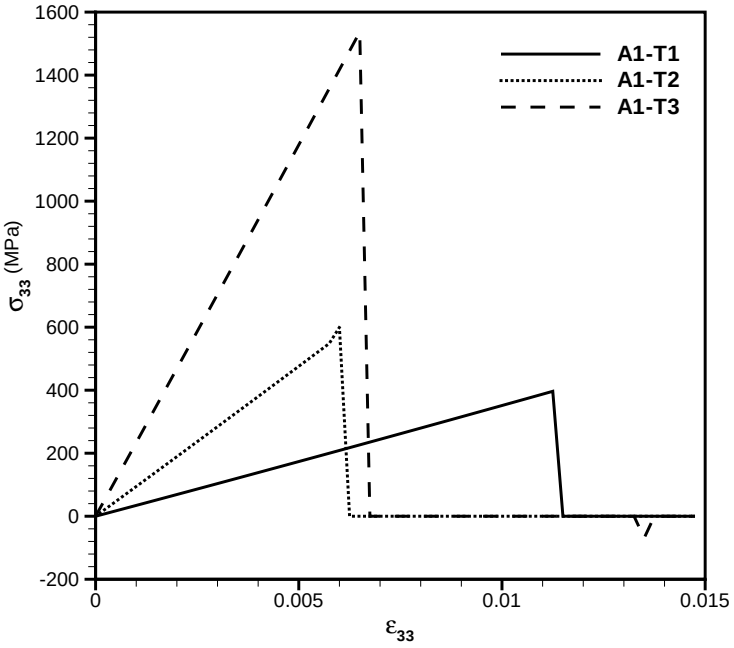

(a)

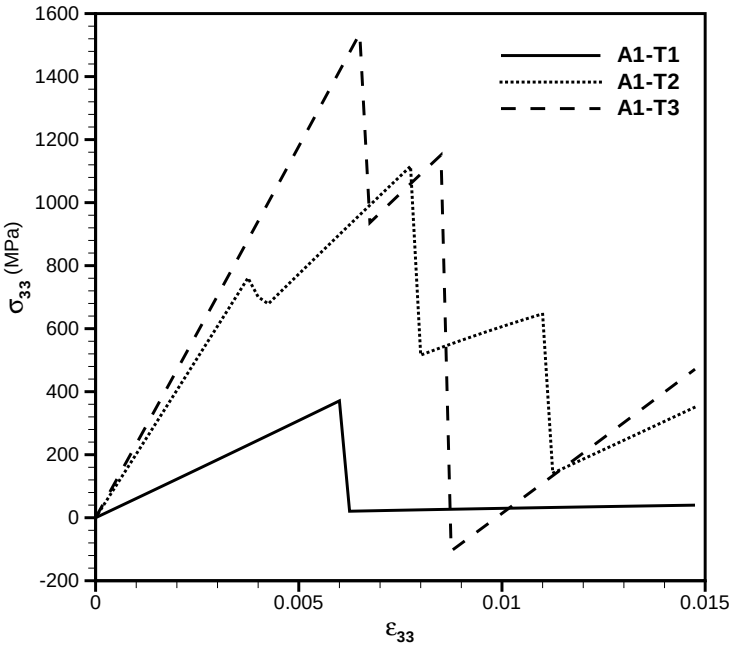

(b)

Figure 4.8: Computed stress-strain curves at a single material point using algorithm with explicit austenite–twinned martensite transformation with (a) free and (b) fixed boundary conditions.

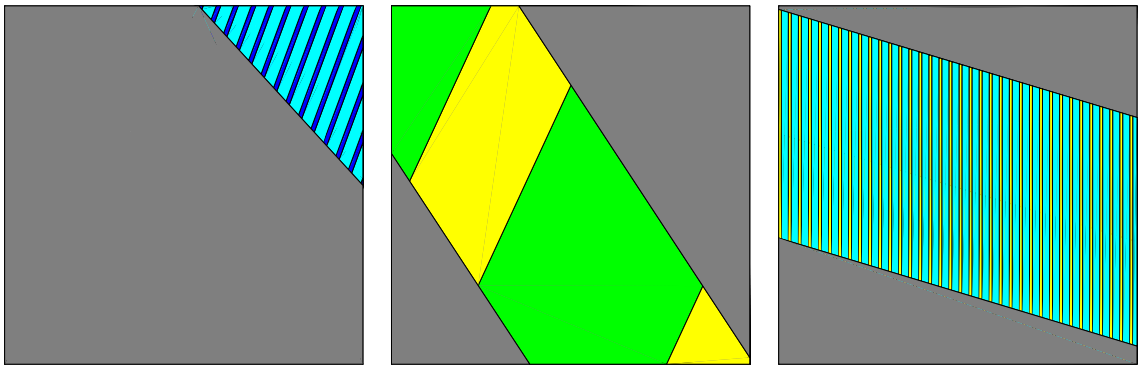

(a) (b) (c)

Figure 4.9: Representative microstructures computed at a single material point for orientations (a) A1-T1, (b) A1-T2 and (c) A1-T3. The grey represents austenite, while the remaining colors indicate martensite variants.

The computed microstructures, Fig. 4.9, did not vary appreciably between the two boundary condition cases. Noting that these results represent a single material point, the microstructures obtained for the first two orientations compare well with experiment, with the results for A1-T1 producing a nearly identical laminate. At the stiffest orientation, Shield obtained a martensite wedge microstructure which is explicitly excluded by sequential lamination and thus not obtained here.

A summary of the numerical results is presented in Table 4.3. The variants obtained for sample orientation A1-T1 correspond to those predicted by Shield, with the habit-plane angle also matching closely. The second orientation similarly obtains the correct variants, with approximately the correct habit-plane angle. As mentioned previously, the wedge microstructure obtained experimentally for A1-T3 is not allowed by the algorithm, although it did obtain the same variants.

Orientation	Modulus (GPa)	σ_{xform} (MPa)	ϵ_{xform}	Variants	A-M interface
A1-T1	$34.3 - 61.0$	$371 - 396$	$0.60\% - 1.13\%$	$(3, 5)$	$45°$
A1-T2	$94.4 - 202$	$600 - 761$	$0.38\% - 0.60\%$	$(2, 4)$	$34°$
A1-T3	234	1540	0.65%	$(4, 5)$	$75°$

Table 4.3: Numerically obtained modulus, transformation stress and strain, initial martensite variants and initial angle of the austenite–martensite interface. Where the results differ between the two boundary condition cases the value is indicated as a range.

4.5 Conclusions

The performance of the lamination algorithm described in the preceding has been compared with the experimental results of Shield. The branching scheme, as originally envisioned, is unable to obtain the austenite–twinned martensite observed experimentally, leading to the explicit addition of this microstructure, alongside martensite twins, as a possible branching type. With this modification the numerical results are quite promising, obtaining reasonable values for the transformation strain, and producing similar microstructures in the two cases describable by sequential laminates. Although the transformation stress and moduli are still higher than the experimental values, this is likely due in part to experimental uncertainty in the crystal orientation and material processing. The calculations also have not as yet attempted to include the nucleation of the initial lamina that contributed to the softer response obtained by Shield. The single material point calculations used in much of the above are not particularly suitable for these calculations, and the final comparison must await the reapplication of the finite element model with the improved lamination algorithm.

In closing, the comparison to date is very encouraging, especially given that there are essentially no free parameters in this model. The moduli and transformation stretches are known, with only the energy functional requiring specification. The only two other constants are related to the volumetric constraint and surface energy terms, currently used only to provide physical deformation gradients and length scales. These values, if reasonable, play little part in the material response.

Chapter 5

Conclusions and future directions

A practical numerical algorithm has been developed to compute the partial relaxation of a general multiwell energy density for arbitrary deformations. While the present work has focused on martensites, the model has been applied to polycarbonate and nematic elastomers as well as purely mathematical problems. The approach consists of the explicit construction of a sequential laminate such that new microstructures are obtainable via pruning and branching operations, while enforcing both static and configurational equilibrium. This *constrained* evolution, necessary to obtain reasonable computational complexity, coupled with equilibrium, provides a description for metastable material states and hence may display hysteresis. The algorithm was illustrated with calculations involving the mixing between two martensitic wells and a martensitic crystal loaded in simple shear.

For calculations with a separation between the microstructural and macroscopic structural scales, the lamination algorithm is suitable for inclusion at the *subgrid* level of a finite element calculation. This capability was demonstrated via a finite element simulation of spherical indentation in Cu-Al-Ni which developed complex microstructures and resulted in a softer response than obtained via direct energy minimization.

The lamination procedure was verified through the computation of several benchmark problems. An exact result was obtained in the first computation involving three pairwise

rank-one connected wells. The classic four-well problem, in which the wells are compatible, but do not differ by a rank-one matrix, was more difficult. The calculations obtained the exact zero energy result along much of the rank-one connections involved in the analytic solution, and relaxed the energy by more than 98% near the origin. This shortcoming was determined to primarily be due to the 'algorithmic' energy barrier imposed by the method of microstructural evolution. In the final examples, the algorithm was able to obtain the exact quasiconvexification of the nematic elastomer model by DeSimone and Dolzmann [35] and of the polycarbonate model of Fortunelli et al. [41]. Both of these latter models incorporate an energy well, formulated in the principal frame, that consists of a continuum of $SO(3)$ invariant states rather than the separate wells encountered, e.g., in martensitic materials.

The verification tests also indicated the importance of reasonable values for the initial guesses used to initiate the laminate optimization. Toward this end, the analytic solution was used in several of the above problems. While this may present a difficulty in some applications, it is not a consideration for many problems of interest, including martensitic materials, in which reasonable values are available.

The final work in this development was to use the lamination algorithm to predict the experimental results of Shield [74]. As originally written the model did not correctly obtain the rank-two microstructure observed experimentally. Explicit inclusion of the austenite–twinned martensite microstructure as a possible lamination type produced good initial numerical results for the two cases in which the experiment produced a sequential laminate. Note that the present algorithm does not contain any tunable parameters. Further finite element simulations of the complete test specimen are planned and should improve the comparison.

Experimental observations include both sequential laminates and more complex mi-

crostructures, such as the martensite wedges from the third of Shield's tests, indicating a need to extend or generalize the current approach. Such future research must be carefully undertaken to preserve the mathematical basis of the present work.

As discussed, an energy barrier precludes the attainment of the full relaxation in some instances. The resulting discontinuous energy can be very challenging to minimize numerically, especially when integrated into a global finite element calculation. While improvement in this area would greatly improve the model, the proper course of action is unclear. One possible approach, similar to Monte Carlo methods from statistical mechanics, would be to accept a branch that leads to an energy increase with some probability less than one, while an energy reducing branch would always be taken. Although a more deterministic approach is desirable, it is unclear how to more fully explore the topology of the lamination graph without incurring combinatorial complexity. On the other hand, although this energy barrier is troublesome in mathematical problems, it is suggestive of the activation energies and metastabilities present in physical processes, and is in this sense not undesirable.

Finally, materials such as Cu-Al-Ni often exhibit significant hysteresis, not attainable with the present approach. This behavior can be included by replacing the configurational equilibrium with a kinetic model for interfacial motion [2, 3, 75], possibly including interface orientation.

Bibliography

[1] R. Abeyaratne, K. Bhattacharya, and J. K. Knowles. Strain-energy functions with multiple local minima: modeling phase transformations using finite thermoelasticity. In Y. Fung and R. W. Ogden, editors, *Nonlinear elasticity: theory and application*, pages 1–50. Cambridge University Press, 2001.

[2] R. Abeyaratne, C. Chu, and R. D. James. Kinetics of materials with wiggly energies: theory and application to the evolution of twinning microstructures in a Cu-Al-Ni shape memory alloy. *Philosophical Magazine A*, 73(2):457–497, 1996.

[3] R. Abeyaratne and J. K. Knowles. On the kinetics of an austenite → martensite phase transformation induced by impact in a Cu-Al-Ni shape-memory alloy. *Acta Materialia*, 45(4):1671–1683, 1997.

[4] E. Aranda and P. Pedregal. Numerical approximation of non-homogeneous, non-convex vector variational problems. *Numerische Mathematik*, 89(3):425–444, 2001.

[5] E. Aranda and P. Pedregal. On the computation of the rank-one convex hull of a function. *SIAM Journal on Scientific Computing*, 22(5):1772–1790, 2001.

[6] S. Aubry, K. Bhattachatya, and M. Ortiz. Effective behavior of single crystals. to be submitted.

[7] S. Aubry, M. Fago, and M. Ortiz. A constrained sequential-lamination algorithm for the simulation of sub-grid microstructure in martensitic materials. *Computer Methods in Applied Mechanics and Engineering*, 192(26–27):2823–2843, 2003.

[8] R. J. Aumann and S. Hart. Bi-convexity and bi-martingales. *Israel Journal of Mathematics*, 54(2):159–180, 1986.

[9] J. M. Ball. Convexity conditions and existence theorems in nonlinear elasticity. *Archive for Rational Mechanics and Analysis*, 63(4):337–403, 1977.

[10] J. M. Ball, C. Chu, and R. D. James. Hysteresis during stress-induced variant rearrangement. *Journal de Physique IV*, 5:245–251, 1995. Colloque C8, supplément au journal de physique III.

[11] J. M. Ball and R. D. James. Fine phase mixtures as minimizers of energy. *Archive for Rational Mechanics and Analysis*, 100(1):13–52, 1987.

[12] J. M. Ball and R. D. James. Proposed experimental tests of a theory of fine microstructure and the two-well problem. *Philosophical Transactions of the Royal Society of London A*, 338:389–450, 1992.

[13] S. Bartels, C. Carstensen, and P. Plecháč. Finite element computation of macroscopic quantities in nonconvex minimization problems and applications in materials science. In A. M. Sandig, W. Schiehlen, and W. L. Wendlan, editors, *Multifield Problems: State of the Art*, pages 69–79. Springer-Verlag Berlin, 2000.

[14] K. Bhattacharya. Wedge-like microstructure in martensites. *Acta Metallurgica et Materialia*, 39(10):2431–2444, 1991.

[15] K. Bhattacharya. Self-accommodation in martensite. *Archive for Rational Mechanics and Analysis*, 120:201–244, 1992.

[16] K. Bhattacharya. Comparison of the geometrically nonlinear and linear theories of martensitic transformations. *Continuum Mechanics and Thermodynamics*, 5:205–242, 1993.

[17] K. Bhattacharya. *Microstructure of Martensite—Why it forms and how it gives rise to the shape-memory effect*. Oxford Series on Materials Modelling. Oxford University Press, 2003.

[18] K. Bhattacharya and G. Dolzmann. Relaxed constitutive relations for phase transforming materials. *Journal of the Mechanics and Physics of Solids*, 48:1493–1517, 2000.

[19] K. Bhattacharya and G. Dolzmann. Relaxation of some multi-well energies. *Proceedings of the Royal Society of Edinburgh A*, 131:279–320, 2001.

[20] K. Bhattacharya, N. B. Firoozye, R. D. James, and R. V. Kohn. Restrictions on microstructure. *Proceedings of the Royal Society of Edinburgh A*, 124:843–878, 1994.

[21] K. Bhattacharya, B. Li, and M. Luskin. The simply laminated microstructure in martensitic crystals that undergo a cubic-to-orthorhombic phase transformation. *Archive for Rational Mechanics and Analysis*, 149:123–154, 1999.

[22] M. L. Bisilliat. *Comportement mechanique d'un polycarbonate a grande vitesse de sollicitation. Etude Experimentale et simulation.* PhD thesis, L'Ecole Nationale Superieure des Mines de Paris, 1997.

[23] P. Bladon, E. M. Terentjev, and M. Warner. Transitions and instabilities in liquid-crystal elastomers. *Physical Review E*, 47(6):3838–3840, 1993.

[24] P. Boullay, D. Schryvers, and R. V. Kohn. Bending martensite needles in $Ni_{65}Al_{35}$ investigated by two-dimensional elasticity and high-resolution transmission electron microscopy. *Physical Review B*, 64(14):144105, 2001.

[25] C. Carstensen and P. Plecháč. Numerical solution of the scalar double-well problem allowing microstructure. *Mathematics of Computation*, 66(219):997–1026, 1997.

[26] M. Chipot, C. Collins, and D. Kinderlehrer. Numerical analysis of oscillations in multiple well problems. *Numerische Mathematik*, 70:259–282, 1995.

[27] M. Chipot and D. Kinderlehrer. Equilibrium configurations of crystals. *Archive for Rational Mechanics and Analysis*, 103(3):237–277, 1988.

[28] C. Chu. *Hysteresis and microstructures: A study of biaxial loading on compound twins of copper-aluminum-nickel single crystals*. PhD thesis, University of Minnesota, 1993.

[29] C. Chu and R. D. James. Analysis of microstructures in Cu-14.0% Al-3.9% Ni by energy minimization. *Journal de physique IV*, 5:143–149, 1995. Colloque C8, supplément au journal de physique III.

[30] C. Collins. Computation of twinning. In D. Kinderlehrer, R. James, M. Luskin, and J. L. Ericksen, editors, *Microstructure and Phase Transition*, volume 54 of *The IMA Volumes in Mathematics and its Applications*, pages 39–50. Springer-Verlag, 1993.

[31] C. Collins, M. Luskin, and J. Riordan. Computational results for a two-dimensional model of crystalline microstructure. In D. Kinderlehrer, R. James, M. Luskin, and J. L. Ericksen, editors, *Microstructure and Phase Transition*, volume 54 of *The IMA Volumes in Mathematics and its Applications*, pages 51–57. Springer-Verlag, 1993.

[32] S. Conti, A. DeSimone, and G. Dolzmann. Soft elastic response of stretched sheets of nematic elastomers: a numerical study. *Journal of the Mechanics and Physics of Solids*, 50:1431–1451, 2002.

[33] R. Dacorogna. *Direct methods in the calculus of variations*. Springer-Verlag Berlin, 1989.

[34] A. DeSimone. Energy minimizers for large ferromagnetic bodies. *Archive for Rational Mechanics and Analysis*, 125:99–143, 1993.

[35] A. DeSimone and G. Dolzmann. Macroscopic response of nematic elastomers via relaxation of a class of SO(3)-invariant energies. *Archive for Rational Mechanics and Analysis*, 161:181–204, 2002.

[36] G. Dolzmann. Numerical computation of rank-one convex envelopes. *SIAM Journal on Numerical Analysis*, 36(5):1621–1635, 1999.

[37] G. Dolzmann. *Variational Methods for Crystalline Microstructure – Analysis and Computation*. Springer-Verlag, 2003.

[38] G. Dolzmann, B. Kirchheim, S. Müller, and V. Šverák. The two-well problem in three dimensions. *Calculus of Variations and Partial Differential Equations*, 10:21–40, 2000.

[39] G. Dolzmann and N. J. Walkington. Estimates for numerical approximations of rank one convex envelopes. *Numerische Mathematik*, 85:647–663, 2000.

[40] J. L. Ericksen. Some phase transitions in crystals. *Archive for Rational Mechanics and Analysis*, 73:99–124, 1980.

[41] A. Fortunelli, M. Fago, and M. Ortiz. Phase transitions in BPA-polycarbonate. in preparation.

[42] A. Fortunelli, C. Geloni, and A. Lazzeri. Theoretical simulation of the plastic behavior of amorphous glassy Bis-Phenol-A polycarbonate. *Macromolecules*, 2004. submitted.

[43] X. Gao and L. C. Brinson. A simplified multivariant SMA model based on invariant plane nature of martensitic transformation. *Journal of Intelligent Material Systems and Structures*, 13:795–810, 2002.

[44] I. M. Gelfand and S. V. Fomin. *Calculus of Variations*. Dover, 2000.

[45] S. Govindjee and C. Miehe. A multi-variant martensitic phase transformation model: formulation and numerical implementation. *Computer Methods in Applied Mechanics and Engineering*, 191(3-5):215–238, 2001.

[46] S. Govindjee, C. Miehe, and G. J. Hall. The free energy of mixing for n-variant martensitic phase transformations using quasi-convex analysis. *Journal of the Mechanics and Physics of Solids*, 51(4):I–XXVI, 2003.

[47] G. J. Hall and S. Govindjee. Application of a partially relaxed shape memory free energy function to estimate the phase diagram and predict global microstructure evolution. *Journal of the Mechanics and Physics of Solids*, 50:501–530, 2002.

[48] J.-B. Hiriart-Urruty and C. Lemaréchal. *Fundamentals of Convex Analysis*. Springer, 2001.

[49] R. D. James and D. Kinderlehrer. Theory of diffusionless phase transitions. In M. Rascle, D. Serre, and M. Slemrod, editors, *PDEs and continuum models of phase transitions*, number 344 in Lecture Notes in Physics, pages 207–215. Springer, 1989.

[50] R. D. James, R. W. Kohn, and T. W. Shield. Modeling of branched needle microstructures at the edge of a martensite laminate. *Journal de Physique IV*, 5(C8):253–259, 1995. Colloque C8, supplément au journal de physique III.

[51] D. Kinderlehrer and P. Pedregal. Characterizations of young measures generated by gradients. *Archive for Rational Mechanics and Analysis*, 115:329–365, 1991.

[52] R.V. Kohn. Relaxation of a double-well energy. *Continuum Mechanics and Thermodynamics*, 3:193–236, 1991.

[53] R.V. Kohn and G. Strang. Explicit relaxation of a variational problem in optimal design. *Bulletin of the American Mathematical Society*, 9(2):211–214, 1983.

[54] R.V. Kohn and G. Strang. Optimal design and relaxation of variational problems I-II-III. *Communications in Pure and Applied Mathematics*, 39:113–137, 139–182, 353–377, 1986.

[55] M. Kruzik. Numerical approach to double well problems. *SIAM Journal on Numerical Analysis*, 35(5):1833–1849, 1998.

[56] B. Li and M. Luskin. Finite element analysis of microstructure for the cubic to tetragonal transformation. *SIAM Journal on Numerical Analysis*, 35:376–392, 1998.

[57] B. Li and M. Luskin. Approximation of a martensitic laminate with varying volume fractions. *Mathematical Modelling and Numerical Analysis*, 33(1):67–87, 1999.

[58] M. Luskin. On the computation of crystalline microstructure. *Acta Numerica*, 5:191–257, 1996.

[59] C. B. Morrey, Jr. *Multiple Integrals in the Calculus of Variations*. Springer-Verlag, 1966.

[60] S. Müller. Variational models for microstructure and phase transitions. In *Calculus of Variations and Geometric Evolution Problems*, volume 1713 of *Lecture Notes in Mathematics*, pages 85–210. Springer-Verlag, Berlin, 1999.

[61] S. Müller and V. Šverák. Attainment results for the two-well problem by convex integration. In J. Jost, editor, *Geometric Analysis and the Calculus of Variations*, pages 239–251. International Press, 1996.

[62] P. Neff. Suitable energy functionals to limit jacobian. Personal communication, 2001.

[63] M. Ortiz and E. A. Repetto. Nonconvex energy minimization and dislocation structures in ductile single crystals. *Journal of the Mechanics and Physics of Solids*, 47(2):397–462, 1999.

[64] M. Ortiz, E. A. Repetto, and L. Stainier. A theory of subgrain dislocation structures. preprint submitted to Elsevier preprint.

[65] M. Ortiz and L. Stainier. The variational formulation of viscoplastic constitutive updates. *Computer Methods in Applied Mechanics and Engineering*, 171:419–444, 1999.

[66] P. Pacheco. *Parallel Programming with MPI.* Morgan Kaufmann, 1996.

[67] A. Pandolfi. Inpenetrability constraints. Unpublished, 2001.

[68] M. C. Payne, M. P. Teter, D. C. Allan, T. A. Arias, and J.D. Joannopoulos. Iterative minimization techniques for *ab initio* total-energy calculations: molecular dynamics and conjugate gradients. *Rev. Mod. Phys.*, 64(4):1045–1097, 1992.

[69] P. Pedregal. Laminates and microstructure. *European Journal of Applied Mathematics*, 4:121–149, 1993.

[70] P. Pedregal. Optimization, relaxation and young measures. *Bulletin of the American Mathematical Society*, 36(1):27–58, 1999.

[71] P. Pedregal. *Variational Methods in Nonlinear Elasticity.* SIAM, 2000.

[72] P. Rosakis and H. Tsai. Dynamic twinning processes in crystals. *International Journal of Solids and Structures*, 32(17/18):2711–2723, 1995.

[73] J. R. Shewchuk. An introduction to the conjugate gradient method without the agonizing pain. http://www.cs.cmu.edu/~quake-papers/painless-conjugate-gradient.ps, 1994.

[74] T. W. Shield. Orientation dependence of the pseudoelastic behavior of single crystals of Cu-Al-Ni in tension. *Journal of the Mechanics and Physics of Solids*, 43(6):869–895, 1995.

[75] N. K. Simha and K. Bhattacharya. Kinetics of phase boundaries with edges and junctions in a three-dimensional multi-phase body. *Journal of the Mechanics and Physics of Solids*, 48:2619–2641, 2000.

[76] V. P. Smyshlyaev and J. R. Willis. On the relaxation of a three-well energy. *Proceedings of the Royal Society of London A*, 455:779–814, 1999.

[77] P. Spellucci. A new technique for inconsistent qp problems in the sqp method. *Mathematical Methods of Operations Research*, 47(3):355–400, 1998.

[78] S. Stupkiewicz and H. Petryk. Modelling of laminated microstructures in stress-induced martensitic transformations. *Journal of the Mechanics and Physics of Solids*, 50:2303–2331, 2002.

[79] M. Suezawa and K. Sumino. Behavior of elastic-constants in Cu-Al-Ni alloy in close vicinity of m_s-point. *Scripta Metallurgica*, 10(9):789–792, 1976.

[80] V. Šverák. Rank-one convexity does not imply quasiconvexity. *Proceedings of the Royal Society of Edinburgh A*, 120:185–189, 1992.

[81] E. B. Tadmor, G. S. Smith, N. Bernstein, and E. Kaxiras. Mixed finite element and atomistic formulation for complex crystals. *Physical Review B*, 59(1):235–245, 1999.

[82] E. B. Tadmor, U. V. Waghmare, G. S. Smith, and E. Kaxiras. Polarization switching in $PbTiO_3$: an ab initio finite element simulation. *Acta Materialia*, 11(50):2989–3002, 2002.

[83] L. Tartar. Some remarks on separately convex functions. In D. Kinderlehrer, R. James, M. Luskin, and J. L. Ericksen, editors, *Microstructure and Phase Transition*, volume 54 of *The IMA Volumes in Mathematics and its Applications*, pages 191–204. Springer-Verlag, 1993.

[84] M. Warner and E. M. Terentjev. Nematic elastomers—a new state of matter? *Progress in Polymer Science*, 21:853–891, 1996.

[85] M. Yasunaga, Y. Funatsu, S. Kojima, K. Otsuka, and T. Suzuki. Measurement of elastic-constants. *Scripta Metallurgica*, 17(9):1091–1094, 1983.

[86] L. C. Young. *Lectures on the Calculus of Variations and Optimal Control Theory*. Chelsea, 1980.

[87] X. Y. Zhang, L. C. Brinson, and Q. P. Sun. The variant selection criteria in single-crystal CuAlNi shape memory alloys. *Smart Materials and Structures*, 9(5):571–581, 2000.

[88] E. R. Zubarev, S. A. Kuptsov, T. I. Yuranova, R. V. Talroze, and H. Finkelmann. Monodomain liquid crystalline networks: reorientation mechanism from uniform to stripe domains. *Liquid Crystals*, 26(10):1531–1540, 1999.